TITANIUM-BASED ANODE MATERIALS FOR LITHIUM ION BATTERIES: CRYSTALLITE SIZE, POROUS STRUCTURE AND DOPING EFFECTS

Dissertation

zur Erlangung des akademischen Grades

„Doctor rerum naturalium“

– Dr. rer. nat. –

eingereicht am

Fachbereich 08 - Biologie und Chemie

der Justus-Liebig-Universität Gießen

von

M. Sc. Junpei Yue

2016

1. Reviewer / Gutachter: Prof. Dr. Bernd Michael Smarsly

2. Reviewer / Gutachter: Prof. Dr. Jürgen Janek

Submitted / Eingereicht: May 2016

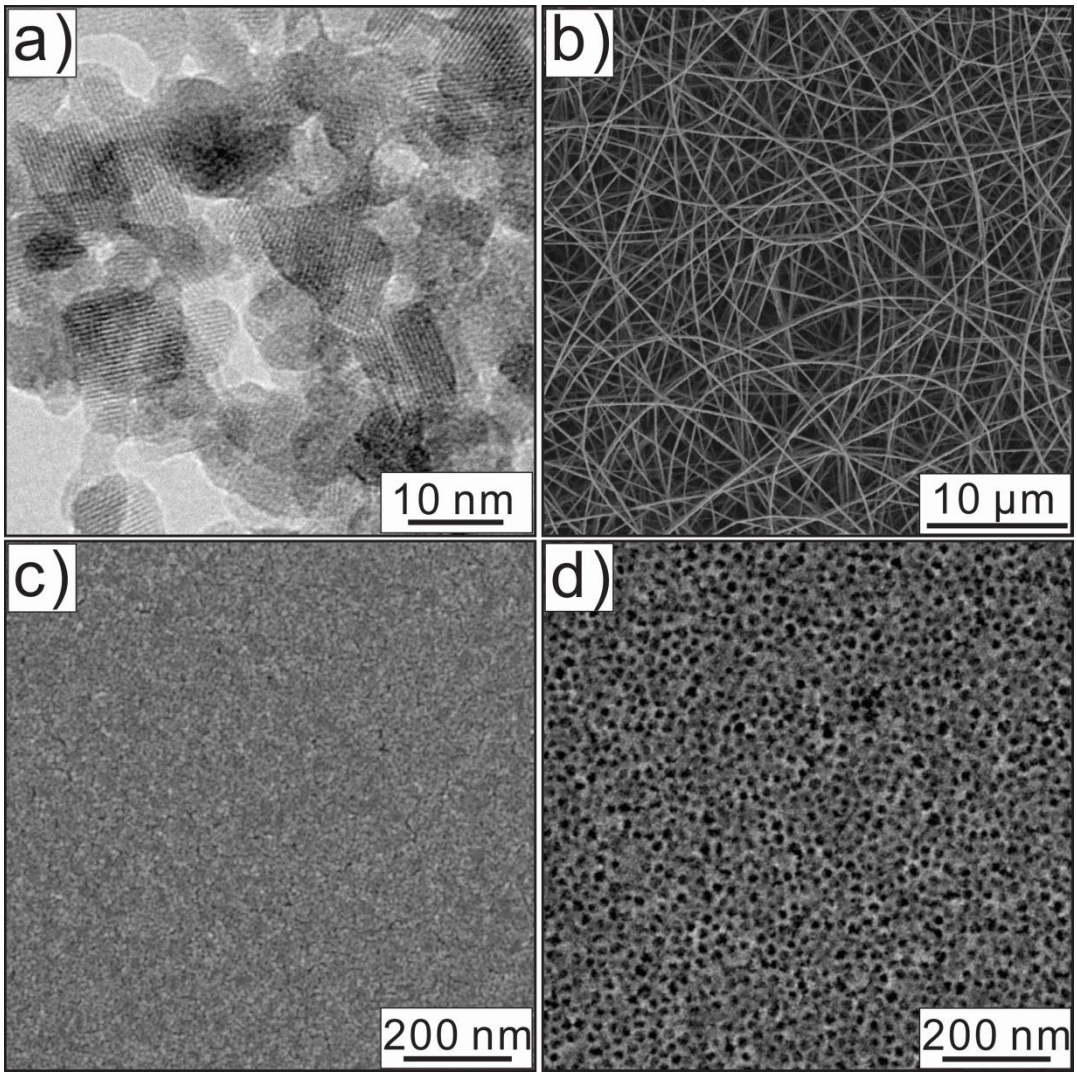

(a) LTO nanocrystals; (b) LTO nanofibers; (c) Nb:TiO_2 film; (d) Mesoporous Nb:TiO_2 film

三十功名尘与土, 八千里路云和月, 莫等闲, 白了少年头, 空悲切!------岳飞

Declaration

This work was completed under the supervision and guidance of Prof. Bernd Smarsly, at Justus-Liebig-Universität Gießen, Germany.

I declare:

I prepared the present dissertation by myself and without unauthorized help from others. Every citation involved literally or adapted from the literature or oral communication has been marked appropriately. I have applied the principles of best scientific practice documented in the charter of the Justus Liebig University of Giessen in all investigations described in this thesis.

Erklärung

Diese Arbeit wurde unter der Aufsicht ung Leitung von Prof. Bernd Smarsly an der Justus-Liebig-Universität Gießen (Deutschland) durchgeführt.

Ich erkläre:

Ich habe die vorliegende Dissertation selbstständig und ohne unerlaubte Hilfe anderer angefertigt. Alle Textstellen, welche wörtlich oder sinngemäß aus Veröffentlichungen entnommen sind, oder auf mündlichen Auskünften beruhen, sind als solche kenntlich gemacht. Die Grundsätze guter wissenschaftlicher Arbeit, wie sie in der Satzung der Justus-Liebig-Universität festgehalten sind, wurden von mir bei allen in dieser Thesis beschriebenen Untersuchungen eingehalten.

Junpei Yue

May 2016

ABSTRACT

Anatase TiO_2 and spinel $Li_4Ti_5O_{12}$ (LTO) have attracted ever-increasing attention as anode materials for LIBs due to their high and flat intercalation potentials and stable structures. The application of both materials in the high-power LIBs, however, is restricted by their low electronic conductivity and the sluggish Li^+-ion diffusion in them. In this thesis, nanostructuring and doping were used to cope with these issues. Additionally, the major attention is paid to investigate the impacts of crystallite size, porous structure and doping on their electrochemical charge storage.

Niobium doped TiO_2 ($Nb:TiO_2$) nanocrystals with a crystallite size of 6 nm were prepared by a novel non-aqueous method based on *tert*-amyl alcohol and 1-hexanol under the assistance of microwave radiation. The doping level can be tuned from 2 to 10 at% by the niobium precursor concentration. The crystallite size can be tailored from 4 to 20 nm by the reaction parameters. The electrochemical properties of $Nb:TiO_2$ as the anode material were evaluated, and the results indicate $Nb:TiO_2$ with the doping level of 5 at% shows the best performance owing to its highest conductivity.

It has been proven that nanocrystals with a crystallite size of several nanometers will exhibit a significant pseudocapacitive contribution in previous studies. Up until now there are no direct studies on the conductivity effect on the pseudocapacitive contribution. Here mesoporous $Nb:TiO_2$ films were selected as model materials to investigate it. In order to obtain mesoporous $Nb:TiO_2$ films with the similar crystallinity and specific surface area, these films were prepared based on the self-assembly of preformed nanocrystals by dip-coating. The results reveal that the 5 at% $Nb:TiO_2$ presents the highest conductivity of 9.8×10^{-5} S/cm and the pseudocapacitive contribution varies in the same trend with the conductivity of these films.

LTO nanocrystals were prepared by a benzyl alcohol-based non-aqueous process and the crystallite sizes can be tuned from 3 to 7 nm by changing the reaction temperature. The other reaction parameters including reaction concentration and precursors have little effect on crystallite sizes. The crystalline structure, surface components and the formation mechanism of these nanocrystals were investigated in detail. The unreacted alkoxide, carbonate and the benzoate are found on the surface. The liquid reaction products such as toluene, benzaldehyde and dibenzyl ether imply a reaction path of the analogous Meerwein-Ponndorf-Verley reaction and a side reaction of the ether elimination.

In order to improve the conductivity of LTO, Nb^{5+} and Al^{3+} ions were used to substitute Ti^{4+} ions in TiO_6 octahedrons. However Al^{3+} ions prefer to substitute the Li^+ in LiO_4 tetrahedrons. The Al:LTO nanocrystals present the highest conductivity due to the high doping level. LTO nanocrystals possess the higher specific capacity at the small C-rates (200 mAh/g at 1C to 153 mAh/g at 10C) than Al:LTO and Nb:LTO nanocrystals. The investigation of the crystallite size effect on electrochemical performance was conducted on LTO and Al:LTO nanocrystals with different crystallite sizes. The results indicate that nanocrystals can enhance the rate capacity and specific capacity on account of the short diffusion distance of electrons and Li^+ ions. On the other hand, the LTO nanocrystals with a crystallite size of 3 nm possess a large amount of pseudocapacitive contribution and this effect results in a large irreversible energy loss at the small C-rates owing to the surface restructuring.

Mesoporous LTO films and powders can be successfully prepared based on the sol-gel process, but a well-controlled heat treatment is required to avoid the formation of anatase TiO_2. The study of the porosity impact on the electrochemical performance was carried out on untemplated, mesoporous and macroporous LTO films. These films were prepared based on their preformed nanocrystals under the assistance of soft or hard templates. Macroporous LTO films exhibit the best rate capacity (150 mAh/g at 160C) compared with dense and mesoporous films. Mesoporous LTO nanofibers can be successfully prepared *via* electrospinning and it can deliver a specific capacity as high as 145 mAh/g at 10C.

ZUSAMMENFASSUNG

Auf Grund ihrer hohen und flach verlaufenden Interkalationspotentiale sowie ihrer stabilen Struktur erfuhren Titandioxid in Anatas-Modifikation und der Spinell $Li_4Ti_5O_{12}$ (LTO) ein stetig wachsendes Interesse als Anodenmaterialien für LIBs. Die Anwendung beider Materialien in leistungsstarken LIBs wird jedoch durch die geringe elektronische Leitfähigkeit und langsame Li^+ Ionendiffusion begrenzt. Um diese Probleme zu überwinden, wurde in dieser Arbeit Prinzipien der Nanostrukturierung und des Dotierens angewendet. Zusätzlich wurden die Einflüsse der Kristallitgröße, poröser Strukturen und des Dotierens auf die elektrochemische Ladungsspeicherung untersucht.

Niob-dotierte TiO_2 (Nb:TiO_2) Nanokristallite mit Kristallitgrößen im Bereich von 6 nm wurden anhand einer neuen, nicht-wässrigen, auf tert-Amylalkohol und 1-Hexanol basierenden Mikrowellensynthese hergestellt. Der Dotiergrad kann durch die Niobkonzentration in den Vorläuferverbindungen im Bereich von 2 bis 10% eingestellt werden. Die Größe der Kristallite kann auf Basis der Syntheseparameter im Bereich von 4 bis 20 nm variiert werden. Die elektrochemischen Eigenschaften des Nb:TiO_2 als Anodenmaterial wurden untersucht. Die Resultate zeigen, dass ein Dotiergrad von 5 % im Falle des Nb:TiO_2 auf Grund der höchsten Leitfähigkeit die beste Leistung zeigt.

In früheren Studien konnte gezeigt werden, dass Nanokristallite mit einer Größe von mehreren Nanometern einen signifikanten pseudokapazitiven Beitrag leisten. Bis zuletzt gibt es jedoch keine Studien, welche den Einfluss der Leitfähigkeit auf den pseudokapazitiven Beitrag zeigen. In dieser Arbeit wurde dies anhand mesoposöser Nb:TiO_2-Filme untersucht. Um mesoporöse Filme mit vergleichbarer Kristallinität und spezifischer Oberfläche zu erhalten, wurden diese Filme auf Basis der Selbstanordnung von Nanokristallen mittels Tauchbeschichtung hergestellt. Aus den Ergebnissen geht hervor, dass Nb:TiO_2 mit einem Dotiergrad von 5 % mit 9.8×10^{-5} S/cm die höchste Leitfähigkeit zeigt und dass die pseudokapazitiven Beiträge der gleichen Entwicklung folgen wie die Leitfähigkeiten der Filme.

LTO Nanokristallite wurden auf der Grundlage einer nicht-wässrigen, Benzylalkohol-basierten Synthese hergestellt und die Kristallitgröße konnte durch Einstellen der Reaktionstemperatur im Bereich von 3 bis 7 nm variiert werden. Andere parameter wie Reaktionskonzentration und Vorläuferverbindung zeigen nur einen geringen Einfluss auf die Kristallitgröße. Die kristallinen Strukturen, die Oberflächen Komponenten sowie der Bildungsmechanismus der Nanokristallite wurde im Detail untersucht. Auf der Oberfläche

konnten unreagierte Alkoxide, Carbonate und Benzoate nachgewiesen werden. Flüssige Reaktionsprodukte wie Toluol, Benzaldehyd und Dibenzylether legen nahe, dass Reakion analog zur Meerwein-Ponndorf-Verley-Reaktion zu verlaufen scheint und die Ethereliminierung als Nebenreaktion abläuft.

Um die Leitfähigkeit des LTO zu verbessern, wurden Ti^{4+} Ionen in den TiO_6 Oktaedern durch Nb^{5+} Ionen und Al^{3+} Ionen substituiert. Al^{3+} neigt dazu, Li^{+} in LiO_4 Tetraedern zu ersetzen. Auf Grund des hohen Dotiergrades zeigten Al:LTO Nanokristallite die höchste Leitfähigkeit. LTO Nanokristallite zeigen eine höherer spezifische Kapazität bei geringen C-Raten (200 mAh/g bei 1C bis 153 mAh/g bei 10C) als Al:LTO und Nb:LTO Nanokristallite. Die Untersuchen der Einflusses der Kristallitgröße auf die elektrochemischen Leistungen wurden anhand von LTO und Al:LTO Nanokristalliten mit unterschiedlichen Kristallitgrößen durchgeführt. Die Ergebnisse legen nahe, dass Nanokrsitallite die Ratenkapazität und die spezifische Kapazität auf Grund kurzer Elektronen- und Li+ Ionendiffusionswege verbessern. Andererseits zeigen LTO Kristallite mit einer Kristallitgröße von 3 nm einen großen Anteil an pseudokapazitiven Beitrag, welches auf Grund von Oberflächenrekonstruktionen zu einem großen irreversiblen Energieverlust bei kleinen C-Raten führt.

Mesoporöse LTO Filme und Pulver können auf Basis des Sol-Gel Prozesses erfolgreich präpariert werden. Um die Bildung von Anatas zu vermeiden ist jedoch eine kontrollierte Temperaturbehandlung nötig. Die Untersuchungen des Porösitätseinflusses auf die elektrochemische Leistung wurden für untemplatierte, mesoporöse und makroporöse LTO File durchgeführt, welche durch Weich- und Harttemplatierungsprozesse mit vorgefertigten Partikeln generiert wurden. Macroporöse LTO Filme zeigen im Vergleich zu mesoporösen und dichten Filmen die beste Ratenkapazität (150 mAh/g bei 160C). Mesoporöse LTO Fasern können über das Elektrospinnen präpariert werden und zeigen eine spezifische Kapazität von 145 mAh/g bei 10C.

CONTENTS

LIST OF ABBREVIATIONS

AC	Alternating current
Al:LTO	Aluminum-doped spinel lithium titanate ($Li_4Ti_5O_{12}$)
BET	Brunauer-Emmett-Teller
BELLA	The battery and electrochemistry laboratory
BJH	Barrett-Joyner-Halenda
CV	Cyclic voltammetry
DEC	Diethyl carbonate
DLS	Dynamic light scattering
DMC	Dimethyl carbonate
DTA	Differential thermal analysis
EC	Ethylene carbonate
EIS	Electrochemical impedance spectroscopy
EISA	Evaporation-induced self-assembly
FTIR	Fourier transform infrared spectroscopy
FTO	Fluorine-doped tin oxide
FWHM	Full width at half maximum
GC-MS	Gas chromatography mass spectrometry
ICP-MS	Inductively coupled plasma mass spectrometry
ITO	Indium-doped tin oxide
IUPAC	International union of pure and applied chemistry
KIT	Karlsruhe Institute of Technology
LTO	Spinel lithium titanate ($Li_4Ti_5O_{12}$)
LIBs	Lithium-ion batteries
MS	Mass spectroscopy
Nb:LTO	Niobium-doped spinel lithium titanate ($Li_4Ti_5O_{12}$)
Nb:TiO_2	Niobium-doped anatase TiO_2
NLDFT	Nonlocal density function theory
NMP	N-methyl-2-pyrrolidon
PC	Propylene carbonate
PEO 1000K	Poly(ethylene oxide), average Mv 1000000
PIB_{50}-*b*-PEO_{45}	Poly(isobutylene)-*block*-poly(ethylene oxide)
PS	Polystyrene
PVA	Poly(vinyl alcohol)
PVDF	Polyvinylidene fluoride
rGO	Reduced graphene oxide
SEI	Solid electrolyte interface
SAED	Selected area electron diffraction
SAXS	Small angle X-ray scattering
SDA	Structure directing agent
SEM	Scanning electron microscopy
TEM	Transmission electron microscopy
TGA	Thermal gravimetric analysis
UV-Vis	Ultraviolet-visible
XPS	X-ray photoelectron spectroscopy
XRD	X-ray diffraction

CHAPTER 1
BACKGROUND AND MOTIVATION

1.1 Lithium-ion batteries

In 1991 Lithium-ion batteries (referred as to LIBs) became commercialized by Sony Corporation, which have flourished the markets in portable electronic devices, such as cameras, phones and computers. Nowadays LIBs are getting more and more important in the new markets of the grid energy storage, hybrid electric vehicles (HEVs), and the requirements on the rate capacity and safety issues of LIBs have become higher and higher.[1] The commercial LIBs are assembled with graphite as an anode material and $LiCoO_2$ as a cathode material separated by a porous insulated membrane, as illustrated in Figure 1.1. During charging process, Li^+ ions are extracted from the layered lithium metal oxides and migrate through the porous separator and are inserted into graphite. In discharging process, Li^+ ions move from graphite back to the layered lithium metal oxides. In comparison with other electrochemical energy storage and conversion systems, LIBs have gravimetric energy densities in the range of 120 to 150 Wh/Kg, three times higher than those of Nickel-Cadmium or lead acid systems.[2]

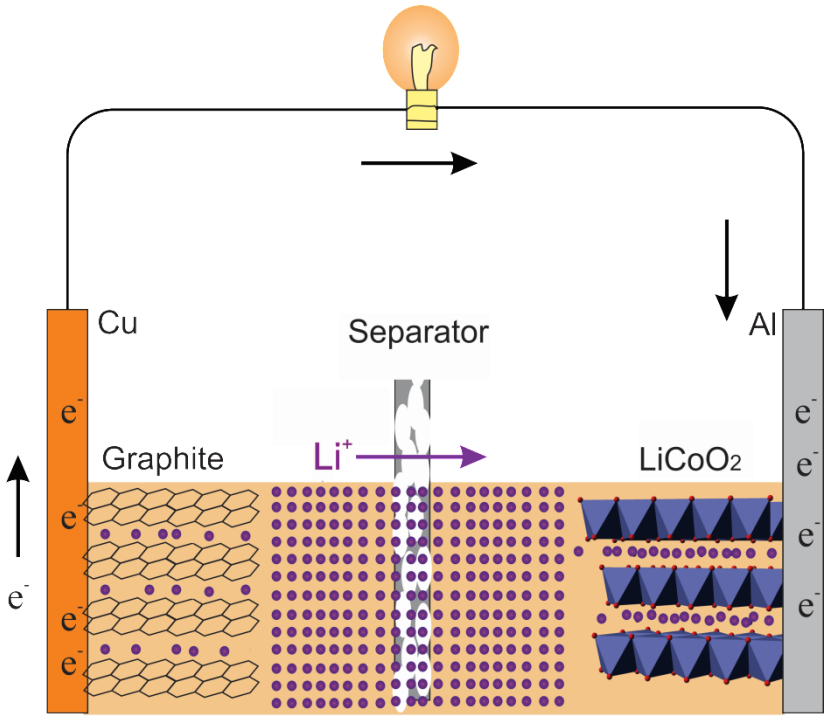

Figure 1.1 Illustration of a lithium-ion battery. When discharging a battery, Li^+ ions migrate from graphite (negative electrode) to $LiCoO_2$ (positive electrode).

The commercial anode material of LIBs is graphite. Graphite can accommodate Li^+ ions to form LiC_6 and provides a specific capacity of 372 mAh/g. The intercalation reaction of Li^+

ions into graphite occurs at the potential of around 0.5~0.6 V vs Li^+/Li. Lithium deposition, however, may take place to form lithium dendrites on graphite at such low potential. Lithium dendrites can penetrate the separator resulting in a short circuit. The electrolytes with special additives can be decomposed to form a solid electrolyte interface (SEI) film and this SEI film on the surface of graphite can prevent the formation of lithium dendrites. On the other hand, the stability of the SEI film and undesired structural changes in graphite (e.g., exploitation or non-active sites) during the charging and discharging process are detrimental to safety and lifetime of LIBs.[3-5] Therefore seeking an alternative anode material has attracted more and more attention.

A large number of candidates for anode materials have been extensively studied over the past two decades. In brief, these candidates can be divided into several categories: alloy reaction materials such as Si, Sn, Sb and Ge; conversion reaction materials such as iron oxide, nickel oxide, and cobalt oxide; and intercalation reaction materials such as lithium titanate spinel ($Li_4Ti_5O_{12}$, LTO) and anatase (TiO_2). Alloy anode materials have an ultra-high specific capacity, which can be up to 10 times higher than that of graphite. On the other hand, the volume of alloy anode materials expands 2 to 3 times after the full lithiation, for instance, 3.2-fold expansion for Si and 2.6-fold expansion for Sn. The considerable volume change during lithiation/delithiation reaction will bring about a pulverization and isolation of active materials in the electrode, leading to a poor cycle stability.[6-9] Transition metal oxides such Fe_2O_3, CuO and CoO can undergo reversible reduction in the presence of Li^+ ions, delivering 2 or 3 times higher specific capacity than that of graphite.[4, 10-15] Metal sulfides, phosphides and fluorides have been proven to be able to undergo such reaction as well.[16-18] The low Coulombic efficiency and cycle stability derived from the irreversible phase transformation at the reduction process impede their application. Further the other promising candidates for anode materials are intercalation reaction materials. More and more attention have been paid to the Ti-based materials such as LTO and TiO_2 (e.g., anatase, rutile, brookite, TiO_2-b and even amorphous), attributed to their structural stability during the intercalation reaction.[19-23]

LTO was first reported as an anode material for LIBs in 1994, and since then numerous studies have been carried out in order to learn its electrochemical and structural properties.[24] Li^+ ions can be reversibly inserted into and extracted from LTO at a potential of 1.55 V vs Li^+/Li. The high intercalation potential of LTO prevents lithium deposition and electrolyte decomposition, which is crucial for electrode durability and safety. The spinel structure of $Li_4Ti_5O_{12}$ ($Fd\bar{3}m$) comprises eight formula units of $(Li)^{8a}[Li_{1/3}Ti_{5/3}]^{16d}O_4^{32e}$ per unit cell, in

which Li^+ entirely occupies 8 tetrahedral (*a*) sites, while the 16 octahedral (*d*) sites are occupied by one-third Li^+ and five-third Ti^{4+} (seeing Figure 1.2). The remaining oxygen ions on 32*e* sites form a cubic close-packed structure. Intriguingly, during the lithiation, the $Li_4Ti_5O_{12}$ structure undergoes a change to $[(Li)_{1-x}{}^{8a}[Li]_{2x}{}^{16c}[Li_{1/3}Ti_{5/3}]^{16d}O_4{}^{32e}]$, which is accompanied by a minor volume expansion of ~0.2% due to the migration of Li^+ ions from tetrahedral (*a*) sites toward octahedral (*c*) sites.[25, 26] The advantage of LTO derived from structural stability as "zero strain" material enables safe operation, high rate capacity and excellent cyclability.[27]

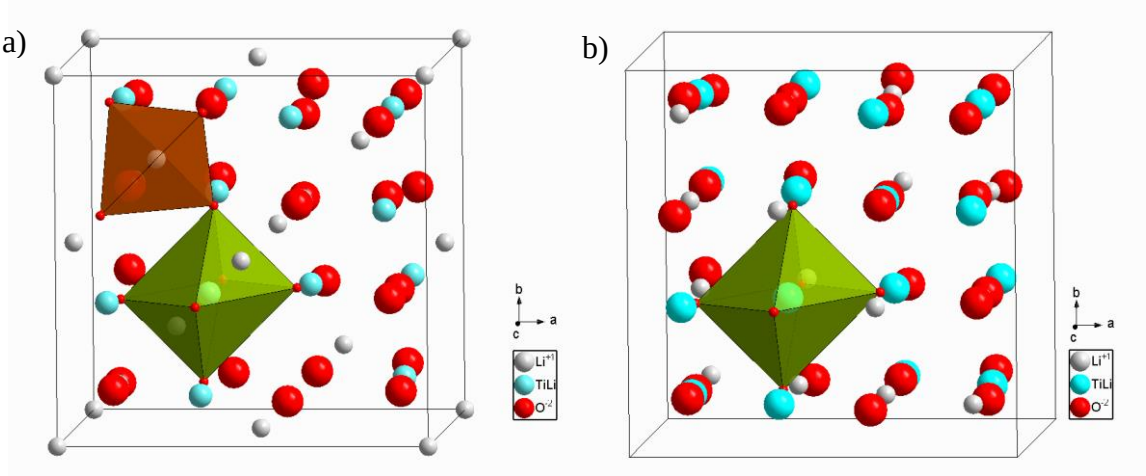

Figure 1.2 Unit cell of $Li_4Ti_5O_{12}$ ($[Li]^{8a}[Li_{1/3}Ti_{5/3}]^{16d}O_4$) (a) and $Li_7Ti_5O_{12}$ ($[Li_2]^{16c}[Li_{1/3}Ti_{5/3}]^{16d}O_4$) (b). The stable frame of $[Li_{1/3}Ti_{5/3}]^{16d}O_4$ is shown as an octahedron and $[Li]^{8a}$ is centered in a tetrahedron.

Anatase TiO_2 is another promising anode material for LIBs and the electrochemical intercalation reaction can be written as:

$$TiO_2 + xLi^+ + xe^- \underset{2.0V}{\overset{1.75V}{\rightleftharpoons}} Li_xTiO_2,$$

where *x* is the mole fraction of Li in TiO_2. The maximum Li^+ capacity in anatase varies from 0.5 to 1 depending on the crystallite size and morphology etc. The value of 0.5 is mostly used to describe the intercalation reaction according to the literature.[28-31] When Li^+ ions enter anatase structure, a structural phase transition and subsequent separation into lithium-poor and lithium-rich phases takes place because of the interaction of intercalated Li^+ ions. The structure of lithium-rich phase ($Li_{0.51}TiO_2$) was studied by neutron diffraction and is believed to present orthorhombic structure with space group of *Imma*, number 74.[32] In comparison with anatase TiO_2 (*I*41/*amd*, number 141), the unit cell decreases in c-axis direction and increases along b-axis. The Li^+ ions in lithiated anatase were believed to occupy 4*e* sites. The unit cell structures of anatase and lithiated anatase phase ($Li_{0.51}TiO_2$) are shown in Figure 1.3.

The volume expansion for LTO and anatase TiO_2 after the intercalation reaction is much smaller than in the case of alloy reaction materials, and the crystalline phase change during the intercalation reaction is much smaller than in conversion reaction materials. The structural stability during the intercalation reaction can ensure long battery lifetime. In addition, the high intercalation potentials of LTO and anatase TiO_2 can prevent the formation of lithium dendrites and SEI films, which can guarantee battery safety. These two advantages of LTO and TiO_2 make them become the most promising anode materials for the LIBs applied in grid energy storage and hybrid electric vehicles.

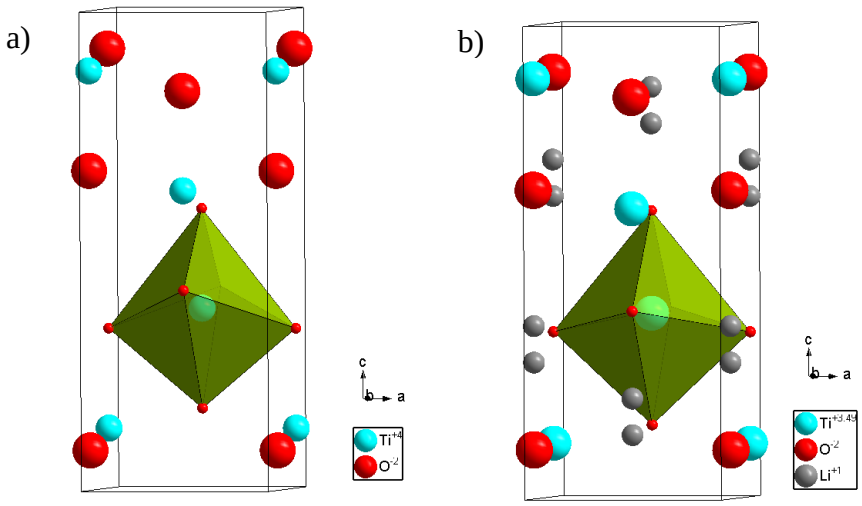

Figure 1.3 Unit cell of anatase TiO_2 (a) and lithiated anatase $Li_{0.51}TiO_2$ (b). The octahedral TiO_6 is shown in green.

The drawbacks of these two materials are their poor electronic conductivity and the sluggish Li^+ ion diffusion. Shortening the diffusion distances by nanostructuring the materials and increasing intrinsic conductivity by changing the electronic structure of materials are two of the most effective approaches to handle the issues.

1.2 Nanostructured materials

Nanostructuring is regarded as one of the most effective methods to improve the kinetic process by providing an available electrolyte transport path and significantly shortening the distance of ion diffusion and electron transport. The characteristic time constant t for the diffusion in a particle with diffusion length of L is given by $t=L^2/D$, where D is the diffusion constant. The diffusion time decreases with the square of the decreasing particle length.[33] Except from facilitating the dynamic diffusion, the high surface area and surface energy can change the thermodynamics of a reaction.[34] There are a few studies on the electrochemical charge storage in nanosized anatase and LTO, which presented a significant difference

compared with bulk materials on account of the interfacial charge storage.[26, 35-37] The interfacial charge storage could be an under-potential deposition reaction or an intercalation reaction occurring on the surface.[38] The interfacial charge storage is significantly dependent on the crystallite size. Taking anatase TiO_2 for example, the interfacial charge storage will take up to 50% in the total charge storage when the crystallize size is less than 10 nm. In many studies the interfacial charge storage in intercalation reaction materials is regarded as pseudocapacitive contribution, because the intercalation reaction occurring on the surface follows the capacitive law. Later the studies on pseudocapacitive contribution were extended to the other intercalation materials (such as Nb_2O_5, MoO_3, and metal chalcogenides).[39-42] Further, Brezesinski et al. compared the pseudocapacitive contribution of anatase electrodes with different morphologies including anatase films from the nanocrystal assembly with and without soft-templates and from a sol-gel process. The results demonstrate that both high specific surface area and mesoporosity play important roles in improving the pseudocapacitive contribution.[43] A mesoporous structure surrounded with numerous nanocrystals has been proven to be the most suitable morphology for the study of pseudocapacitive contribution.[44] Additionally, Augustyn et al. investigated the crystallinity effect on pseudocapacitive contribution of Nb_2O_5 and the results reveal that the pseudocapacitive charge storage involving Li^+ intercalation prefers to occur in crystalline phase.[45] Unfortunately, researches were concentrated on the pseudocapacitive behavior of different intercalation materials and the effects of crystallite size, morphology and crystallinity on the pseudocapacitive contribution, with only few studies on the influence of the conductivity on the pseudocapacitive charge storage of the intercalation materials.

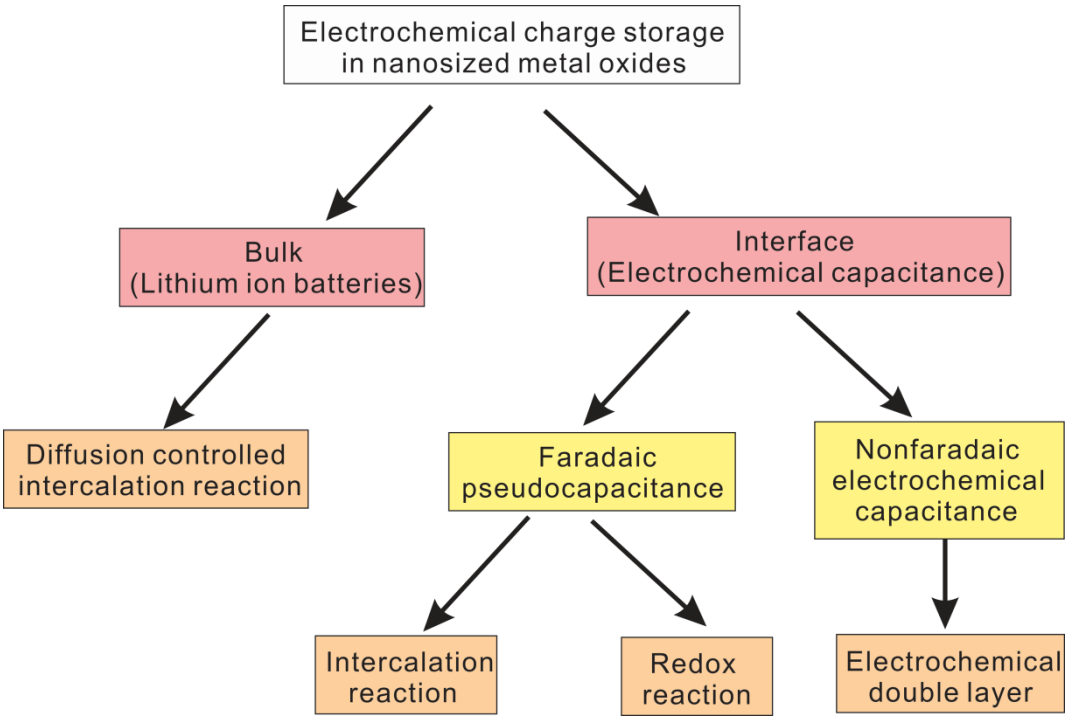

Figure 1.4 Different mechanisms of electrochemical charge storage in nanosized metal oxides.

An important indication of pseudocapacitive contribution in the galvanostatic charge/discharge profiles is the fact that the plateau representing the multiphase equilibrium regimes will be partially replaced by gradient slopes.[46] In this way it is not sufficient to evaluate the interfacial charge storage. Since the pseudocapacitive concept was proposed by Conway et al., there have been a few studies about how to quantify the interfacial charge storage. The well-known approach is based on the scan rate-dependent cyclic voltammetry.[30, 47] The stored charges in nanosized TiO_2 or LTO can be divided into three parts: the faradaic contribution from the Li^+ ion intercalation process, the faradaic contribution from the charge-transfer process with surface atoms referred to as pseudocapacitance, and the nonfaradaic contribution from the double layer capacitance (showing in Figure 1.4). Among the three contributions, the bulk intercalation reaction is diffusion-limited and the other two are surface area-limited. The current from the intercalation reaction is proportional to the square root of the scanning rate, while the current from capacitive contributions is proportional to the scanning rate. The total current can be written as

$$j_V = k_C v + k_F v^{1/2} \quad (1)$$

and equation (1) is divided by $v^{1/2}$, giving

$$j_V / v^{1/2} = k_C v^{1/2} + k_F \quad (2)$$

where j_V is the current density at potential of V and v is the scanning rate. Therefore plotting $j_V / v^{1/2}$ against $v^{1/2}$ following equation 2, the contribution from each of the three parts can be quantified (showing equation 2).[47] In a real system, the difference of the electrochemical polarization at different scanning rates at the same potential makes the results from the above proposal without any physical meanings at a wide potential range.[48] Therefore finding a new approach to evaluate the pseudocapacitance is still a challenge.

As mentioned above, nanocrystals with different dimensions play a crucial role in investigating the interfacial charge storage. The preparation of nanocrystals less than 10 nm is another great challenge, especially for LTO. The common methods for the preparation of nanomaterials are solid state reaction, sol-gel chemistry, hydrothermal methods etc.[49-57] The solid state reaction is much slower than solvent-based reactions. Thus it needs a longer reaction time and a higher reaction temperature to form pure crystalline materials. For that reason it is generally not possible to prepare nanocrystals less than 10 nm based on solid state reaction.[52, 53, 50, 58] The sol-gel method requires a high temperature to transform the gel products into the crystalline materials and the intricate crystallization process results in the final products with unpredicted crystallinity and phase composition.[51, 54] The hydrothermal method is a robust protocol to prepare nanomaterials with different shapes and crystallite sizes. To the best of our knowledge, however, there are no reports about the preparation of LTO nanocrystals with the crystallite size of several nanometers using hydrothermal methods. Apart from these conventional techniques, some new ones such as a supercritical alcohol route and a flame spray pyrolysis were applied to prepare LTO nanocrystals with crystallite sizes less than 20 nm.[59, 60] All of these new techniques need special reaction conditions compared with the traditional chemical routes.

The surfactant-controlled non-aqueous process can be used to produce nanocrystals with the excellent control of crystallite sizes, shapes and monodispersibility, but the large amount of organic residue and toxicity of surfactants obstruct its development and application. The solvent-controlled non-aqueous approach based on benzyl alcohol was introduced by Niederberger in 2002 to prepare crystalline TiO_2 at low temperature, and since then this approach has been extensively adopted to prepare metal oxides and binary metal oxides.[61-63] There were several studies about the preparation of Nb:TiO_2 and LTO nanocrystals with the crystallite size less than 10 nm based on the solvent-controlled non-aqueous approach.[64-66] A disadvantage of the benzyl alcohol route is that the as-made nanocrystals have been proven to possess the poor dispersibility in alcohols. Preformed nanocrystals and alcohols are the best

building blocks and solvents for constructing nanostructures respectively. Hence it is requisite to explore other solvents to prepare crystalline metal oxides. *Tert*-alcohols are regarded as the eligible candidates owing to the similar stability of their intermediates ($((CH_3-(CH_2)_x)_3-C^+$) with benzyl alcohol (benzyl cation, $Ph-CH_2^+$). Bein et al. have successfully used *tert*-butanol to prepare metal oxides such as TiO_2, Nb:TiO_2, NiO, Fe_2O_3 and LTO.[66-69] The problem of the *tert*-butanol route is the low crystallinity of oxides. In this thesis, *tert*-amyl alcohol has been first and successfully used to prepare TiO_2 and Nb:TiO_2. Additionally, the primary alcohol (1-hexanol) was introduced to increase the crystallinity. In this approach, TiO_2 and Nb:TiO_2 nanocrystals can be successfully prepared within 5 minutes under the assistance of microwave radiation, and the obtained nanocrystals possess quite high dispersibility in water (20 wt%) and ethanol (10 wt%).

The preparation of LTO nanocrystals is much more complicated than the preparation of TiO_2. Pinna et al. had tried to use benzyl alcohol to prepare LTO nanocrystals but the as-made LTO nanocrystals contained a certain amount of anatase. In this thesis, in order to obtain phase-pure LTO, the reaction conditions including reaction temperature, concentration, Li and Ti precursors will be studied in detail. Furthermore the Al^{3+} and Nb^{5+}-doped LTO nanocrystals were also successfully prepared.

Mass transportation from bulk electrolytes to the surface of nanocrystals is another issue. Continuous porous structures with nanocrystalline walls have been recognized as an effective approach to facilitate the mass transportation by providing transportation path. According to the classification of IUPAC, there are three kinds of pores: micropore with a pore size of less than 5 nm, mesopore with a pore size from 5 to 50 nm and macropore with a pore size of more than 50 nm. The different pore categories possess different functions. For instance, microporosity is essential for supercapacitors owing to the high surface area, however detrimental for mass transportation. Macroporosity holds the converse properties. The well-established procedure for preparing porous material relies on the self-assembled soft or hard templates, which has been elaborated in many reviews.[70-75] Apart from the templates, the precursors are equally crucial for successfully producing expected crystalline materials with porous structures. Normally the precursors are salts which can form gel clusters or oligomers surrounding micelles or hard templates. The gel products or oligomers can be crystallized into expected products at certain temperatures. Ordered mesoporous LTO and Nb:TiO_2 films have been prepared based on such process.[69, 76-78] In some special cases, it is not possible to prepare porous structure based on sol-gel process on account of the intricate crystallization process.

For preparing large-scaled mesoporous LTO, it has been proven that a well-controlled crystallization process is required to avoid the impurity phase of anatase.[76] Additionally, dispersible preformed nanocrystals are suitable building blocks for constructing porous films as well. The porous materials prepared from sol-gel process possess low boundary resistance, which is beneficial for the charge transfer process, while the one prepared from preformed nanocrystals has more accessible path and higher surface area, which is beneficial for the mass transformation. The comparison of porosity and electrochemical performance between films from sol-gel process and preformed nanocrystals will be drawn in this thesis.

1.3 Increasing electrical conductivity by doping

Doping is a robust protocol to significantly raise the conductivity of metal oxides, and the representative examples are indium-doped tin oxide (ITO), fluorine-doped tin oxide (FTO), Al-doped ZnO, and Nb-doped TiO_2.[79-82] Both electronic structure (band structure) and crystalline structure (vacancy or interstitial defects) of materials can be modified by doping. For that reason, doping has been widely applied in electrode materials. Myriad studies about doped TiO_2 and their properties have been carried out. For example, Yutaka et al. reported that 6 at% Nb doped TiO_2 film presents the characteristic of a degenerated semiconductor and the conductivity of such film is comparable with the commercial ITO film.[82] Liu et al. prepared Nb-doped TiO_2 with crystallite sizes of several nanometers and found that the doping resulted in the reduction of Nb^{5+} and Ti^{4+}. In his case, the 20 at% Nb-doped TiO_2 presented the highest conductivity around 3×10^{-4} Scm^{-1}.[66] De Trizio reported colloidal Nb-doped TiO_2 nanocrystals, and such nanocrystals show a broad absorption ranging from visible light to the mid-infrared light because the substitution of Ti^{4+} with Nb^{5+} generates free carriers inside the conduction band.[83] There are two approaches to compensate the extra positive charge stemmed from the substitution of Ti^{4+} with Nb^{5+}: one is the reduction of Nb^{5+} and Ti^{4+}, and another one is the production of Ti^{4+} vacancies. In this work, *tert*-amyl alcohol was used to prepare Nb-doped TiO_2, and the compensation approaches and the impacts of conductivity on pseudocapacitive contribution were investigated as well.

In case of LTO, the studies about Mg^{2+}, Na^{+} or Cs^{+} substituted LTO indicated that the conductivity can be enhanced from 10^{-13} to 10^{-2} Scm^{-1}.[84-86] The dopant can be divided into three categories according to the substituted elements (Li, or Ti or O). From the above description of LTO crystalline structure, the octahedron TiO_6 is a stable framework and Li^{+} ions migrate among the interstitial positions of octahedrons (8*a*→16*c*→8*a* or 8*a*→16*c*→48*f*→16*d*).[87, 88] When Li^{+} ions in tetrahedrons (8*a* site) were substituted by other

cations, the Li^+ diffusion path can be partially blocked by dopant cations, and such substitution would result in a smaller specific capacity than undoped LTO. In order to maintain the diffusion path available, the substitutions of Ti or O in TiO_6 octahedrons are the common cases. Therefore Nb^{5+}, V^{5+}, Zr^{4+}, Cr^{3+}, Al^{3+}, Ti^{3+}, Fe^{2+}, Mn^{2+} etc. were used to substitute Ti^{4+} and F^-, Br^-, N^{3-} etc. were used to replace O^{2-}.[51, 58, 89-94] In this thesis, the attention will be focused on the aliovalent ions Nb^{5+} and Al^{3+}-doped LTO nanocrystals and their doping mechanisms (the cation substitution occurs in tetrahedrons or octahedrons). The influence of different doping mechanisms on electrochemical properties was studied as well.

In order to facilitate the electron transport from active materials to current collector, a certain amount of conducting agents such as active carbon, carbon black, carbon nanotubes and graphene were introduced into the preparation of an electrode. The challenge is the homogeneous mixing of conducting agents and active materials cannot be achieved by stirring, grounding or milling. The in-situ growth of materials on conducting agent matrix is a robust protocol to fabricate homogeneous composites.[95-99] Here the reduced graphene oxide and nanocrystal dispersions were first mixed to form homogeneous dispersion. The composite fibers of reduced graphene oxide and nanocrystals can be fabricated by electrospinning the homogeneous dispersion.

1.4 Outline

In chapter 3, the novel non-aqueous protocol based on *tert*-amyl alcohol is studied to prepare Nb:TiO_2 and the reaction parameters are investigated to fully understand the reaction mechanism and to control crystallite sizes. Further, the crystalline structure of Nb:TiO_2 is examined in detail by several state-of-art techniques including the Rietveld refinement of XRD patterns, Raman spectroscopy and XPS. The Ti^{4+} vacancies are produced after Nb doping and a fraction of Ti^{4+} ions are starting to get reduced with increasing doping level. The conductivity and electrochemical performance as anode materials of Nb:TiO_2 are measured, and the results show that 5 at% Nb:TiO_2 presents the best electrochemical performance due to the highest conductivity. The ordered mesoporous Nb:TiO_2 films are prepared by evaporation-induced self-assembly based on these nanocrystals. The porous structures are investigated by SEM images and N_2 physisorption. The results indicate that the specific surface area of mesoporous films from preformed nanocrystals is two times higher than the one from sol-gel process. The charge storage mechanisms are discussed as well and a new approach is used to quantitatively analyze the pseudocapacitive contribution. The results show that the pseudocapacitive contribution increases with the increase of conductivity.

In chapter 4, LTO and doped LTO nanocrystals are prepared based on benzyl alcohol and the reaction parameters are studied in detail. Further the crystalline structure, surface composition and formation mechanism of LTO nanocrystals are investigated by XRD, Raman spectra, XPS, FTIR, TG-MS and GC-MS. The crystals tend to aggregate at the temperature of 250 °C attributable to the benzoate on the surface. The Nb^{5+} in Nb:LTO is believed to substitute Ti^{4+} at 16*d* sites as expected, while Al^{3+} in Al:LTO not only substitutes Ti^{4+} at 16*d* sites but also Li^{+} at 8*a* sites. Both doping types can improve the conductivity. Although Al:LTO presents the highest conductivity, it does not have the best electrochemical properties. This is ascribed to the substitution of Li^{+} at 8*a* sites.

In chapter 5, the preparation parameters of mesoporous LTO powders based on sol-gel chemistry are at first elucidated. After that the porous structures with different pore size distributions are prepared based on nanocrystals and their electrochemical properties are examined by galvanostatic charge/discharge curves. The results show that the film with mesoporous pores presents a similar electrochemical performance as the film without any templates, and the macroporous film presents the best rate capacity. At last the assembly mechanisms of the preformed TiO_2 and LTO nanocrystals are explored. The results show that the differences of the zeta potentials play the key role in the different morphology of the assembled films.

CHAPTER 2
EXPERIMENTAL PRINCIPLES AND METHODS

2.1 Experimental principles

2.1.1 X-ray diffraction

Nowadays X-ray diffraction (XRD) has become the most powerful tool to analyze the crystalline structure of matter. However, it is hard to obtain the fine crystal cell information without the structure refinement. Therefore the Rietveld refinement is introduced here. As it is well-known, different information about the measured samples can be obtained from the corresponding parts of the XRD patterns. The background implies the scattering from a sample holder, Compton scattering and diffuse scattering from samples. The diffuse scattering indicates the amorphous fraction. The diffraction position gives the information about space group and qualitative phase analysis. The diffraction intensity can reflect the information of crystal structure, atomic positions and occupancy. The other important parameters from diffraction patterns are the peak shape and full width at half maximum (FWHM), which indicate the strain and domain size. To better understand the structure of unknown materials, the pattern parameters should be refined.

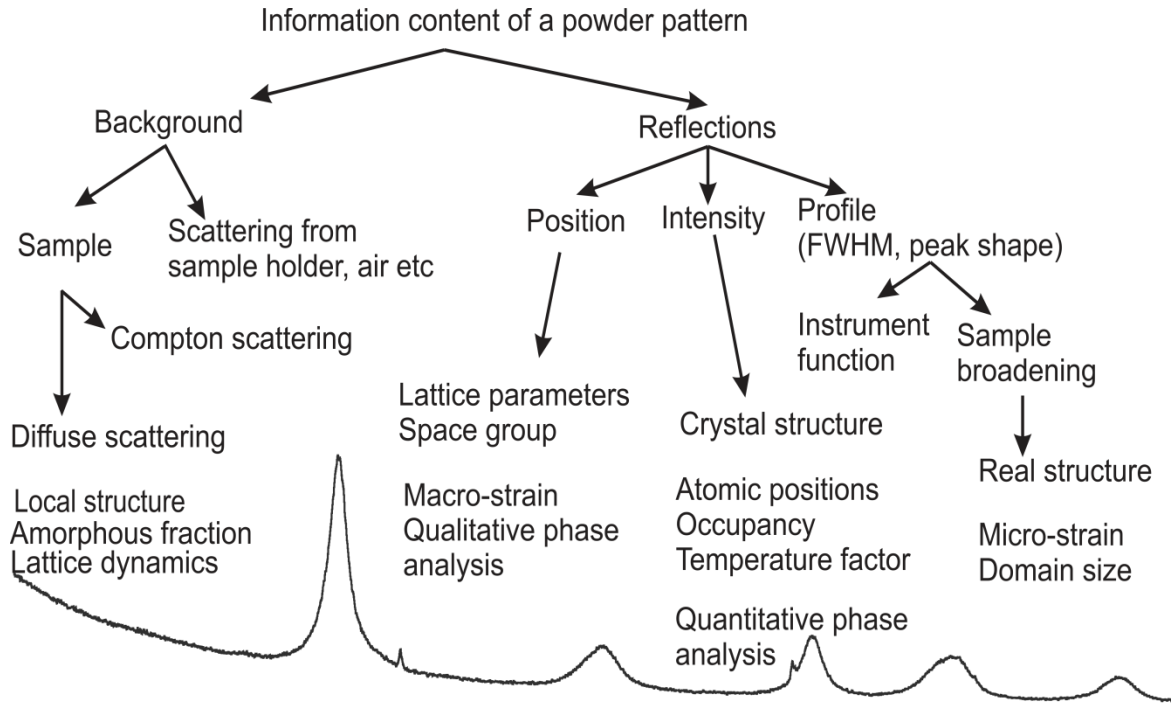

Figure 2.1 General information content of a powder diffraction pattern from Powder Diffraction Theory and Practice by Billinge and Dinnebier.[100]

The Rietveld refinement is to extract the structure parameter in mathematical expression representing the reflection intensity by least square minimization of the weighted differences between the observed and calculated intensities.[101] The following is the discussion about the mathematical expressions of the background, peak intensity, peak shape and FWHM etc.

Peak position

As mentioned above, the diffraction peak position corresponds to the distance of different crystal planes, which follows the Bragg's law. However the observed peak position can be affected by the instrumental parameters and specimen.

The instrumental factors include the axial divergence of incident beam, finite length of receiving slit of detector, zero curvature of flat samples used in Bragg-Brentano goniometer, transparency shift, and zero shift error etc. All of these factors from instruments can be minimized by the corresponding way or normalizing measurements. Taking the effect from axial divergence of incident beam for example, it can be easily minimized by using the Soller slit.

The focus here is concentrated on the position change from unit cell parameters. For a solid solution composed of A and B with the same crystalline structure, the unit cell parameter can be approximately equal to a mixture of the two constituents' unit cell parameters, described by Vegard's law:

$$a_{AxB(1-x)} = xa_{\mathrm{A}} + (1-x)a_{\mathrm{B}} \qquad (2.1)$$

Vegard's law is an empirical heuristic, which can be suitable to explain for the position change of homogeneously doped materials.

Peak shape and determination of crystallite size and lattice strain

The observed peak can be best described by the peak shape function (PSF) for PSF is the convolution of instrumental broadening, wavelength dispersion and specimen function. The instrumental broadenings are stemmed from the geometry and location of X-ray source, slits and monochromator. The wavelength dispersion depends on the nature of the source and the monochromatization technique. The specimen effects originate from the dynamic scattering and physical properties such as crystallite sizes and lattice strains.

For the symmetry peak shapes, the Gaussian function, the Lorentzian function and the PseudoVoigt function are the common mathematical models used for the analysis of peak

shape. The PseudoVoigt function is a linear combination of the Gaussian function and the Lorentzian function. The definitions are

$$G_{UA}(\mathrm{x}) = \left(\frac{g_1}{fwhm}\right) Exp\left(\frac{-g_2 x^2}{fwhm^2}\right) \tag{2.2}$$

$$L_{UA}(\mathrm{x}) = \left(\frac{l_1}{fwhm}\right) \Big/ \left(\frac{1+l_2 x^2}{fwhm^2}\right) \tag{2.3}$$

$$PV = \eta L_{AU}(\mathrm{x}) + (1-\eta) G_{AU}(\mathrm{x}) \tag{2.4}$$

for the Gaussian function, the Lorentzian function and the PseudoVoigt function, respectively; where x is ($2\theta - 2\theta_{hkl}$), *fwhm* is the full width at half maximum. $\eta = \eta_0 + \eta_1 2\theta + \eta_2 2\theta^2$, is the PseudoVoigt mixing parameter, which is in the range of 0 to 1. η_0 , η_1 and η_2 are free variables.

The relation between *fwhm* and 2θ can be described as $fwhm^2 = U\tan^2\theta + V\tan\theta + W$ for the Gaussian component of the peak shape, and $fwhm = X\tan\theta + Y/\cos\theta$ for the Lorentzian component, where *U*, *V*, *W*, *X* and *Y* are the refined parameters. To achieve the precise description and enhance the asymmetrical approximation, in our case, the Thompson modified PseudoVoigt function was applied for the peak shape fitting. An advantage of the Thompson modified PseudoVoigt function is the separation of the contributions to *fwhm* from the Gaussian and the Lorentzian component, where the Gaussian component is ascribed to the instrumental effects and the Lorentzian component represents the effect from specimen broadening. The Thompson modified PseudoVoigt function employs multi-term Simpson's integration. The *fwhm* and mixing parameter can be written by

$$fwhm = \left(\sum_{i=0}^{5} a_i \, fwhm_G^{5-i} \, fwhm_L^{i}\right)^{1/5} \tag{2.5}$$

$$\eta = \sum_{i=1}^{3} b_i \left(\frac{fwhm_L}{fwhm}\right)^i \tag{2.6}$$

where a_i and b_i are tabulated coefficients. Furthermore,

$$fwhm_G = 2\sigma\sqrt{2\ln 2}, \sigma = \sqrt{U\tan^2\theta + V\tan\theta + W + P/\sin^2\theta} \tag{2.7}$$

$$fwhm_L = (X + X_a\cos\phi)/\cos\theta + (Y + Y_a\cos\phi)/\tan\theta \tag{2.8}$$

The Gaussian *fwhm* is modified by an additional broadening parameter P and the Lorentzian *fwhm* is modified by the anisotropic broadening parameters X (crystallite size) and Y (lattice

strain). Therefore from the parameter of X and Y in Lorentzian part, the information about the crystallite size (p, A) and lattice strains (s) can be obtained in following way,

$$p_{iso} = p_{\perp} = \frac{180K\lambda}{\pi X} \quad (2.9)$$

$$p_{\parallel} = \frac{180K\lambda}{\pi(X + X_a)} \quad (2.10)$$

$$s_{iso} = s_{\perp} = \frac{\pi}{180}(Y - Y_{instr})*100\% \quad (2.11)$$

$$s_{\parallel} = \frac{\pi}{180}(Y + Y_a - Y_{instr})*100\% \quad (2.12)$$

where $\perp$ and || denote the perpendicular and parallel to anisotropy axis respectively and Y_{instr} is the instrumental part for strain broadening.

Peak intensity and quantitative analysis of phases

The quantitative analysis of each phase is based on the facts that the intensity of each set of patterns is corresponding to the amount of each phase and each phase possesses one and only one independent set of patterns.

The calculated intensity of each step ($2\theta_i$) for all phases can be written by

$$I_i = \sum_n S_n \sum_H L_{H,n} \left|F_{H,n}\right|^2 \varphi(2\theta_i - 2\theta_{H,n}) + I_{bi} \quad (2.13)$$

Where S is the scale factor, L is the Lorentz factor, F is the structure factor, and I_{bi} is the intensity of background. For a phase α, the scale factor can be described by

$$S_\alpha = K\frac{v_\alpha}{V_\alpha} = \frac{Km_\alpha}{Z_\alpha M_\alpha V_\alpha} \quad (2.14)$$

Where K is a constant, m_α is the mass content of α phase, Z_α, M_α and V_α are the molecular number, mass and volume of α phase respectively. By the refinement, the scale factor of each phase can be obtained and the corresponding mass content can be calculated as well.

Evaluation of refinement

The common way to evaluate the goodness of the refinement is the least square minimization of the weighted differences between the observed and calculated intensities. The weighted profile R value, R_{wp}, is defined as

$$R_{wp} = \left\{ \sum_i w_i \left[y_i(\text{obs}) - \text{y}_i(\text{calc}) \right]^2 / \sum_i w_i \left[y_i(\text{obs}) \right]^2 \right\}^{1/2} \qquad (2.15)$$

where $y_i(\text{obs})$ is the observed intensity at step i, $y_i(\text{calc})$ is the calculated intensity, and w_i is the weight. The R_{wp} should be approaching to statistically expected R value, defined by

$$R_{\text{exp}} = \left[(N-P) / \sum_i^N w_i y_i(\text{obs})^2 \right]^{1/2} \qquad (2.16)$$

where N is the number of observations and P is the number of parameters. The goodness-of-fit is given by the ratio between R_{wp} and R_{exp} : $\chi^2 = R_{wp} / R_{\text{exp}}$.

In this thesis, Fullprof program was used to refine the XRD patterns under the assistance of Pascal Voepel and Dr. Igor Djerdj.[102]

2.1.2 N_2 Physisorption

The adsorption and desorption isotherms of an inert gas (such as N_2, Ar or Kr) are the robust tools to analyze the surface area and pore structure of materials. During the adsorption process, the adsorbate firstly undergoes physical adsorption on materials when the equilibrium pressure p is much lower than its saturation pressure p_0 (normally $0.05 < p/p_0 < 0.35$). At this stage, the adsorption is following the Brunauer–Emmett–Teller (BET) theory and the surface area can be deduced from the BET plot. The adsorption isotherm can be expressed by the BET equation:

$$\frac{1}{v\left[(p_0 / p) - 1\right]} = \frac{c-1}{v_m c}\left(\frac{p}{p_0}\right) + \frac{1}{v_m c} \qquad (2.17)$$

where v is the adsorbed gas quantity, v_m is the monolayer adsorbed gas quantity, and c is the BET constant. The BET constant c and the monolayer adsorbed gas quantity v_m can be obtained from the slope and y-axis intersection of the linear BET plot in equation 2.17. The specific surface area can be calculated from following equation: $S_{BET} = \frac{v_m N_{\text{A}} s}{Va}$, where N_{A} is the Avogadro constant, s is the adsorption cross section of the adsorbing species, V is the molar volume of the adsorbates, and a is the mass of the absorbents.

At a high relative pressure p/p_0 (dependent on the adsorbates, pores etc.) but lower than saturated pressure, the pores became filled with condensed liquid instead of multilayer vapor. This process is called capillary condensation. Due to surface tension and capillary shape, the condensed liquid presents a meniscus shape. The Kelvin equation can be used to describe the

relationship of the meniscus curvature and liquid/vapor surface tension at the equilibrium pressure. The equation can be written by:

$$\ln\left(\frac{p}{p_0}\right) = -\frac{2H\gamma V_l}{RT} \qquad (2.18)$$

where H is the curvature of the meniscus, γ is the liquid/vapor surface tension and V_l is the molar volume of the liquid. According to this equation, the larger radius of meniscus curvature results in a higher equilibrium pressure of capillary condensation. The radius of curvature corresponds to the pore size and thus a bigger pore brings about a higher equilibrium pressure of capillary condensation. For a uniform pore size system, vapor capillary condensation would occur at constant equilibrium pressure, which leads to a sharp increase in adsorbed volume in the adsorption isotherm. For a non-uniform pore system, the adsorption branch increases gradually starting at one point. A committee of IPUC reported six kinds of N_2 adsorption and desorption isotherms at 77 K and the types IV and V possess a hysteresis behavior.[103] This hysteresis is due to several reasons. One of the explanations is condensation and evaporation processes occurring in pores with narrow necks and wide bodies, like ink-bottles. This hysteresis is derived from pore blocking effects. As the relative pressure decreases gradually at the desorption process, condensed liquid in the bottle part tends to gasify first. But the escaped path of gasified gas in the bottle part is blocked until the condensed liquid filled in the neck part gasifies (Figure 2.2 d). When the neck diameter is smaller than a critical size, the bottle can empty at the pressure P_{cav} *via* cavitation before the condensed liquid filled in neck part gasifies. The tensile stress limit of condensed liquid is independent on the pore size or adsorbents but is a feature of adsorbate. Therefore the P_{cav} is certain for certain gas, about 0.42 for nitrogen at 77.4 K, ~0.25 for argon at 77.4 K, and ~0.38 for argon at 87.3 K. [104]

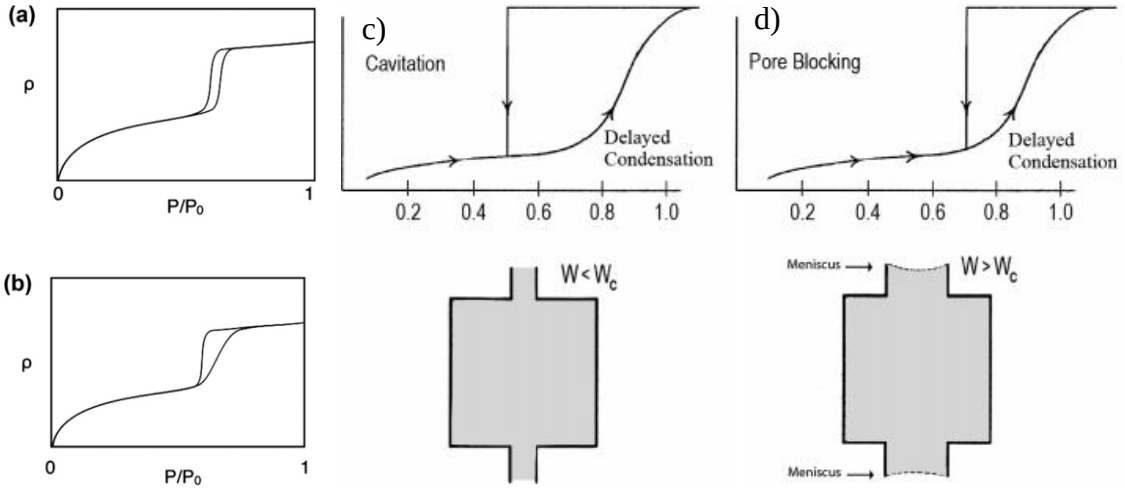

Figure 2.2 H1 (a) and H2 (b) types of hysteresis loops and schematic illustration of cavitation phenomena (c) and pore blocking (d).[105]

Although the pore size distribution can be estimated by Kelvin equation as mentioned above (Barrett-Joyner-Halenda (BJH) method is based on the modified Kelvin equation), this approach is not very accurate. The reason is that Kelvin equation is based on the assumption that the capillary condensation occurs only between two homogeneous phases--gas and liquid phases. In fact it has been recognized that metastable phases (gas-like liquid or liquid-like gas phase) exist. Subsequently some researchers introduced the surface forces at equilibrium and the stability of adsorbed liquid films into the above analysis and proposed Derjaguin-Broekhoff-de Boer theory (DBdB), giving

$$\Pi(h)V_l + \frac{\gamma V_l}{R_p - h} = RT\ln(p/p_0) \qquad (2.19)$$

The disjoining pressure $\Pi(h)$ represents the interaction between liquid and solid and is assumed to be independent on the pore curvature.[106] This method is not used as widely as BJH but is implemented as the standard procedure in all commercial physisorption instruments. The main problem for this method is that the effect of pore curvature is not taken into account of. Not like the BJH or DBdB assumption only from macroscopic point, the non-local density functional theory (NLDFT) provides the bridge between molecular level and macroscopic level. The NLDFT describes the local liquid structure dependent on curvature, which is in good agreement with molecular simulation. To obtain the pore size distribution, the experimental isotherm is regarded as the integral of the theoretical isotherms of each individual pore:

$$N_{\exp}(p/p_0) = \int_{D\min}^{D\max} N_V^{ex}(D_{\text{in}}, p/p_0)\varphi_V(D_{\text{in}})\,\mathrm{d}D_{\text{in}} \qquad (2.20)$$

where $\varphi_V(D_{\text{in}})$ is the pore size distribution function, and $N_V^{ex}(D_{\text{in}}, p/p_0)$ is the kernel of the theoretical isotherm in pores of different diameters, which is dependent on the shape of the pores.[106, 107] Many studies have shown that the pore size distribution from the calculation based on NLDFT is in good agreement with the results from SAXS and Electron Microscopy.

In this thesis, the pore size distribution was analyzed by applying NLDFT (cylindrical/spherical pores) on the adsorption branch of isotherms. The measurements on films are difficult owing to limited quantity of material. The detectable limit of surface area is around 1 m^2 in our instrument. Given the specific surface area of porous film is 100 m^2/g, the limit mass is 10 mg. In real experiments, the mass of the thin film sample is normally less than 10 mg. That means that the adsorption branch and desorption branch cannot overlap perfectly at low relative pressure.

2.1.3 Electrochemical methods

Cyclic Voltammetry (CV) is the most commonly used electroanalytical technique, where a linearly changed potential is imposed on an electrochemical system and the corresponding change of current is recorded. In the semi-infinite diffusion controlled redox reaction, the peak current at 298 K can be written by

$$i_p = (2.69\times10^5)\,\mathrm{n}^{3/2} A D^{1/2} C \upsilon^{1/2} \qquad (2.21)$$

for a reversible system, and

$$i_p = (2.99\times10^5)\,\mathrm{n}^{3/2} \alpha^{1/2} A D^{1/2} C \upsilon^{1/2} \qquad (2.22)$$

for an irreversible system, where i_p is the peak current (A), n is the number of exchange electrons, A is the surface area of electrode (cm^2), D is the chemical diffusion coefficient of active mass (cm^2/s), C is the molar concentration of active mass (mol/cm^3), υ is the scanning rate (V/s), and α is the transfer coefficient.[108] For Li^+ ion intercalation into anatase, the redox reaction is irreversible. Given the final product is $Li_{0.5}TiO_2$, C would be 0.024 mol/cm^3 and α is 0.5, therefore the Li^+ ion chemical diffusion coefficient in the system can be obtained from the CV at different scanning rates. The chemical diffusion coefficient of Li^+ ions in TiO_2 (anatase) varies from 10^{-13} to 10^{-17} cm^2/s dependent on the materials.[47, 109, 110]

Compared with CV technique, which is a transient technique and normally far from equilibrium, the electrochemical impedance spectroscopy (EIS) can measure the systems under a steady state after a small perturbation of an AC voltage. In the EIS measurements,

small amplitude of alternative voltage is imposed on an electrochemical system, and the impedance is measured over a range of frequencies. The frequency of alternative voltage can be tuned from 10^6 to 0.01Hz and the impedance responses at different frequencies represent different interfacial information. For instance, the response signals in an intercalation reaction represent different kinds of reaction processes including Li^+ ions migration through surface films, interfacial charge-transfer, solid state Li^+ ion diffusion, and accumulation (sorption) in the bulk *via* a phase transition. To analyze the response signals, a reasonable corresponding equivalent circuit should be proposed. The determination of equivalent circuit is a challenging work, which can strongly vary with different reaction systems. Generally speaking, at the high frequency, the impedance is mainly attributed to the migration of Li^+ ions through the SEI (solid electrolyte interphase) films. This resistance is normally in the range of 5~20 Ω. At the medium frequency, the impedance is normally derived from charge transfer process between the SEI film or conductive additives and active materials. At the low frequency, the impedance is mainly from bulk materials: one part is the Li^+ ions diffusion in bulk materials (named as Warburg resistance) and the other part is the accumulation or sorption of lithium or other capacitive effects.[111] The chemical diffusion coefficient D can be deduced from the Warburg coefficient and the equation can be written by

$$D = \frac{1}{2}\left[\left(\frac{V_M}{S_W F A}\right)\left(\frac{dE}{dx}\right)\right]^2 \qquad (2.23)$$

where V_M is the molar volume, S_W is the Warburg coefficient, dE/dx is the slope of the coulometric titration curve, F is the Faradic constant and A is the surface area.[112] S_W can be obtained from slope of $|Z'|$ vs. $\omega^{-1/2}$ plot (ω is the angular frequency) in the Warburg region.

Although there are plenty of reports about calculating the chemical diffusion coefficient of Li^+ ions in anatase and LTO through the above methods, these obtained results vary in several magnitudes. The Li^+ ion intercalation reaction in anatase and LTO contains the phase transformation and interface migration (boundary transfer), but the above discussion about CV and EIS does not involve the interface migration process.[113-116]

Electrical conductivity

The conductors can be divided into electronic conductors, ionic conductors and mixed conductors according to the elements that play the role of the current carriers. For electronic conductors, the carriers are electrons and holes, while for ionic conductors they are cations and anions. In order to distinguish the ionic conductivity and electronic conductivity, Hebb-

Wagner method was established and successfully applied in this field.[117, 118] Taking the measurements of electronic conductivity of silver sulfide for example, the suppression of ionic conductivity can be achieved by using inert electrode such as platinum or graphite. For the measurement of ionic conductivity, the suppression of electronic conductivity can be accomplished by using silver iodide as blocking electrode, for silver iodide is a good Ag^+ conductor but a poor electronic conductor. The relationship between the ionic conductivity and the ionic diffusivity (diffusion coefficient) was described by Nernst-Einstein equation:

$$D_i = \frac{\mu_i RT}{z_i F} \text{ and } \sigma_i = \mu_i c_i z_i F \text{, therefore } \sigma_i = \frac{c_i z_i^2 F^2}{RT} D_i ,$$

Where D_i is the diffusivity ($cm^2\ s^{-1}$), σ_i is the ionic conductivity ($S\ cm^{-1}$), μ_i is the ionic mobility ($cm^2\ V^{-1}\ s^{-1}$), z_i is the charge number of the ion (i), c_i is the molar concentration of charged particle i ($mol\ cm^{-3}$), R is the gas constant ($8.314\ J\ mol^{-1}\ K^{-1}$), F is the Faraday constant ($96485\ C\ mol^{-1}$) and T is the temperature (K). If the ionic conductivity can be measured by an experiment, the ionic diffusivity can be deduced from the above equation. For the measurement of ionic conductivity of LTO and doped LTO, several measurement systems were established: for electrical conductivity, measurements were conducted on a pallet coating with gold on both sides by EIS. For electronic conductivity, an inert gold electrode can be used as a positive blocking electrode and lithium metal was used as a negative electrode. However this system is not stable for lithium metal can reduce LTO to form Ti metal on the surface. Only electrical conductivity was carried out in this thesis.

2.1.4 X-ray Photoelectron Spectroscopy

X-ray Photoelectron Spectroscopy (XPS) has been intensively applied to analyze the surface chemistry of materials including surface composition, chemical state and bonding configuration. The principle behind XPS is the photoelectric effect: when X-ray energy exceeds the binding energy of electrons at core level, such electrons will escape into the Free State. Then the kinetic energy of photoelectrons can be determined. The binding energy of core level electron can be deduced by subtracting the kinetic energy of X-ray source. The binding energy is characteristic for each element. In addition, the intensity of XPS peaks is related with the content of each element, which provides an approach to perform the quantitative analysis. XPS is a surface sensitive technique because only the electrons ejected from the surface (around 1 to 10 nm deep) can be detected without energy loss. Besides, the in-depth XPS can provide the information of element distribution information along the sample depth.

2.1.5 Raman spectroscopy

Raman spectroscopy is a spectroscopic technique based on Raman scattering of monochromic laser light to observe vibrational, rotational, and other low-frequency modes of materials. The Raman Effect can be considered as the inelastic scattering of electromagnetic radiation. During this interaction, energy is transferred between the photons and the molecular vibrations. Therefore, the scattered photons have a different energy from the incoming photons. According to the group theory, each phase possesses a set of characteristic Raman modes. Raman spectroscopy is a powerful tool to analyze the phase structure of materials.

2.2 Experimental methods

2.2.1 Materials

Titanium (IV) chloride (99.0%), titanium (IV) ethoxide (97%), titanium (IV) *iso*-propoxide (97%), titanium (IV) butoxide (97%), niobium (V) ethoxide (99.95%), aluminium (III) *iso*propoxide (98.0%), 2-methoxyethanol (99.8%), anhydrous lithium acetate (99.999%), glacial acetic acid (99%), benzyl alcohol (99.8%), lithium ribbon (99.9%) were purchased from Sigma-Aldrich. 1-hexanol, 1-octanol, *tert*-amyl alcohol are from abcr GmbH. 1M $LiPF_6$ in EC:DEC (3:7) were obtained from Powerlyte. Whatman GF/A glass microfiber membrane was used as separator here purchased from Sigma-Aldrich. Poly(ethylene oxide) average Mv 1000000 was from Sigma-Aldrich, here referred as PEO 1000K.

Poly(isobutylene)-*block*-poly(ethylene oxide) ($H[C(CH_3)_2CH_2]_{50}C_6H_4(OCH_2CH_2)_{45}OH$) was obtained from BASF SE, here referred as PIB_{50}-*b*-PEO_{45} or PIB 3K.

2.2.2 Characterization methods

Scanning electron microscopy (SEM) and bright-field transmission electron microscopy (TEM) images were obtained on a LEO GEMINI 982 and a CM30-ST microscope from Philips, respectively. Powder X-ray diffraction (XRD) measurements were carried out on an X'Pert PRO diffractometer from PANalytical instruments. Rietveld refinements were performed with Fullprof software using Thompson–Cox-pseudo-Voigt peak function. The grain size was calculated based on anisotropic Lorentzian size broadening. X-ray photoelectron spectroscopy (XPS) data were acquired on a VersaProbe PHI 5000 Scanning ESCA Microprobe from Physical Electronics, with monochromatic Al Kα X-ray source. The C 1s signal from adventitious hydrocarbon at 284.8 eV was used as energy reference to

correct for charging. Nitrogen physisorption measurements were carried out at 77 K using an Autosorb-6-MP automated gas adsorption station from Quantachrome Corporation. Raman spectra were collected on a SENTERRA dispersive Raman microscope from Bruker Optics equipped with an objective from Olympus (MPlan N 100x) and a Nd:YAG laser (λ = 532 nm, P = 0.2 mW). Thermal gravimetric analysis (TGA) data were acquired on a Netzsch STA 409 PC. The thermobalance was coupled to a Balzers QMG 421 quadrupole mass spectrometer. The ionization energy was 70 eV. Fourier transform infrared (FTIR) spectra were obtained on a Bruker IFS-48 spectrometer. Optical absorption measurements were conducted on a Perkin-Elmer Lambda 750 UV-Vis-NIR spectrophotometer, equipped with a Praying-Mantis diffuse reflectance accessory. For crystal structure visualization, the software Crystal Impact Diamond version 3.2i was used. GC-MS analyses were conducted using an Agilent 5973 MSD with 6890 gas chromatograph.

CHAPTER 3
NB:TIO_2 NANOCRYSTALS: CRYSTALLINE STRUCTURE, SIZE CONTROL, SELF-ASSEMBLY AND ELECTROCHEMICAL PROPERTIES

3.1 Preparation of Nb:TiO_2 nanocrystals

The preparation of Nb-doped TiO_2 (Nb:TiO_2) was accomplished by a microwave-assisted non-aqueous reaction. The illustration of this process is presented in Figure 3.1. In order to obtain homogenously doped nanocrystals, stoichiometric amounts of $TiCl_4$, $Ti(OEt)_4$ and $Nb(OEt)_5$ were mixed at 75 °C for 1 min. 3 mL 1-hexanol were added into the precursors. An alcohol exchange reaction took place at 110 °C for 1 min. 2 mL *tert*-amyl alcohol were added to initiate the condensation reaction at 140 °C for 5 min. Afterward, the nanocrystals were precipitated in 50 mL of pentane and collected by centrifugation. These nanocrystals were washed with diethyl ether for three times and dried at room temperature. In order to obtain the similar crystallite size, the condensation reaction time for doped TiO_2 extends one minute.

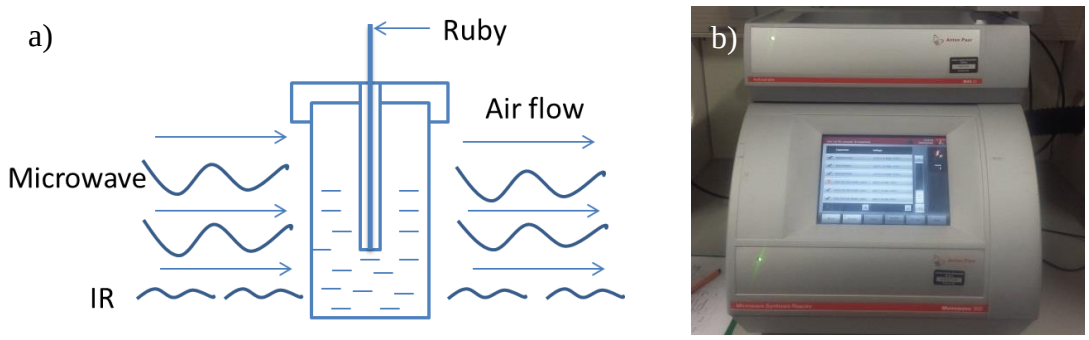

Figure 3.1 (a) Illustration of a microwave-assisted reaction. There are two temperature sensors (IR sensor (outside) and Ruby (inside the solution)). Here the Ruby sensor was used to monitor the temperature. Air flow is used to cool down the system. (b) A photograph of the Monowave 300 microwave reactor from Anton Paar.

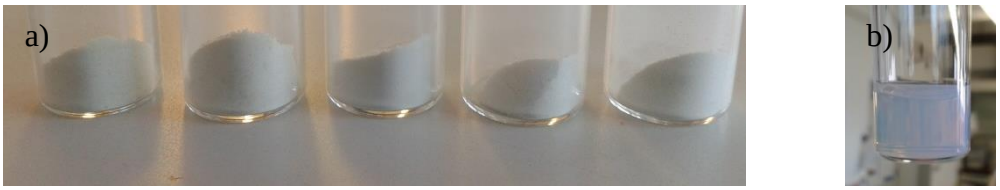

Figure 3.2 (a) Nb:TiO_2 nanocrystals with different Nb contents (from left to right: TiO_2, 2 at%, 5 at%, 10 at% and 20 at% Nb:TiO_2) and (b) TiO_2 dispertion in ethanol (around 5 wt%).

Nb:TiO_2 nanocrystals can be successfully synthesized by a microwave-assisted non-aqueous reaction with a high yield of more than 90%. The photographs of as-made nanocrystals and TiO_2 dispersion in ethanol are shown in Figure 3.2. Nb:TiO_2 nanocrystals have almost the same colour, which indicates that the doped nanocrystals have no absorption of the visible light. Due to residual surface components, Nb:TiO_2 nanocrystals possess a high dispersibility in polar solvents (20 wt% in water and 10 wt% in ethanol). The thermogravimetric analysis

(showing in Appendix Figure 1) indicate 5 to 8 wt% residual organic compounds. In order to avoid the effect of the residual compounds on their properties, the as-made nanocrystals were anealed at 400 °C for one hour. The characterizations were carried out on the annealed nanocrystals without the specific explanation. The specific surface area were nearly the same from the BET plots, 155, 170, 165 and 195 m^2/g for TiO_2, 2 at%, 5 at% and 10 at% Nb:TiO_2 nanocrystals. The Nitrogen physisorption isotherms were shown in Appendix Figure 1 as well.

3.2 Microstructure of Nb:TiO_2 nanocrystals

3.2.1 Morphology of Nb:TiO_2 nanocrystals

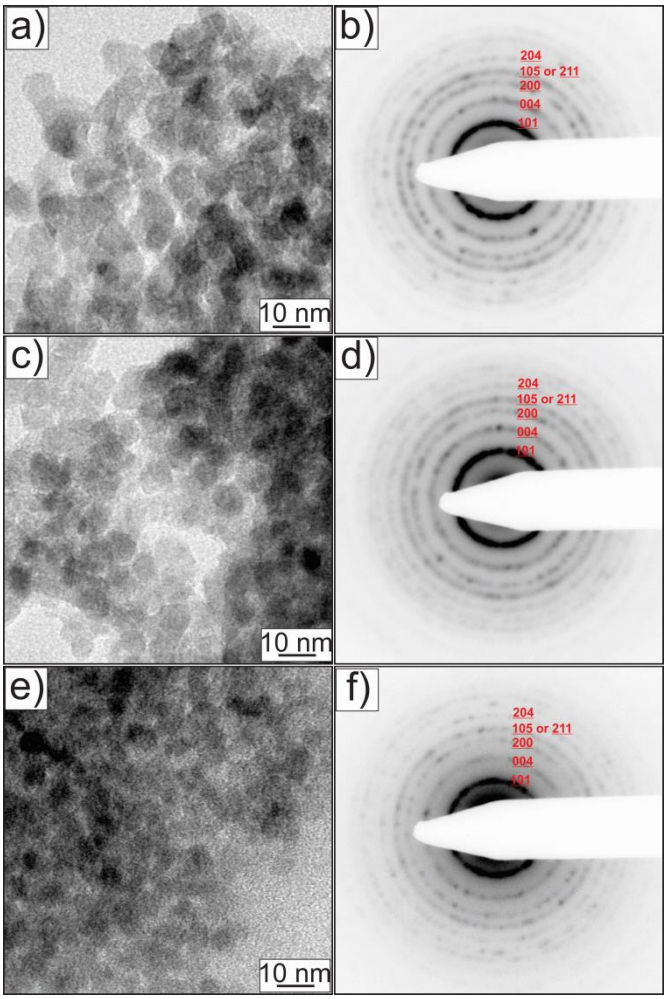

Figure 3.3 TEM images and selected area electron diffractions of Nb:TiO_2. (a) and (b) 2 at% Nb:TiO_2; (c) and (d) 5 at% Nb:TiO_2; (e) and (f) 10 at% Nb:TiO_2.

Nb:TiO_2 nanocrystals were investigated by bright-field transmission electron microscopy (TEM), and results are shown in Figure 3.3. From the TEM images, the nanocrystals present sherical sphapes and the average particle sizes for 2 at%, 5 at% and 10 at% Nb:TiO_2 are 8.0 ± 0.5, 7.5 ± 0.5 and 6.0 ± 0.5 nm, respectively. With the increase of doping level from 2 at% to 10 at%, the particle sizes decrease around 2 nm. The lattice planes can be clearly observed in

high resolution TEM images of Nb:TiO_2, which confirms the good crystallinity. The electron diffraction patterns in SAED can be assigned to the (101), (004), (200), (105) or (211) and (204) crystalline planes of the anatase phase according to JCPDS card 021-1272. The clear electron diffraction rings can prove the good crystallinity as well.

Table 3.1 Dispersibility, particle and crystallite sizes, BET surface area and Nb contents of Nb:TiO_2 nanocrystals. Particle size, crystallite size and Nb content information are from TEM, Rietveld refinements and XPS, respectively.

Samples	Dispersibility in ethanol / wt%	Particle size / nm	Crystallite size / nm	BET surface area / m^2/g	Nb content / at%
TiO_2	> 9	-	6.4	155	-
2 at% Nb	> 7	8.0 ± 0.5	6.3	170	2.3
5 at% Nb	> 10	7.5 ± 0.5	6.5	165	4.9
10 at% Nb	> 10	6.0 ± 0.5	5.5	195	9.7

3.2.2 Microstructure of Nb:TiO_2 nanocrystals

Herein several state-of-art technologies including XRD with the Rietveld refinement, Raman spectroscopy and XPS were used to analyze the crystalline structure of Nb:TiO_2 nanocrystals.

XRD patterns of Nb:TiO_2 with different doping levels are shown in Figure 3.4(a) and all patterns present the characteristic anatase phase (space group $I4_1/amd$) in accordance to the JCPDS card 021-1272. All XRD patterns were analyzed by the Rietveld refinement using the FullProf program.[102] Only the TiO_2 results are shown here and the rest are shown in Appendix Figure 2. All patterns can be fitted very well. The value of χ^2 are 1.75, 1.55, 2.08 and 3.21 for TiO_2, 2 at%, 5 at% and 10 at% Nb:TiO_2 patterns, respectively, which confirm the good refinement. The unit cell parameters a, b and c linearly increase with the increase of Nb doping levels (see Figure 3.4(b)). The increase in unit cell parameters is attributed to the substitution of Ti^{4+} with the bigger cations Nb^{5+}. The linear relationship implies the homogeneous distribution of Nb^{5+} in anatase structure in all doping levels. These results prove the good incorporation of Nb^{5+} ions into anatase lattice. From the refinement, the crystallite sizes are 6.4 ± 0.2, 6.3 ± 0.3, 6.5 ± 0.2, and 5.5 ± 0.2 nm for TiO_2, 2 at%, 5 at% and 10 at% Nb:TiO_2 respectively. The smallest crystallite size of 10 at% Nb:TiO_2 is on account of the highest doping level.[66] Generally speaking, the differences in crystallite sizes of these nanocrystals are quite small (in one nanometer). The similar crystallite sizes can eliminate the impact of the crystallite sizes on the electrochemical performance.

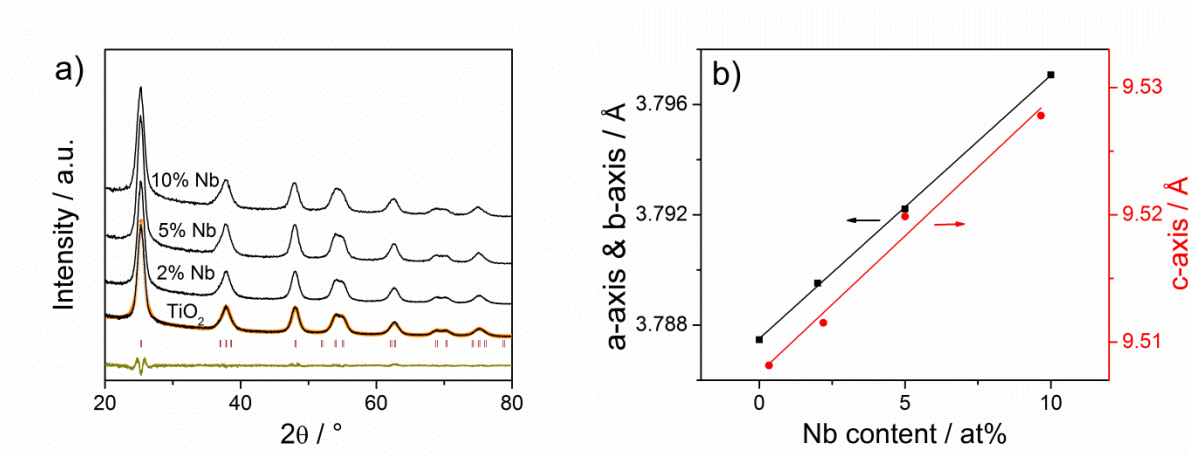

Figure 3.4 (a) XRD patterns of annealed doped TiO_2 nanocrystals. Only the refinement of TiO_2 pattern is shown. The orange curve represents the fitting curve, the dark yellow curve is the difference between observed and calculated curves, and the wine bars stand for the position of diffraction peaks. (b) Unit cell parameters change with Nb content.

Raman spectra of Nb:TiO_2 are shown in Figure 3.5. The Raman bands located at 146, 197, 394, 516 and 641 cm^{-1} can be assigned to the E_g, E_{1g}, B_{1g}, A_{1g} and B_{1g}, and E_g vibration modes of the anatase phase according to literature, respectively.[119-121] No rutile or other TiO_2 phases are found. With the increase of the Nb doping levels, the first E_g band shifts to higher energy, while the B_{1g} band shifts to lower wavenumbers. The position shift of the Raman bands can normally be caused by non-stoichiometry or phonon confinement effects. Because the crystallite sizes of Nb:TiO_2 are nearly the same, the phonon confinement effects should be similar. Such changes could be derived from the non-stoichiometry (vacancies of Ti^{4+} after Nb^{5+} doping) and the formation of Nb−O−Ti bonds.[83, 122] A broad, weak scattering band marked by an asterisk at ~850 cm^{-1} in Figure 3.5 is attributed to the vibration mode of the terminal Nb=O bonds, which is typically presenting as network termination in amorphous NbOx.[83, 123, 124] Such peak is only observed in the sample with a high Nb concentration, here only in 10 at% Nb:TiO_2 spectroscopy. It has been proven that the Nb atoms have the trend to accumulate on the surface of Nb:TiO_2 when exposed to ambient atmosphere.[125, 126]

The FTIR spectra of Nb:TiO_2 are shown in Figure 3.5b. The strong vibration bands located at 3400 and 1630 cm^{-1} are assigned to O−H stretching vibration and bending vibration from adsorbed water. Three vibration bands located 465, 556 and 643 cm^{-1} are attributed to Ti−O stretching and Ti−O−Ti bridging stretching modes.[124, 127] Two vibration bands located at 802 and 901 cm^{-1} are probably attributed to Ti−Cl bonds, which are from residual precursors.

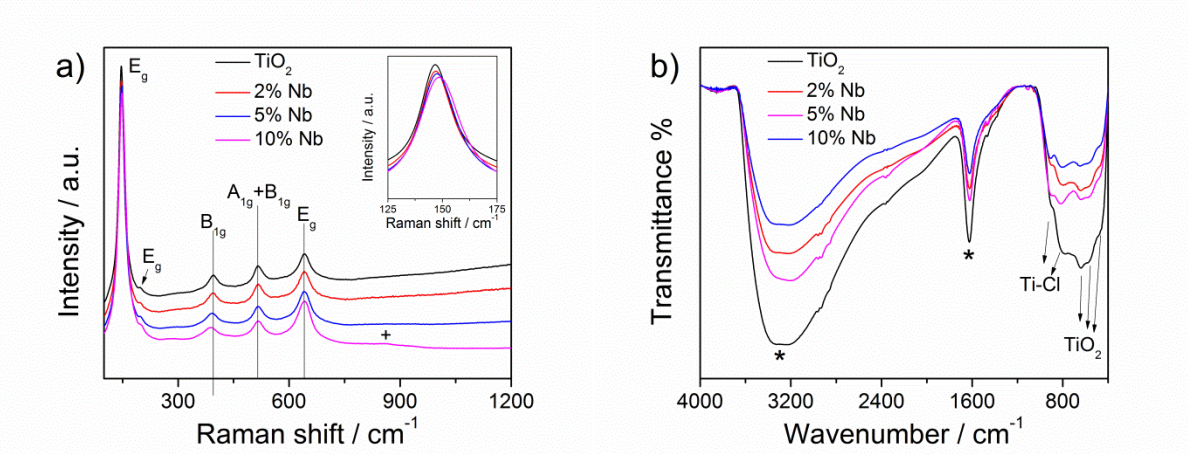

Figure 3.5 (a) Raman spectra of annealed Nb:TiO_2 nanocrystals with different Nb contents. The inset figure is the first E_g band at 125 to 175 cm^{-1}. The "+" stands for the band of Nb=O. (b) Normalized FTIR spectra of annealed Nb:TiO_2 nanocrystals. The * indicate the vibration of adsorbed water.

3.2.3 XPS measurements and proposed doping mechanism

To gain more insight into the composition and chemical state of Nb:TiO_2 nanocrystals, the high resolution XPS measurements were carried out and the results are shown in Figure 3.6. The XPS survey of Nb:TiO_2 indicate that, except from the existence of Ti, Nb, O and C elements, Cl 2p can be found at 199.36 eV as well. The Cl can be derived from residual precursors, which is confirmed by FTIR spectra. The residual precursors can further hydrolyze to make the nanocrystals possess positive zeta potential. The electrostatic repulsion between charged nanocrystals makes them to possess high dispersibility in polar solvents. With increasing Nb doping levels, the peak intensities of Nb 3d and Nb 3p increase. The Nb content for 2 at%, 5 at% and 10 at% Nb:TiO_2 from XPS analysis are 2.3 at%, 4.9 at% and 9.7 at%, respectively. The Nb content in the products is the same with the content in the precursor, which confirms that the preparation protocol of Nb:TiO_2 is successful and efficient. The detailed XPS scans of Ti 2p and Nb 3d core level are shown in Figure 3.6b. To calibrate the charging effect, the binding energy of C−C peak of adventitious C 1s is shifted to 284.80 eV. The Ti 2p spectrum of 2 at% Nb:TiO_2 presents the asymmetric doublet peak stemmed from spin-orbit splitting with binding energy of 458.78 ± 0.05 eV for $2p_{3/2}$ and splitting energy of 5.72 eV.[83] With increasing Nb content, the binding energy increases slightly to 458.86 ± 0.05 and 458.92 ± 0.05 eV with the same splitting energy for 5 at% and 10 at% Nb:TiO_2. A newly appearing peak located 456.9 ± 0.1 eV in Ti 2p spectrum of 5 at% and 10 at% Nb:TiO_2 can be assigned to the Ti^{3+}.[128] The Ti^{3+} ions take up 1.4 at% and 2.4 at% of total titanium content for 5 at% and 10 at% Nb:TiO_2. Nb 3d spectra of 2 at%, 5 at% and 10 at% Nb:TiO_2 present symmetric spin−orbit doublet with Nb $3d_{5/2}$ binding energies of 207.31, 207.37 and 207.40 eV

and the same splitting energy of 2.76 eV, which confirms niobium in its Nb^{5+} oxidation state.[129, 130] The C 1s core level spectrum can be deconvoluted into three peaks with binding energies of 284.80 ± 0.05 eV, 286.19 ± 0.05 eV and 288.87 ± 0.05 eV, assigned to C−H and/or C−C groups, C−O and O−C=O species, respectively.[76]

The optical band gaps of doped TiO_2 nanocrystals were investigated by UV-Visible absorption spectroscopy at room temperature. The optical band gap of semiconductor materials (allowed direct and indirect band gap, forbidden direct and indirect transition) can be calculated from UV-Vis absorption spectroscopy. Within the semiconductor, the extinction of light I is proportional to the exponent of the penetration distance of light (l) and reciprocal absorption length (α),

$$I=I_0\exp(-\alpha l) \quad (1)$$

Near the threshold wavelength, α is related with the band gap energy in following way:

$$\alpha h\nu=C(h\nu-E_{bandgap})^n \quad (2)$$

Here $h\nu$ is the photon energy, $E_{Bandgap}$ is the optical bandgap energy, C is a constant and n is the bandgap transition dependent exponent (0.5 for direct transition and 2 for indirect transition). We plot $(\alpha h\nu)^{1/n}$ against $h\nu$ and fit the linear part of bandgap onset. The results are shown in Figure 3.7, indicating the indirect band gap of 3.18, 3.15, 3.14 and 3.14 eV for TiO_2, 2 at%, 5 at% and 10 at% Nb:TiO_2, respectively. The value of pure TiO_2 is identical with the theoretical value and band gaps scarcely change after doping.

The data from XRD, Raman spectra and XPS provide sufficient evidences of the successful incorporation of Nb^{5+} ions into anatase lattice. Depending on the oxygen partial pressure, the temperature applied during the synthesis, and the Nb concentration, the charge compensation of Nb^{5+} substituting Ti^{4+} can be achieved by two mechanisms: one possibility is the reduction of one Ti^{4+} ion to Ti^{3+} ion for each incorporated Nb^{5+},[66] the other possibility is the formation of one Ti^{4+} vacancy per four incorporated Nb^{5+} ions.[124, 125, 130]

$$2Nb_2O_5(TiO_2) \rightarrow 4Nb_{Ti}^{\bullet} + 4e' + 8O_O^{\times} + O_2 \quad (3)$$

$$2Nb_2O_5(TiO_2) \rightarrow 4Nb_{Ti}^{\bullet} + V_{Ti}^{''''} + 10O_O^{\times} \quad (4)$$

From the XPS data, at the lower Nb content, the main compensation mechanism is to produce Ti^{4+} vacancies while it becomes a mixture of both approaches at higher Nb contents.

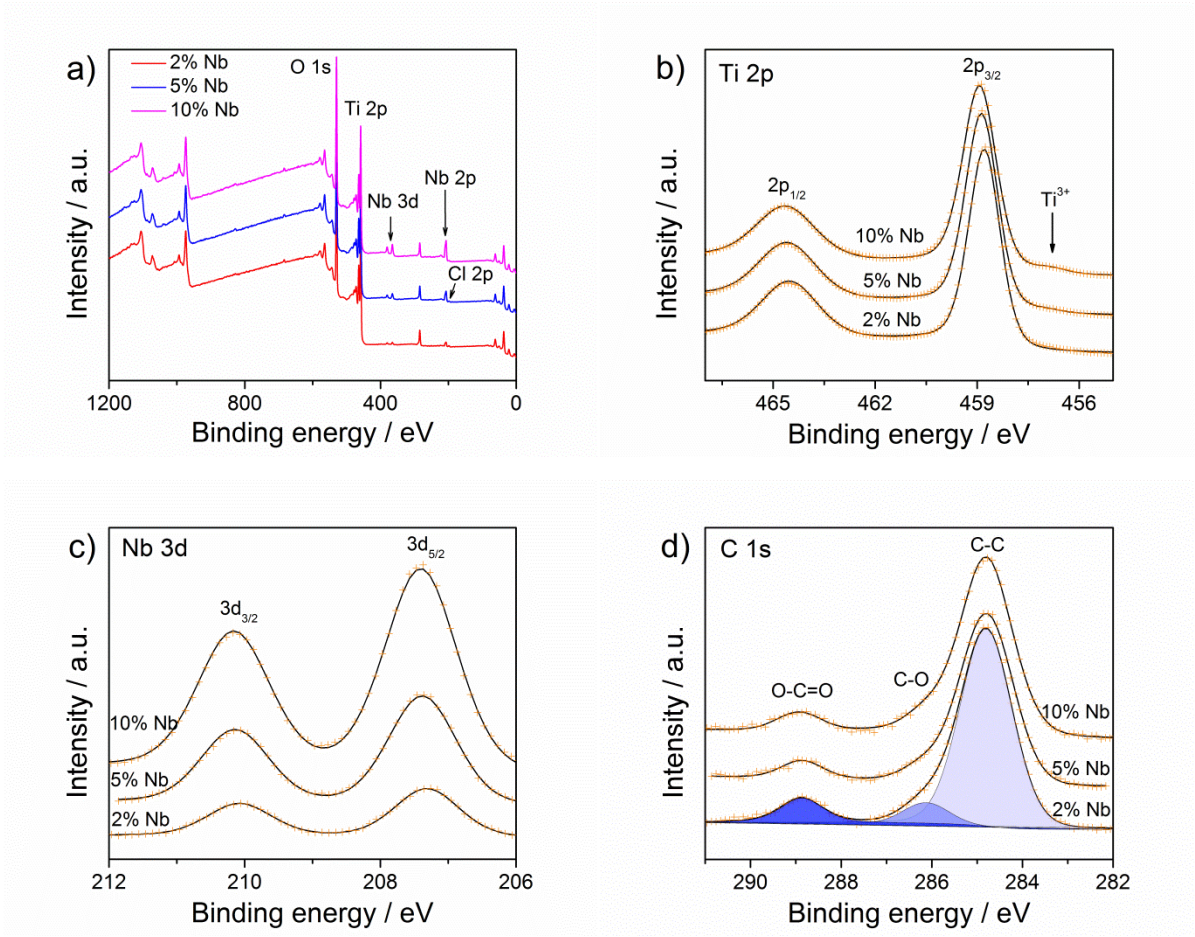

Figure 3.6 XPS surveys of Nb:TiO_2 and XPS spectra of Ti 2p, Nb 3d and C 1s core level. Orange curves represent the sum of the peak fits using mixed Gaussian-Lorentzian functions, and black curve is experimental data. The charging correction was carried out by shifting the C−C peak to 284.80 eV.

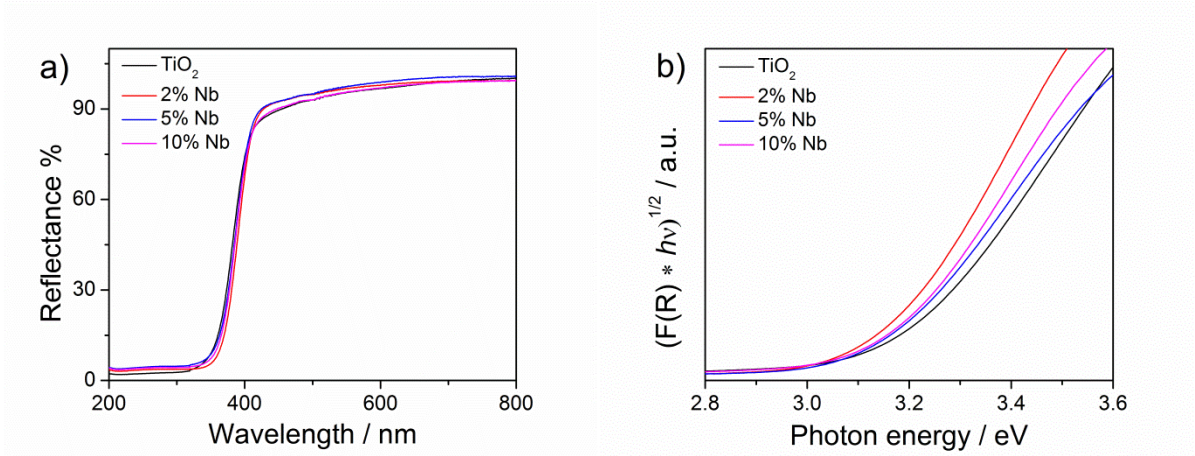

Figure 3.7 (a) UV-Visible reflectance spectra of annealed Nb:TiO_2 nanocrystals and (b) their indirect bands. Black, red, blue and magenta curves represent undoped, 2 at%, 5 at% and 10 at% Nb:TiO_2, respectively.

3.3 Crystallite sizes tuned by reaction conditions

The formation process of crystalline TiO_2 in this protocol can be divided into three steps. The first step is the preparation of the precursor $TiCl_2(OEt)_2$. The precursor is crucial for controlling the reaction rate. When $TiCl_4$ is used as the precursor, it can react with alcohols to form $TiCl_2(OR)_2$ and HCl. The side product of HCl can accelerate the condensation reaction and thus promote the formation of amorphous phase instead of crystalline phase. If $Ti(OR)_4$ is used as the precursor, due to the lower reactivity of $Ti(OR)_4$ with respect to a precursor containing a Cl group, the condensation reaction will not take place under a mild reaction condition such as a low temperature or a short reaction time. Therefore $TiCl_2(OR)_2$ is the perfect choice for the condensation reaction. The preparation of $TiCl_2(OEt)_2$ can be achieved by mixing $TiCl_4$ and $Ti(OR)_4$ with the molar ratio of 1 at the temperature of 75 °C for 1 min.[131] The second step is an alcoholysis reaction (the alcohol interchange reaction). This step controls the particles size and crystallinity. From Table 3.2, the crystallite size of anatase is around 4.0 nm without using 1-hexanol to exchange the alkoxy group, while the value is 5.9 nm when using it. The smaller crystallite size of anatase from $TiCl_2(OEt)_2$ is on account of the faster condensation reaction that induces TiO_2 nanocrystals with low crystallinity. On the other hand, increasing the length of the hydrocarbon-chain of alcohol will lead to a decrease in crystallite size owing to the steric effect. The third step is condensation reaction initiated by the appropriate benzylic or tertiary alcohol, such as *tert*-amyl alcohol, *tert*-butanol, benzyl alcohol and 1-phenyl ethanol.[64, 66, 132, 133] The reason is that such alcohols possess a higher stability after losing the OH group than primary or secondary alcohols. The condensation reaction between $Ti(Cl)_2(OR)_2$ and benzylic or tertiary alcohol forms Ti−O−Ti oxo-bridges and corresponding halides or ether. Such reaction mechanism is called halide or ether elimination reaction.[62, 63, 134]

Table 3.2 and Table 3.3 summarize the effects of different reaction conditions on the crystallite sizes, such as the reaction time, the reaction temperature, the interchange alcohols, the reactants, and the ratio between alcohols and reactants. It is clear that extending the reaction time and a higher temperature will lead to a bigger crystallite size. The ratio between solvents and reactants affects the crystallite size as well. When the solvent content increases, the crystallite size increases, for lower concentration of reactants and higher concentration of solvents can slow down the reaction process to form more crystalline structures.

From Table 3.2 can be concluded that the crystallite size can be tuned in the range of 4 to 7 nm by changing reaction conditions. Obtaining nanocrystals with bigger crystallite size using

this protocol is still a challenge. A different protocol based on benzyl alcohol was used to synthesize crystals with big crystallite sizes attributable to its higher boiling point (205 ℃) than *tert*-amyl alcohol (101 to 103℃). The condensation reaction based on benzyl alcohol can be carried out at higher temperatures and consequently results in bigger crystallite size, seeing Table 3.3.

Table 3.2 Crystallite sizes of anatase nanocrystals obtained from different reaction conditions with *tert*-amyl alcohol as the reactant. The crystallite sizes were calculated using the Scherrer equation. All experiments were conducted using a Monowave 300 microwave reactor from Anton-Paar. The temperature is controlled by an IR sensor at the first step and a ruby sensor at the second and third step. "Ratio" is the volume ratio between the solvent and reactant.

	Precursor	Solvents	Ratio/ml	Reaction step 2		Reaction step 3		Size / nm
				t/min	T/℃	t/min	T/℃	
1	$TiCl_2(OEt)_2$	hexanol	3:2	3	110	30	110	5.9
2	$TiCl_2(OEt)_2$	----	5	----	----	30	110	4.0
3	$TiCl_2(OEt)_2$	hexanol	3:2	3	110	20	110	5.0
4	$TiCl_2(OEt)_2$	hexanol	4:2	1	110	1	150	7.0
5	$TiCl_2(OEt)_2$	decanol	4:2	1	110	1	150	6.8
6	$TiCl_2(OEt)_2$	tetradecanol	4:2	2	140	1	150	6.6
7	$TiCl_2(OEt)_2$	octadecanol	4:2	2	140	1	150	6.2
8	$TiCl_2(OEt)_2$	decanol	3:3	1	110	1	150	6.3
9	$TiCl_2(OEt)_2$	decanol	2:4	1	110	1	150	6.1

The benzyl alcohol route can be applied to produce nanocrystals with bigger crystallite size. On the other hand, the as-made nanocrystals obtained from the benzyl alcohol route possess a bad dispersibility in methanol or ethanol than the ones obtained from the *tert*-amyl alcohol route. Therefore the preparation of Nb:TiO_2 for the self-assembly into mesoporous films is based on the *tert*-amyl alcohol. 5 at% Nb:TiO_2 with crystallite size of 20 nm can be obtained using benzyl alcohol with the reaction time of 90 mins and the reaction temperature of 220 °C or by annealing the as-made nanoparticles at 600 °C for 12 h. The XRD patterns of the 5 at% Nb:TiO_2 samples using different methods are shown in Appendix Figure 2b.

Table 3.3 Crystallite sizes of anatase nanocrystals obtained from different reaction conditions with benzyl alcohol as reactant. The crystallite sizes are from the calculation based on Scherrer equation. "*" means the reactor from CEM Corporation.

Precursors	Solvents	Reactants	ratio/ml	reaction step 2		reaction step 3		crystallite size/nm
				t/min	T/℃	t/min	T/℃	
$TiCl_2(OEt)_2$	octadecanol	BnOH	4:2	1	140	20	140	5.7
$TiCl_2(OEt)_2$	octadecanol	BnOH+HCl	4:2	1	140	15	140	10.7
$TiCl_2(OEt)_2$	octadecanol	BnOH	4:2	3	140	5	180	11.8
$TiCl_2(OEt)_2$	octadecanol	BnOH	4:2	3	140	5	170	11.5
$TiCl_2(OEt)_2$	octadecanol	BnOH	4:2	1	140	5	140	16*

3.4 Electrochemical performance of Nb:TiO_2 nanocrystals

The electrochemical performance of Nb:TiO_2 as anode materials for LIBs were evaluated with a half cell by galvanostatic charge/discharge profiles. The working electrodes were prepared by casting the slurry composed of 90 wt% Nb:TiO_2, 5 wt% PVDF binders and 5 wt% active carbon on an aluminum foil. The lithium metal and 1 M $LiPF_6$ in EC/DMC (50:50) solutions were used as the counter electrode and electrolytes, respectively. The batteries were assembled in an argon-filled glovebox with [O_2] < 0.5 ppm and [H_2O] < 0.5 ppm. The measurements were carried out on a MACCOR Series 4000 (Tulsa, Oklahoma) multichannel battery cycler. The nanocrystals tested here is those annealed nanocrystals prepared from *tert*-amyl alcohol.

The representative voltage-capacity curves (at 100 mA/g) of 5 at% Nb:TiO_2 for the first, fifth and 20th cycles are shown in Figure 3.8b. These profiles exhibit an intercalation and de-intercalation plateau at 1.75 and 2.0 V, respectively. These plateaus are characteristic of the transformation of anatase to $Li_{0.5}TiO_2$ and vice versa.[32, 135] The gradual slope after the plateaus indicates the interfacial charge storage derived from the small crystallite size (6.5 nm).[43, 47, 136] After 20 cycles, the Coulombic efficiency reaches 99.9 % and the overpotential (potential difference between intercalation and de-intercalation process) scarcely changes. This confirms that 5 at% Nb:TiO_2 sample possesses a good cycling stability. In comparison, 2 at% and 10 at% Nb:TiO_2 nanocrystals samples possess bigger overpotential and poor cycling stability. It has been proven that around 5 at% Nb:TiO_2 presents the best conductivity.[109, 137]

This can be the reason for the relatively good performance of 5 at% Nb:TiO_2. In the following the conductivity of doped TiO_2 will be measured and discussed.

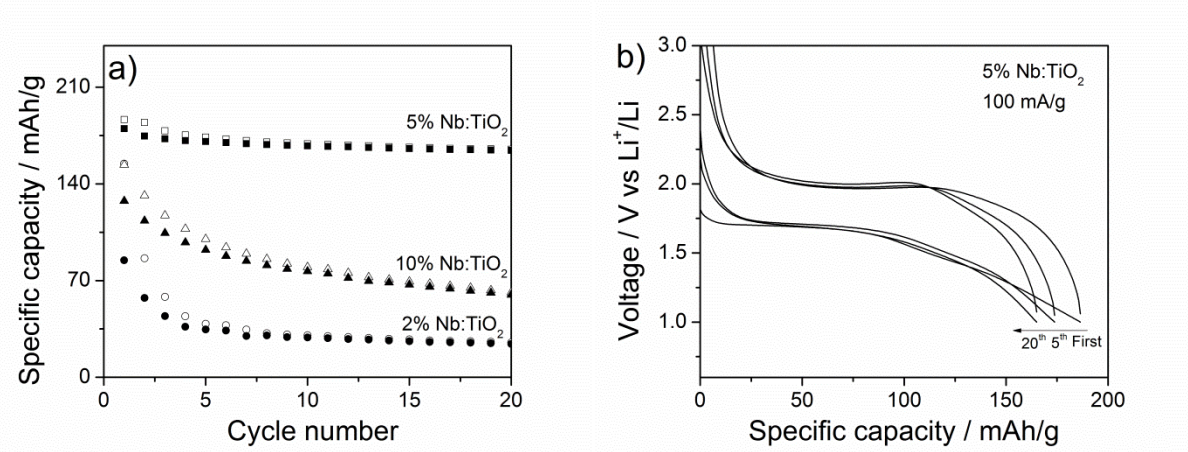

Figure 3.8 (a) The electrochemical performance of Nb:TiO_2 at the current density of 100 mA/g and (b) the corresponding galvanostatic charge/discharge profiles of 5 at% Nb:TiO_2.

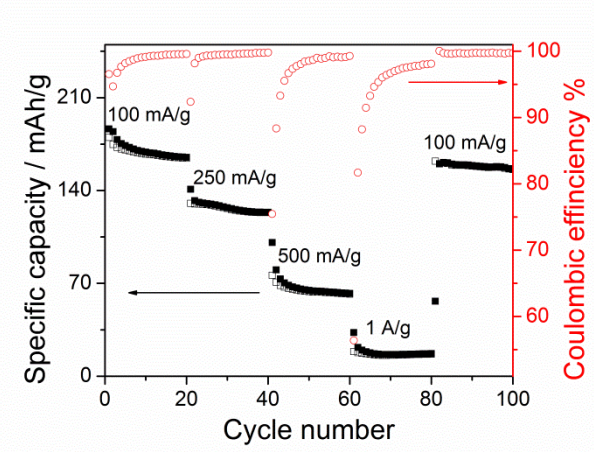

Figure 3.9 Rate capability of half-cells using the 5 at% Nb:TiO_2 nanocrystals as active electrode material and the discharge/charge current density gradually increases from 100 to 250, 500 and 1000 mA/g and back to 100 mA/g.

The rate capacity of 5 at% Nb:TiO_2 is shown in Figure 3.9. With the increase of the current density, the specific capacity decreases from 165 to 125, 63 and 17 mAh/g. When the charge/discharge current decreases back to 100 mA/g, the specific capacity is back to 160 mAh/g. The capacity loss with increasing discharge/charge current could be caused by the limitation of kinetic process involving sluggish Li^+ ion diffusion. Stievano et al. reported that 5 at% Nb doped TiO_2 nanofibers as anode material for LIBs and the results indicate that the specific capacity at 5 C is around 23 mAh/g, similar results with our nanocrystals.[138]

Although anatase TiO_2 is regarded as a promising anode material for LIBs, the results we obtained are not comparable with the results from LTO nanocrystals illustrated in the

following chapter. Comparing the data of different doping levels, 5 at% Nb:TiO_2 presents the best electrochemical performance due to its best conductivity.

3.5 Mesoporous TiO_2 and Nb:TiO_2 films

Porous films can be prepared from sol-gel process or preformed nanocrystals under the assistance of structure-directing agents. The films prepared from sol-gel process possess low boundary resistance, which is beneficial for the charge transfer process, while the films prepared from preformed nanocrystals have more accessible path and larger surface area, which is beneficial for the interfacial charge storage.[43, 139] It is hard to precisely control the crystallinity, crystallite sizes of metal oxides in the mesoporous film prepared from sol-gel process. Here the morphology and porosity of mesoporous TiO_2 films prepared from sol-gel process and preformed nanocrystals were compared in detail.

3.5.1 Preparation of TiO_2 and Nb:TiO_2 mesoporous films

The mesoporous Nb:TiO_2 films with uniform pore size and controlled wall thickness were prepared by dip-coating the nanocrystal dispersion with PIB_{50}-*b*-PEO_{45} polymers (from BASF) as SDAs on different substrates. The substrates can be ITO (for the study of electrochemical properties), glass (for the conductivity measurements), and silicon wafer (for the characterization). The nanocrystals dispersion for the dip-coating consisted of 60 mg Nb:TiO_2 nanoctrystals in 0.5 mL 2-methoxyethanol and 40 mg PIB_{50}-*b*-PEO_{45} in 1.5 mL methanol. The optimized conditions for dip-coating were a humidity of 80 RH%, a drawing rate of 10 mm/min and room temperature. The film was kept in the dip coating chamber for 5-10 min, and was subsequently transferred into an oven preheated to 120 °C for 3 h. Afterwards the film was heated up to 300 °C with a temperature ramp of 1°C/min for 6 h. The polymers can be totally removed by a heat treatment of 400 °C for 1 min with a ramp of 10 °C/min.

The dip-coating solution for preparation of mesoporous TiO_2 film from sol-gel process is composed of 400 mg $TiCl_4$ and 50 mg PIB_{50}-*b*-PEO_{45} in 3 mL ethanol. Then 250 mg water was added into the above solution drop by drop under stirring. After 1 hour stirring, the solution is ready for the dip-coating. The optimized conditions for dip-coating are a humidity of 20 RH%, a drawing rate of 3 mm/min and room temperature. The heat treatment is the same with the preparation of mesoporous film from preformed nanocrystals.

3.5.2 Morphology of TiO_2 and Nb:TiO_2 mesoporous films

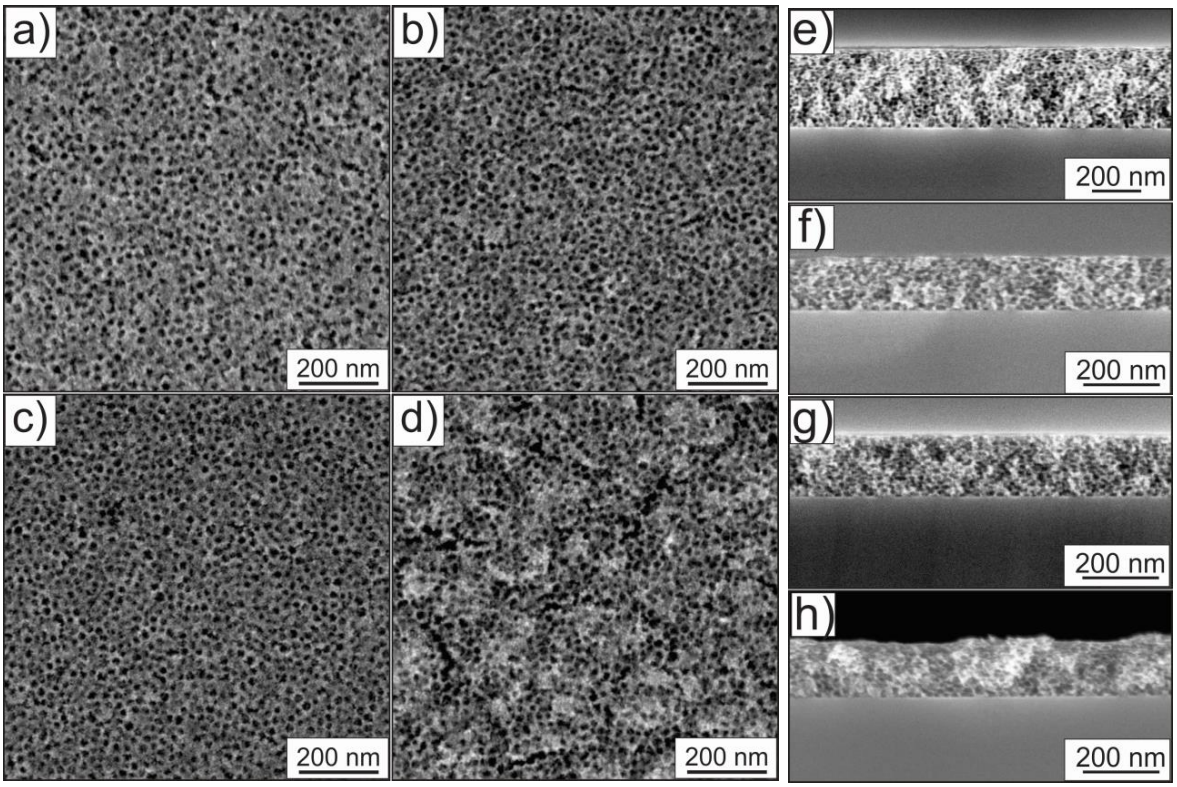

Figure 3.10 Morphology of mesoporous films from preformed nanocrystals. The images of (a), (b), (c) and (d) are top-view images for TiO_2, 2 at%, 5 at% and 10 at% Nb:TiO_2, respectively. The images of (e), (f), (g) and (f) are cross-section images for pure TiO_2, 2 at%, 5 at% and 10 at% Nb:TiO_2.

The morphologies of Nb:TiO_2 films are shown in Figure 3.10. The SEM analysis shows that mesoporous films from the preformed nanocrystals exhibit a uniform mesostructure with spherical pores and short-range ordering. The pore sizes are in a very narrow range from 15 to 18 nm. The wall thickness is in the range of 6 to 8 nm, identical with the single particle size, which indicates a good co-assembly of nanocrystals and micelles. According to the previous XPS study, there are some residual Ti−Cl functional groups on the surface of the nanocrystals, which can further hydrolyze to form protons on the surface. As a result the nanocrystals are positively charged. As we know, the PIB_{50}-*b*-PEO_{45} polymer is slightly negatively charged. Therefore the electrostatic adsorbed force is the main driving force for ordered self-assembly between nanocrystals and micelles. From the cross section images, the continuously connected porous network can be observed. The thickness of films is around 150-200 nm, which is dependent on the drying time and the drawing speed. The shape of pores in the view of cross-section direction is cylindrical due to the distortion originated from the gravity. The pores are 6 to 10 nm in height and 14 to18 nm in length.

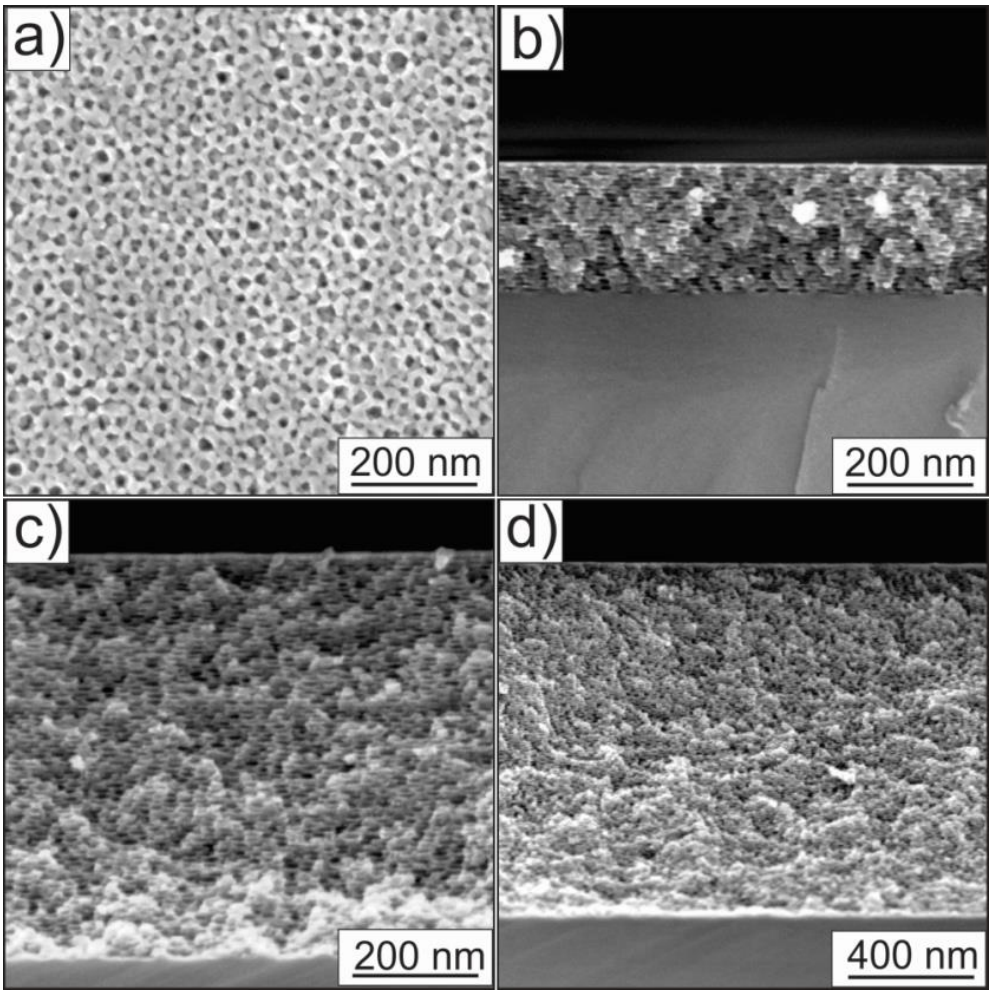

Figure 3.11 Morphology of mesoporous TiO_2 films calcined at 650 °C from sol-gel process. (a) The top-view image of single layer film. (b), (c) and (d) Cross-section images of mesoporous TiO_2 films with single layer, three layers and five layers, respectively.

The morphology of mesoporous TiO_2 from sol-gel chemistry is shown in Figure 3.11. From the top view images, the pore size of the mesoporous films prepared *via* sol-gel process is 20 to 25 nm, which is nearly the same with the size of polymer micelles and larger than the pore size (15 to 18 nm) of the film from the preformed nanocrystals. Additionally, the wall thickness of the films from the sol-gel process is around 10 to 15 nm, larger than the wall thickness of the films from preformed nanocrystals, which is on account of the high crystallization temperature. Compared with the films from preformed nanocrystals, the films from sol-gel process possess bigger connected crystals, which can facilitate the charge carrier transfer but decrease the surface area. From the cross-section images, the thickness of a film with one layer to five layers increases from 209 to 1120 nm. The average thickness of each layer is the same, which indicates there is no penetration between layers during the repeated dip-coatings. The pore distortion caused by the gravity and crystallization is much more distinct than the films from preformed nanocrystals.

3.5.3 Porosity of mesoporous TiO_2 films

The porosity was analyzed in detail *via* N_2 physisorption at 77 K. The adsorption/desorption isotherms of mesoporous films from preformed nanocrystals in Figure 3.12 show a typical type-IV shape and exhibit an H1-type hysteresis, indicating the mesoporous spherical or cylindrical pores.[140] A hybrid nonlocal density functional theory (NLDFT) model was applied to the adsorption branch based on spherical/cylindrical pores for the calculation of the pore size distribution and the result is shown in Figure 3.12b.[105] This analysis provides a pore diameter from 4 to 18 nm, which is in good agreement with the SEM results. The wide pore size distribution is derived from the distortion of the pore shapes. The total adsorbed pore volume on such film is 1.4×10^{-3} cm^3 and the calculated porosity is around 55%. The surface area from the multipoint BET for such film is around 0.734 m^2. According to the density of TiO_2 (3.89 g/cm^3), the estimated mass of TiO_2 on the film is around 4.4 ± 0.4 mg. Due to the homogenous pore distribution and thickness, the mass of such film with thickness of 100 nm is around 0.7 mg, which is used to estimate the mass for specific capacity.

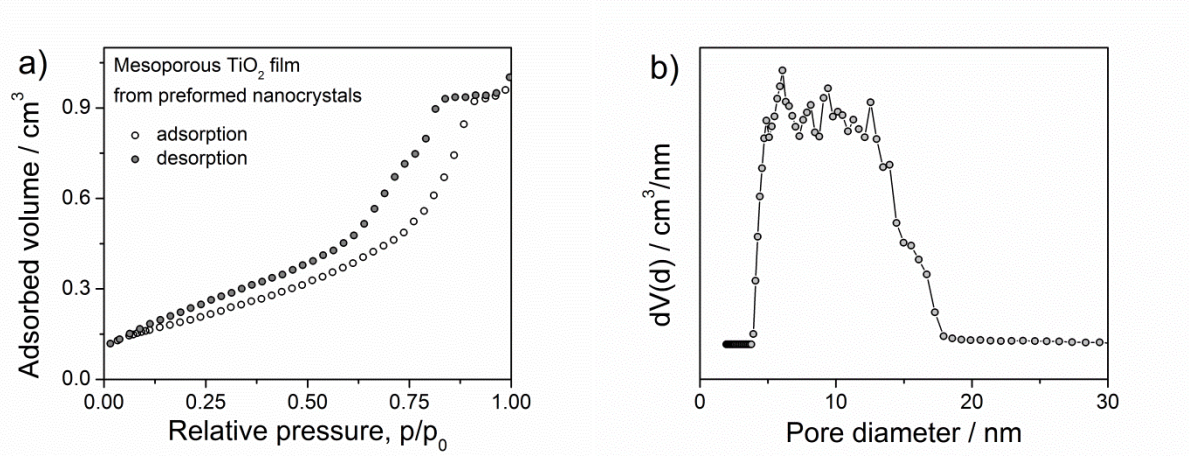

Figure 3.12 N_2 adsorption and desorption isotherms of mesoporous TiO_2 films from preformed TiO_2 nanocrystals with area of 42 cm^2 and thickness of 600 ± 50 nm. Corresponding pore size distribution is obtained by NLDFT, spherical/cylindrical pores, adsorption branch.

The analysis from the physisorption data of mesoporous TiO_2 film from sol-gel process indicates a pore size of 6 to 13 nm (seeing Figure 3.13), which corresponds to the height of the cylindrical pore in SEM cross section images. The total adsorbed pore volume in the film is 1.1×10^{-3} cm^3 and the porosity is 45%. The total surface area from multipoint BET for such films is around 0.46 m^2. Since both films used for the measurements have nearly the same amount of active materials, their surface area and porosity can be compared directly. The surface area of films from nanocrystals (0.734 m^2) is much larger than the films (0.46 m^2) from sol-gel process.

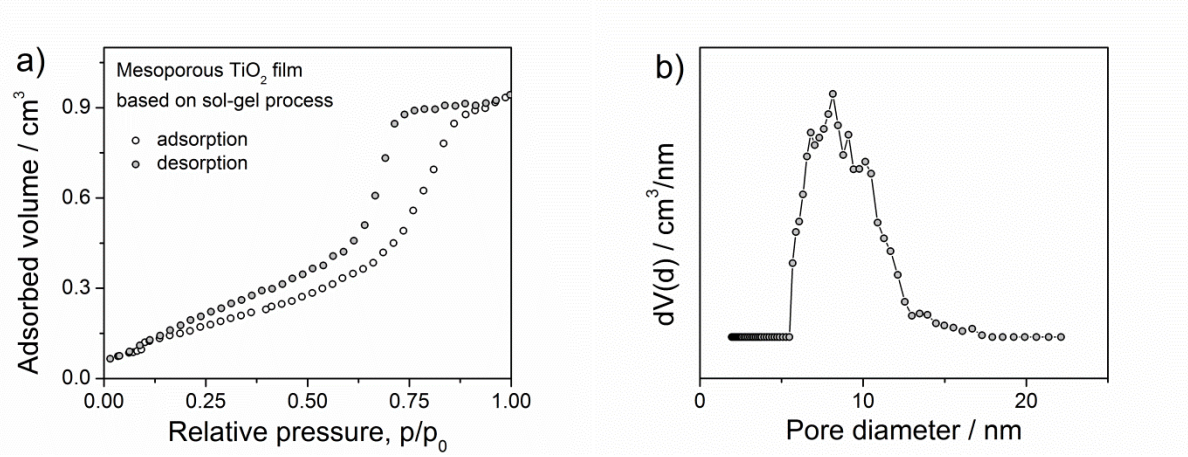

Figure 3.13 N_2 adsorption and desorption isotherms of mesoporous TiO_2 films calcined at 550 °C from sol-gel process with area of 35 cm^2 and thickness of 700 ± 50 nm. Corresponding pore size distribution is obtained on NLDFT, spherical/cylindrical pores, adsorption branch.

3.5.4 Conductivity of mesoporous Nb:TiO_2 films

The conductivity of the mesoporous Nb:TiO_2 films has been investigated by two-electrode AC impedance spectra (seeing Figure 3.14). To prevent the penetration of current through the film from top to bottom, two parallel electrodes were used to measure the conductivity of mesoporous films on an insulated substrate (here glass as substrate).[141]

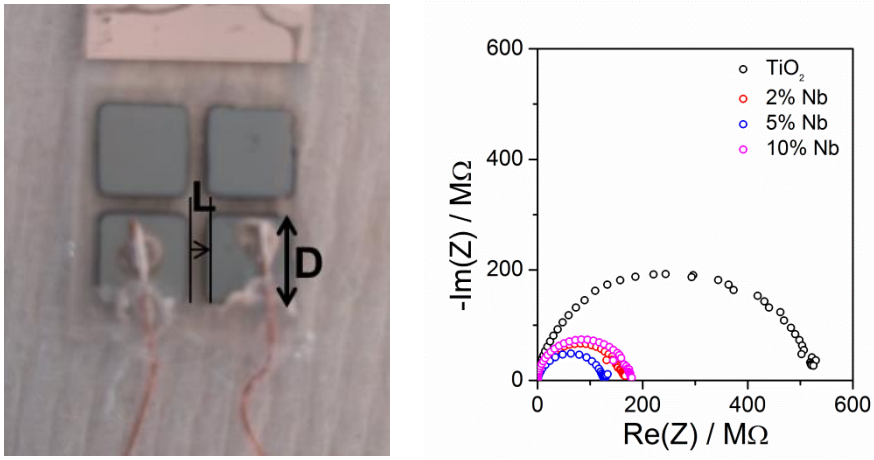

Figure 3.14 The digital picture of setup for conducticity measurements and the corresponding EIS results.

The impedance spectra are shown in Figure 3.14 and present one semicircle corresponding to the overrall resistance. The caculated conductivities are 1×10^{-5}, 7.8×10^{-5}, 9.8×10^{-5} and 7.9×10^{-5} s/cm for TiO_2, 2 at%, 5 at% and 10 at% Nb:TiO_2, respectively. Due to the vacancies and the reduced Ti ions, the conductivity increases by almost 10 times after doping.

3.5.5 Conductivity effect on pseudocapacitive contribution

It is well-known that nanomaterials can store and convert energy not only by solid state reactions but also interfacial reactions.[34, 46] The electrochemical performance of doped TiO_2 nanocrystals have been illustrated above, and the attention here will be focused on the quantification of pseudocapacitive effect and the effects of conductivity on pseudocapacitive contribution. The electrochemical properties of the mesoporous Nb:TiO_2 films were evaluated by cyclic voltammetry and galvanostatic charge/discharge profiles. The electrochemical measurement was carried out in conventional three-electrode system in 1 M $LiClO_4$ in propylene carbonate using lithium foil and lithium wire as counter electrode and reference electrode, respectively. The potential was controlled by an Autolab Potentiostat to 1.4 V and 2.5 V as the vertex potentials for the cyclic voltammetry.

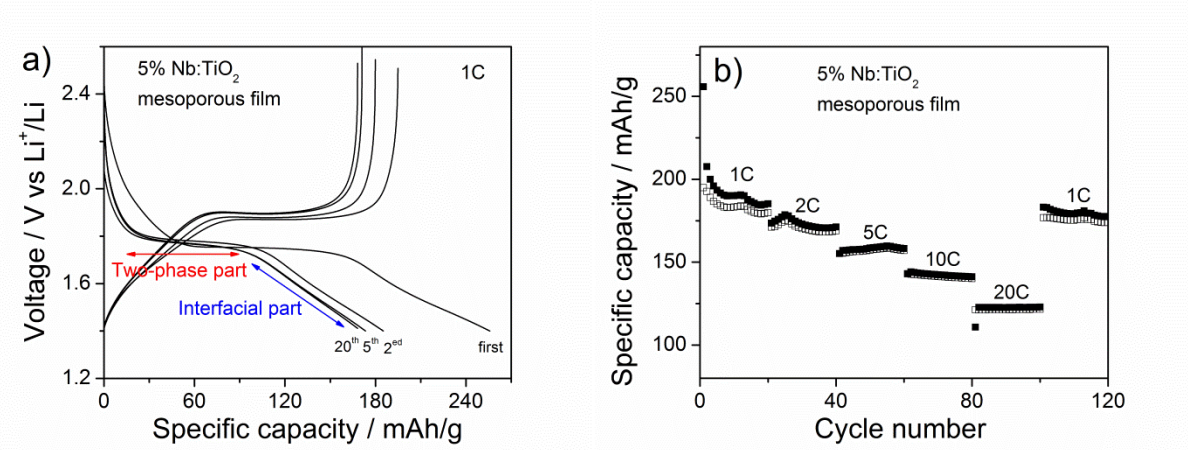

Figure 3.15 (a) Discharge and charge profiles of 5 at% Nb:TiO_2 mesoporous film and (b) Rate capacity performance of 5 at% Nb:TiO_2 mesoporous films. 1C means the discharge and charge current of 175 mA/g.

The galvanostatic profiles and rate capacities of mesoporous 5 at% Nb:TiO_2 films are shown in Figure 3.15. The first cycle shows poor Coulombic efficiency, which could be attributed to the SEI formation and trapping of Li^+ in irreversible sites.[138] The specific capacity and Coulombic efficiency become stable after five cycles. The discharge and charge plateau potentials after five cycles are 1.77 and 1.90 V, respectively, which are in good agreement with Li^+ intercalation into and extraction from anatase TiO_2. The plateau is corresponding to two phase equilibrium process between a lithium-poor phase of $Li_{0.05}TiO_2$ and a lithium-rich phase of $Li_{0.5}TiO_2$, contributing a specific capacity of around 90 mAh/g. Following the plateau is a gradient curve, which is normally assigned to interfacial charge storage. Although it is hard to accurately evaluate the pseudocapacitive contribution by the gradient curve, the rough pseudocapacitive contribution can be estimated by this to take up 47 % in total charge storage. The mesoporous thin film presents much better rate performance than nanocrystals. This could be ascribed to the improved dynamics for both electronic and Li^+ transport in

continuous mesoporous pores. At the discharge and charge rate of 20C, the specific capacity is still around 120 mAh/g. This performance is much better than the results reported in literature.[129]

The scanning rate dependent cyclic voltammetry (CV) was recognized as the most efficient and widely adopted method to quantify the pseudocapacitive contribution to the whole charge storage. The basic principle is that the total stored charges are divided into two parts: one part from solid state reaction, which is controlled by diffusion; the other part is from capacity, which is controlled by the surface area. The relationship between current and scanning rate in CV can be described by $j = av^b$ and $\log j = b\log v + \log a$. The current from intercalation reaction is proportional with the square root of scanning rates (b=0.5) while the current from capacitive contribution is proportional with scanning rates (b=1). The equation can be further written as: $j_V = k_c v + k_F v^{1/2}$ and divided by $v^{1/2}$, giving $j_V / v^{1/2} = k_c v^{1/2} + k_F$, where j_V is the current density at potential of V and v is the scanning rate. Therefore, if we can plot every current density divided by square root of scanning rates at every potential against the square root of scanning rates, the contribution from two parts can be quantified by analysis of relationship between current and scanning rate in the isolated potential rate dependent cycling voltammetry. Although this method has been widely employed in the quantitative analysis of pseudocapacitive contribution in many metal oxides and metal dichalcogenides,[41, 43, 44, 142, 143] it has been shown by us that the value obtained from this approach could be physically meaningless in a large potential scope.[48] Herein the peak current was selected as a special example to analyze the pseudocapacitive contribution.

The results of CV are shown in Figure 3.16. The CV curves present combined shapes with obvious redox peaks and capacitive rectangle.[143] The current peaks shift to higher potentials for anode and to lower potentials for cathode with the increasing scanning rate, implying the irreversible electrochemical reaction system. From the analysis of peak current and scanning rate (only 5 at% Nb:TiO_2 data shown in Figure 3.17a), the b value for the anode and cathode process are 0.71 and 0.72, respectively. Following we plot the peak current density divided by the square root of scanning rates against the square root of the scanning rates. The fitting curves are shown in Figure 3.17b. The relationship between $j_{peak} / v^{1/2}$ and $v^{1/2}$ is nearly linear. The analysis indicates the capacitive contributions are 40% and 44% for the anode and cathode process, respectively. The discharge profiles give a similar value (47%), implying the reasonable results. The same approach was applied in other mesoporous Nb:TiO_2 films and the results are shown in Table 3.4.

Table 3.4 The effects of conductivity on the *b* value and pseudocapacitive contribution.

	σ / S/cm	*b* value (cathode)	*b* value (anode)	Pseudocapacitive (cathode)	Pseudocapacitive (anode)
TiO_2	1×10^{-5}	0.63	0.63	25%	21%
2% Nb	7.8×10^{-5}	0.71	0.67	40%	30%
5% Nb	9.8×10^{-5}	0.72	0.71	44%	40%
10% Nb	7.9×10^{-5}	0.70	0.65	37%	27%

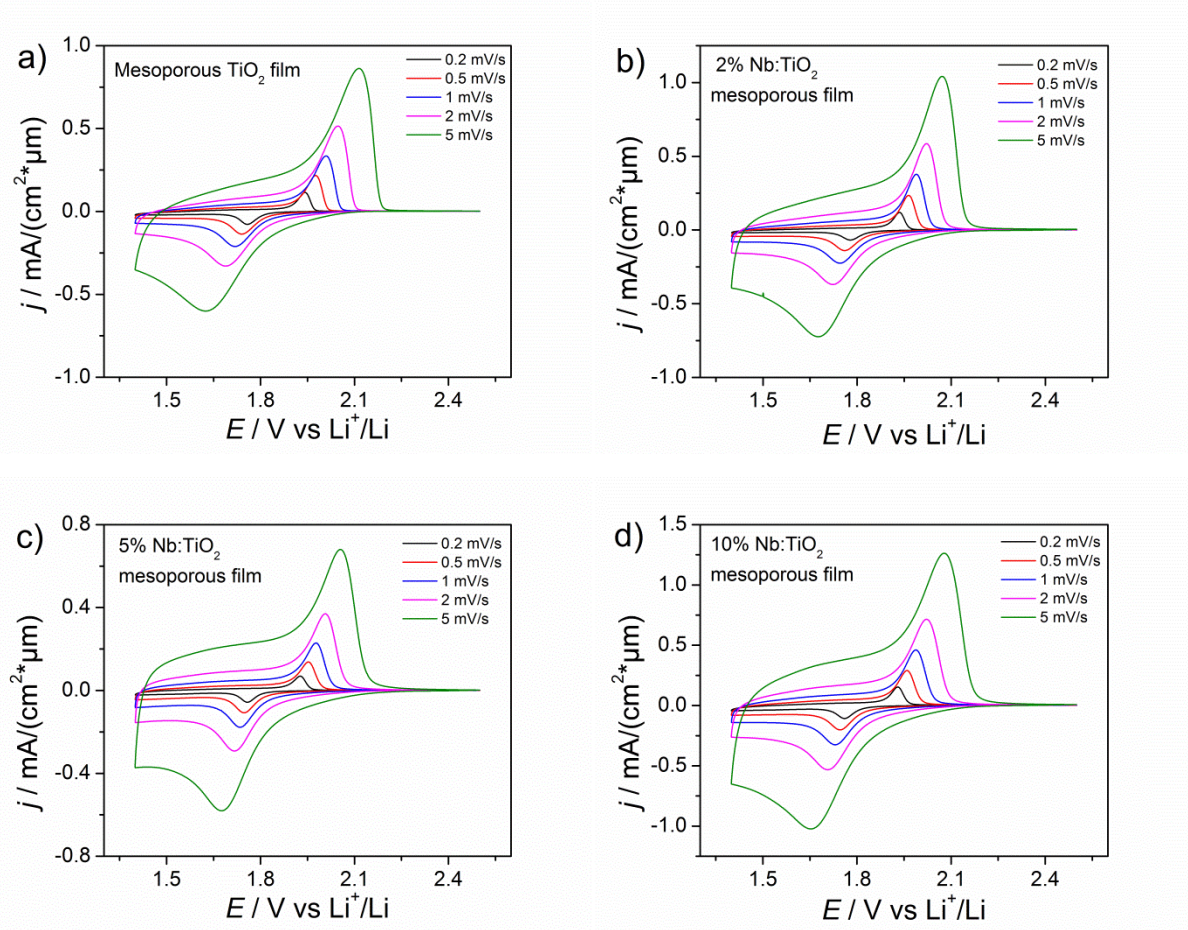

Figure 3.16 CV of Nb:TiO_2 mesoporous films with different scanning rates. (a), (b), (c) and (d) are TiO_2, 2 at%, 5 at% and 10 at% Nb:TiO_2 mesoporous films, respectively.

From Table 3.4, it can be obtained that the pseudocapacitive contribution increases with increasing electrical conductivity. This proves that the pseudocapacitive effect is not only particle size dependent but also the conductivity dependent.

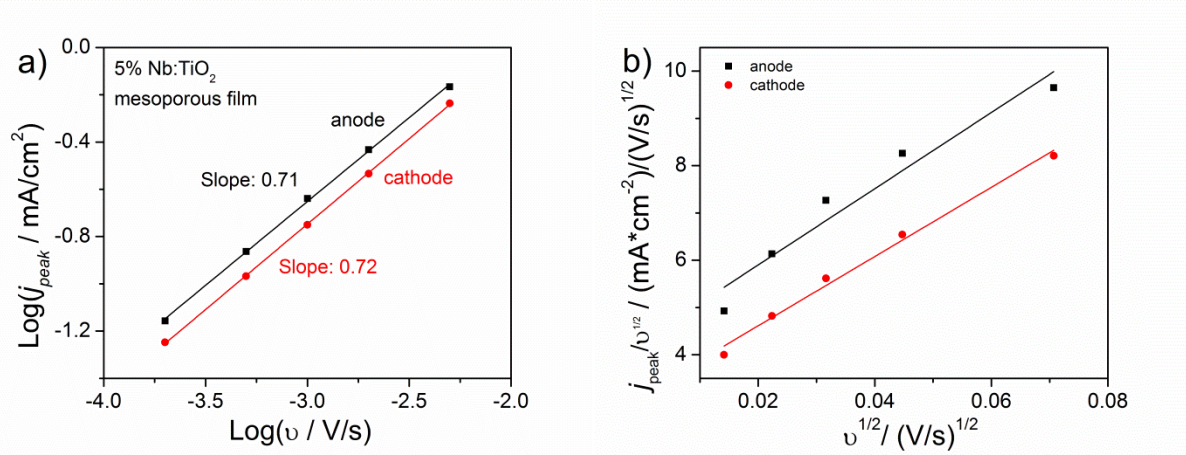

Figure 3.17 The relationships (a) between $\log j_{peak}$ and $\log v$ and (b) between $j_{peak} / v^{1/2}$ and $v^{1/2}$ from the CV data of 5 at% Nb:TiO_2.

3.6 Summary

Nb:TiO_2 with desired Nb contents and controllable crystallite sizes were successfully prepared by a novel two-step non-aqueous reaction. From the results of XRD, Raman spectroscopy and XPS, the Nb^{5+} ions are well incorporated within the anatase lattices, which resulted in Ti^{4+} vacancies and partially reduced titanium at high doping levels. 5 at% Nb:TiO_2 nanocrystals present the best electrochemical performance. The mesoporous Nb:TiO_2 films were prepared based on the assembly of preformed nanocrystals, which possess higher surface areas and wider pore size distributions than the films prepared *via* sol-gel process. The pseudocapacitive contribution in 5 at% Nb:TiO_2 were analyzed by a novel approach. The results show that the capacitive contribution using peak current analysis is around 44 % similar with the estimation from discharge/charge profiles, proving that using the peak current can be a reasonable way to evaluate the pseudocapacitive contribution. Further it is shown that the pseudocapactive contribution is not only crystallite size dependent but also conductivity dependent.

CHAPTER 4
LTO AND DOPED LTO NANOCRYSTALS: PREPARATION, FORMATION MECHANISM, CRYSTALLITE SIZE AND DOPING EFFECTS

4.1 Preparation of LTO nanocrystals

Firstly, a certain amount of metallic lithium were dissolved in benzyl alcohol under argon flow at 70 °C for two to four hours until the solution became clear, homogenous and slightly yellow. Subsequently, stoichiometric amounts of titanium precursors (such as Ti(O-*iso*-Pr)$_4$, Ti(OEt)$_4$ or Ti(OBu)$_4$) were added under vigorous stirring. This solution was kept at 70 °C for another two hours before transferred into a 45 mL Teflon sealed autoclave (from Paar Company). The autoclave was put into an oven with the temperature of 220, 230, 240 and 250 °C for three days. LTO nanocrystals were obtained by centrifugations, washing by acetone for three times and then drying at room temperature. In order to distinguish these nanocrystals obtained from different temperatures, they are named by the reaction temperature, such as LTO-220, LTO-230, LTO-240 and LTO-250.

The as-made nanocrystals were slightly yellow attributed to some organic function groups on their surface. The as-made nanocrystals can be dispersed in water with a concentration of more than 5 wt%. The digital pictures of as-made LTO nanocrystals and its dispersion in water are shown in Figure 4.1. The specific surface area was investigated by N_2 physisorption at 77K and the isotherms are shown in Figure 4.1. The isotherms show typical type-IV shape and exhibit H2-type hysteresis due to the packing of nanocrystals and the BET surface area is 300 m^2/g for LTO-220 and 200 m^2/g for LTO-230, which is corresponding to the particles sizes of less than 10 nm.

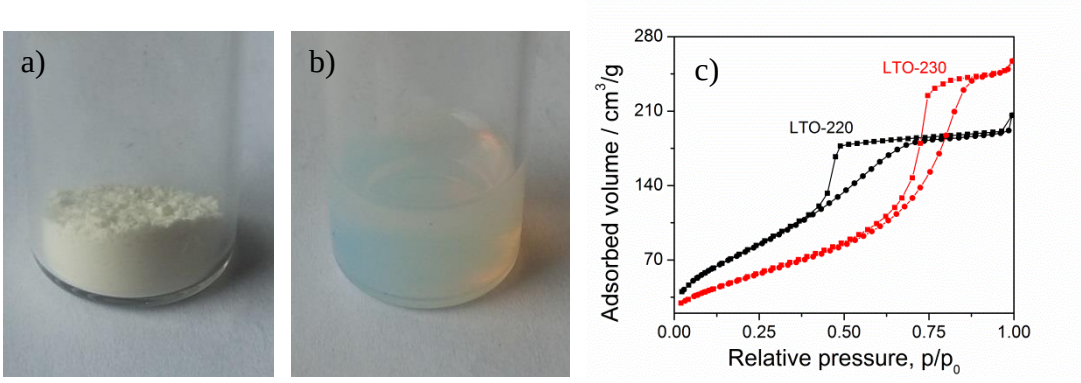

Figure 4.1 Digital pictures of as-made LTO-230 nanocrystals (a) and 5 wt% dispersion of LTO-230 in water (b); (c) N_2 adsorption (circles) and desorption (squares) isotherms at 77 K of LTO-220 (black curves) and LTO-230 (red curves).

4.2 Characterization of LTO nanocrystals

4.2.1 Crystalline structure of LTO nanocrystals

The crystalline structure of LTO nanocrystals was studied by wide-angle X-ray diffraction and Raman spectroscopy. The XRD pattern of as-made LTO-230 nanocrystals is shown in Figure 4.2 and analyzed by the Rietveld refinement using the FULLPROF program. The Rietveld refinement provides an average crystallite size of (6.7 ± 0.6) nm. The R-factors are R_p= 9.77, R_{wp}= 8.80 and R_{exp}= 1.62 and indicate a reasonable fitting.

In order to better understand the formation conditions of LTO nanocrystals, the reaction parameters including reaction temperature, precursors of titanium and concentration of lithium, were investigated in detail. The XRD patterns of LTO nanocrystals obtained under different reaction conditions are all in good agreement with the desired spinel structure with $Fd\bar{3}m$ (O_h^7) space group (JCPDS card 01-082-1617). The reaction temperatures (above 220 °C), the precursors of titanium (alkoxides only), and the concentrations do not alter the crystalline phases. The other lithium salts (lithium acetate, lithium nitrate, and lithium chloride and lithium hydroxide) and other titanium precursors such as titanium tetrachloride, however, cannot be used as precursors for producing pure LTO nanocrystals in this system. The effect of reaction temperature on crystallite sizes was investigated and results are shown in Figure 4.2(b). The results show that the crystallite sizes are around 3.8, 6.0, 5.6 and 6.0 nm with respect to the reaction temperature of 220, 230, 240 and 250°C. The crystallite sizes are calculated using the Scherrer equation based on (111) diffraction peaks. Above 230 °C, the crystallite sizes remain unchanged. LTO-250 nanocrystals aggregate into mesocrystals with a size of several micrometers (seeing Figure 4.7). This phenomena can be found in other oxides prepared based on benzyl alcohol as well, such as ZrO_2, Eu:ZrO_2, HfO_2 etc.[144, 145] The reason behind is recognized that the side products (benzoate etc.) on the surface produced at higher temperature (more than 220 °C, in some cases more than 250 °C) control the growth and stabilize the nanocrystals. The XRD patterns of LTO nanocrystals from different precursors and different concentrations are shown in Appendix Figure 3. Compared the crystallite sizes of LTO nanocrystals from $Ti(OEt)_4$ and $Ti(OBu)_4$ with the one from Ti(O-*iso*-Pr)$_4$, the smaller sizes are attributed to the poorer alkoxide reactivity. The concentration of precursors scarcely alters the crystallite size. The crystallite sizes of LTO nanocrystals from different reaction parameters are shown in Table 4.1.

Table 4.1 Crystallite sizes of LTO nanocrystals from different conditions

Reaction conditions	Temperature / °C				Precursors		Li concentrations	
	220	230	240	250	$Ti(OEt)_4$	$Ti(OBu)_4$	10 mg	40 mg
Crystalite sizes / nm	3.8	6.0	5.6	6.0	4.5	4.5	5.3	5.6

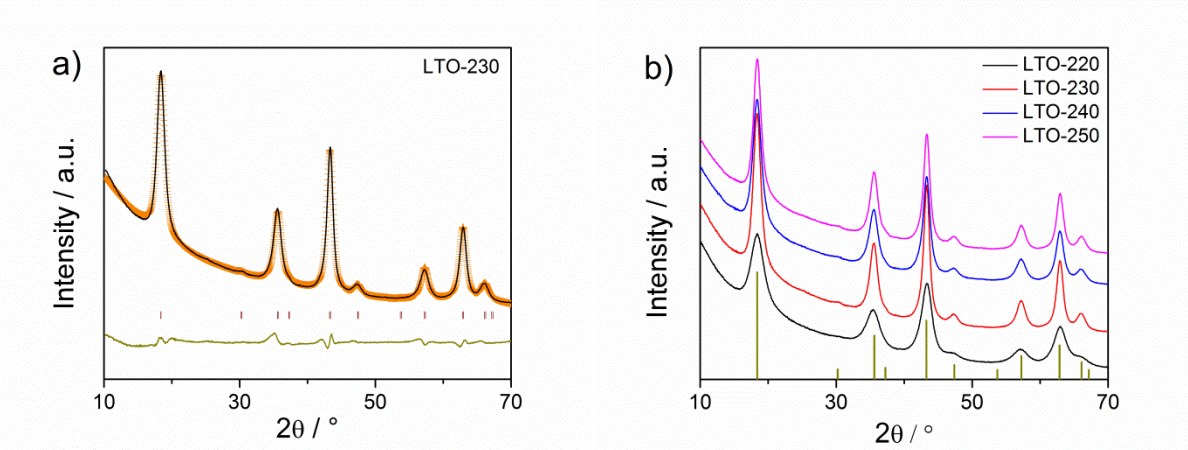

Figure 4.2 XRD patterns of LTO nanocrystals. (a) Black curve is the collected XRD pattern of LTO nanocrystals obtained at 230 °C from Ti(O-*iso*-Pr)$_4$ with 20 mg metallic lithium, orange curve represents the fitting result from Rietveld refinement and dark yellow curve for the difference. (b) XRD patterns of LTO nanocrystals from different temperatures.

Raman spectra of as-made LTO-220 and LTO-230 were collected and are shown in Figure 4.3(a). Five first-order Raman-modes given by $1\times A_{1g}$, $1\times E_g$ and $3\times F_{2g}$ modes of cubic LTO spinel structure according to factor group analysis can be observed.[146, 147] These five vibration bands located at wavenumbers of 231, 270, 337, 427 and 677 cm^{-1} can be assigned to F_{2g}, F_{2g}, F_{2g}, E_g and A_{1g}, respectively, which are in fair agreement with literature.[148-150] In detail, a strong band at 678 cm^{-1} with the shoulder at 754 cm^{-1} is attributed to the symmetrical stretching vibration Ti-O in the TiO_6 octahedron; the band located at 427 cm^{-1} corresponds to an asymmetrical stretching vibration Li-O in the LiO_4 tetrahedron; the band located 231 cm^{-1} is assigned to the bending vibration Ti-O in the TiO_6 octahedron.[146, 148, 151] Raman bands of impurities such as monoclinic Li_2TiO_3 (lithium titanate), cubic $LiTi_2O_4$ (spinel-type) and TiO_2 (rutile), especially anatase TiO_2 are not found. Another noticeable Raman band at 618 cm^{-1} is attributed to phenyl rings from residual benzoate on the surface, which is commonly observed in metal oxides obtained at high temperature reaction in benzyl alcohol system.[144]

Apart from the crystalline structure, the optical properties of the LTO-230 were investigated by UV-vis absorption spectra at room temperature. The analysis method was already

introduced in chapter 3. The result in Figure 4.3(b) indicates an indirect band gap of $E_{bandgap}$ = (3.69 ± 0.05) eV. The optical bandgap of LTO-230 is in accordance with other experimental observations in the literature.[25, 89, 152, 153]

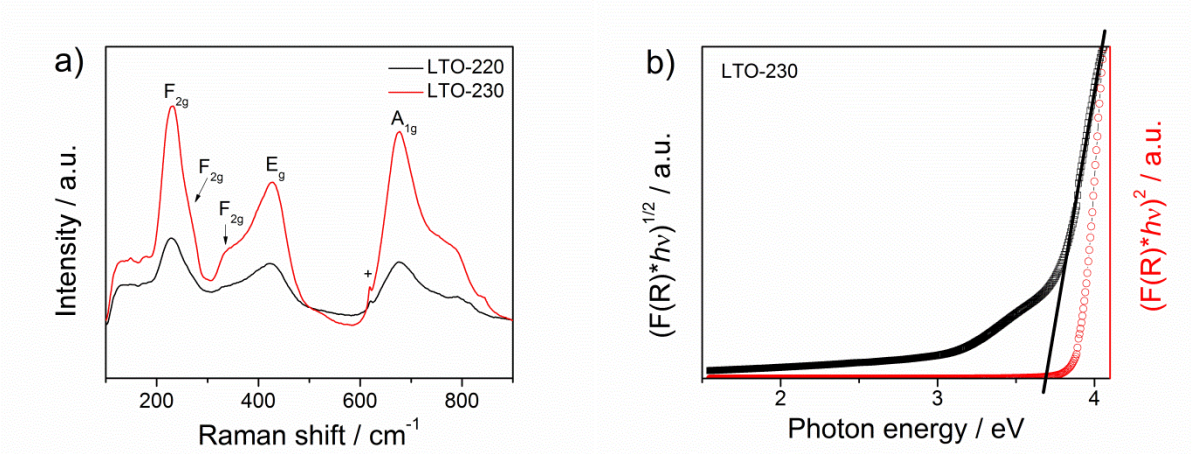

Figure 4.3 (a) Raman spectra of as-made LTO-220 and LTO-230 nanocrystals. "+" located at 618 cm^{-1} represents the vibration band from phenyl ring. (b) Direct (squares) and indirect (circles) optical transitions in LTO-230 nanocrystals.

4.2.2 Surface components of LTO nanocrystals

The surface components on LTO nanocrystals are of great importance for explaining the growth process and physical properties, and are investigated by several state-of-the-art characterization methods such as XPS, TG-MS and FTIR.

The XPS survey of LTO nanocrystals and detailed scans of Ti 2p, O 1s and C 1s core level are presented in Figure 4.4. The XPS survey spectra indicate that no other element is found except from Li, Ti, O and C in both LTO nanocrystals. Carbon can be commonly observed in samples due to adventitious carbon source and can be used to adjust the charging effect by centering the C−H/C−C peak to 284.8 eV. The atomic ratio of lithium and titanium (Li/Ti) is 0.82, which is identical with the product—$Li_4Ti_5O_{12}$. Both LTO nanocrystals present the same Ti 2p core level spectra shown in the Figure 4.4(b). A doublet peak at 464.4 eV and 458.5 eV with the area ratio of 0.5 is attributed to the $2p_{1/2}$ and $2p_{3/2}$ from spin-orbit splitting of Ti 2p, which is in fair agreement with Ti^{4+} in spinel LTO.[154-156] No reduced titanium is found. The XPS spectra of C 1s core level are shown in Figure 4.4 (c) and can be deconvoluted into five signals at 284.8, 285.8, 288.8, 290.0 and 291.5 eV, thereby indicating the presence of various forms of carbon with different bonding configurations. The peak at the lowest binding energy with the greatest quantity is attributed to C−H/C−C carbon from adventitious hydrocarbon and residual organic groups on the surface. The binding energy at 285.8 eV is assigned to C−O−C from unreacted precursors and the binding energy at 288.8 eV is originated from C in

O−C=O bonds in benzoate, which can be confirmed by FTIR data.[157-159] From the quantitative analysis of C−O−C and O−C=O on the surface, the unreacted precursor's content in LTO-220 is much higher than in LTO-230 while the benzoate content in LTO-220 is much lower than in LTO-230. This is one evidence that the benzoate can be easily produced at higher temperature.[145] The peak located at 290.0 eV is assigned to carbonate, which is normally seen in spinel LTO.[160, 161] The content of carbonate in LTO-220 is much higher than LTO-230. The weak peak with highest energy of 291.5 eV is related to the Teflon lining of the reaction container. For O 1s core level spectra, two peaks can be fitted: one from inorganic species mainly LTO located at 529.9 eV and the other one from organic species located at 531.3 eV.

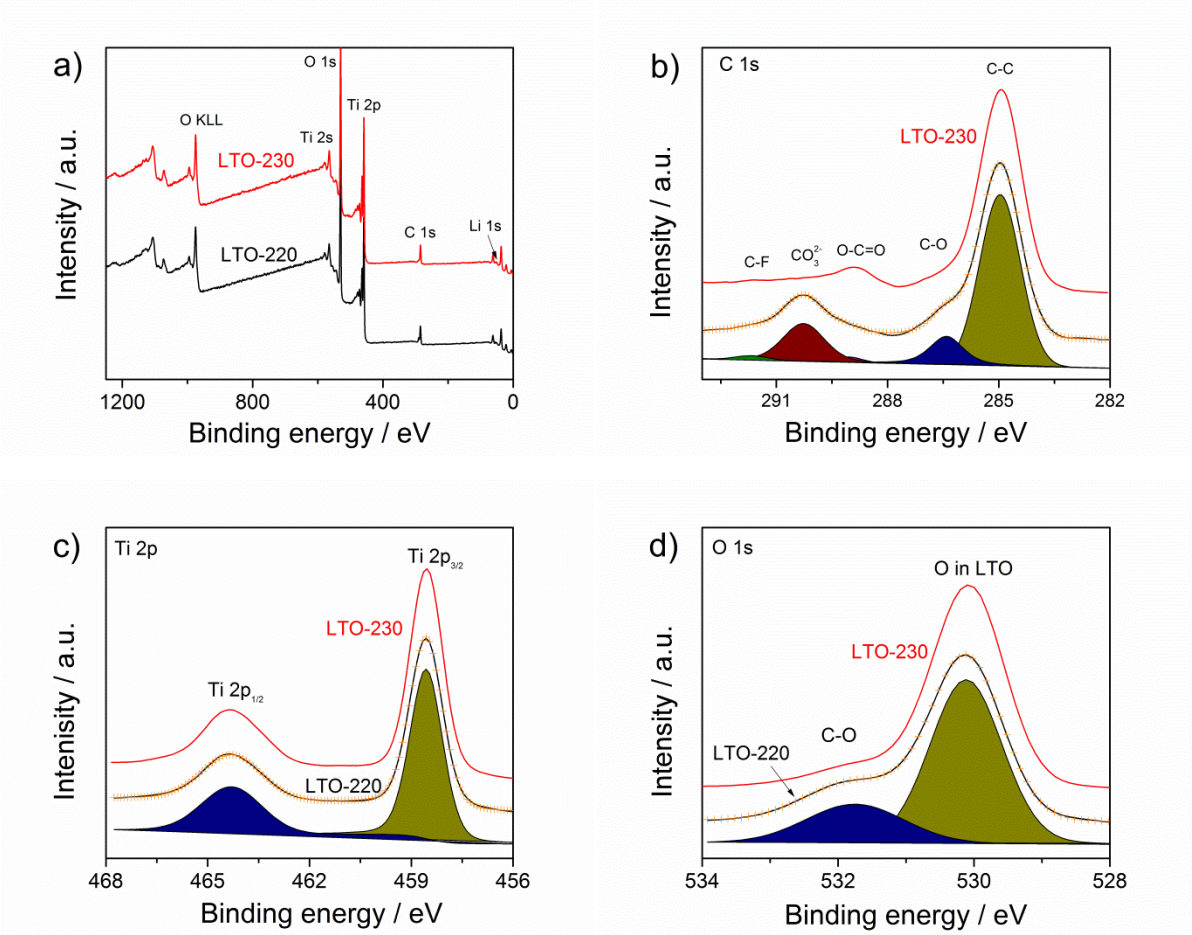

Figure 4.4 XPS survey of LTO nanocrystals. (a) Full spectra of LTO-220 (black) and LTO-230 (red). (b), (c) and (d) are detailed spectra of Ti 2p, C 1s and O 1s core level respectively. The upper red curves are from LTO-230 nanocrystals and their fitting curves are not shown. The black curves represent the experimental data of LTO-220 and the orange crosses represent the sum of the peak fits using mixed Gaussian−Lorentzian functions.

Although the different organic species can be distinguished by XPS spectra, it is hard to identify the organic compounds only from the analysis of XPS. Therefore combined methods (TG-MS and FTIR) are needed to determine them. The thermal gravimetric analysis can provide the exact content of organic matter and the organic compound fragment information

with the assistance of an accompanying mass spectroscopy, whereas the FTIR can provide some fingerprint information of the organic compounds.

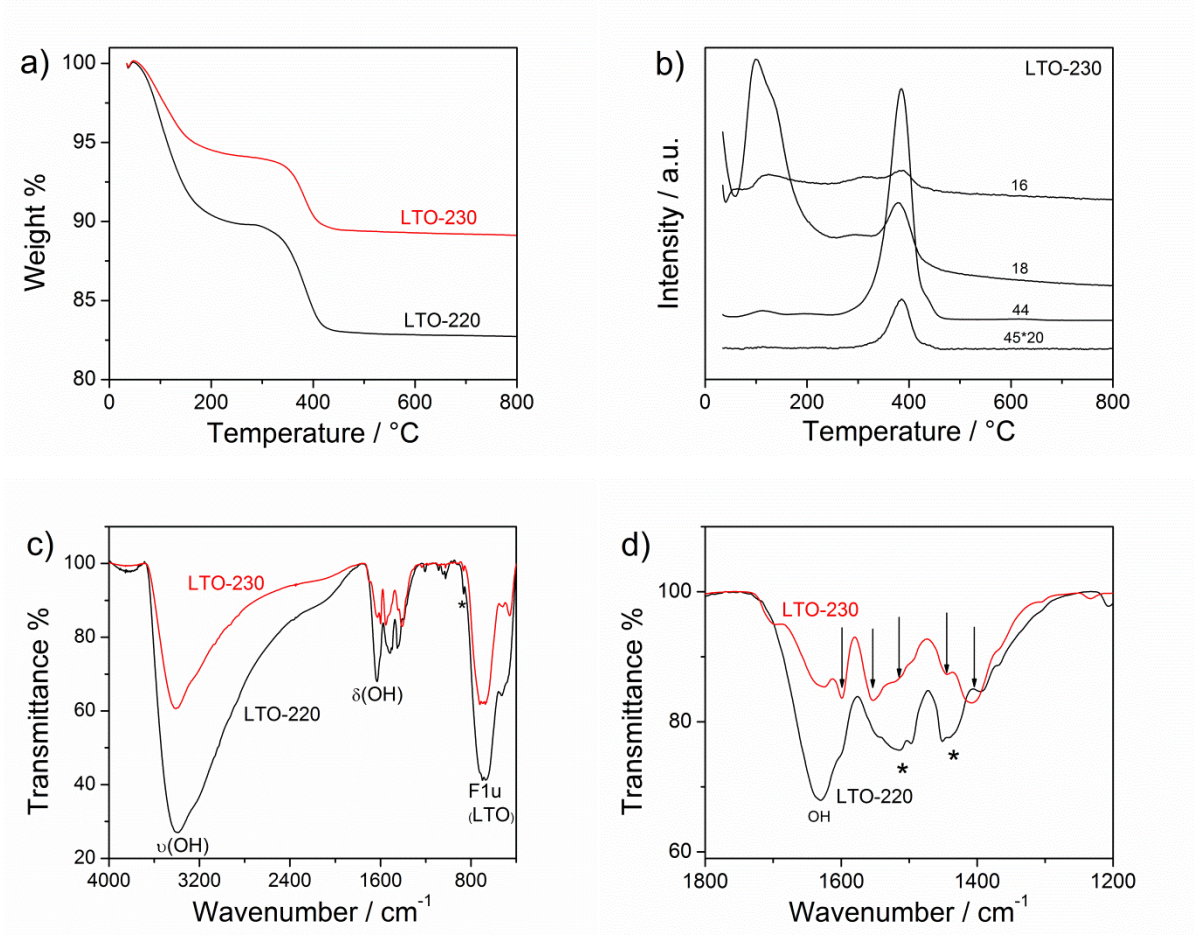

Figure 4.5 (a) Thermal gravimetric analysis of LTO-220 and LTO-230 nanocrystals and (b) the intensity of mass species of 16, 18, 44 and 45 with temperature in LTO-230 nanocrystals. (c) KBr-pellet FTIR spectra of both LTO-220 and LTO-230 nanocystals and zoom in spectra in the wavenumber of 1200 to 1800 cm^{-1} (d). The red curve represents LTO-230 and the black curve stands for LTO-220. The arrows and the asterisks mark the vibration bands from benzoate and carbonate respectively.

The results from thermal gravimetric analysis combined with mass spectra and FTIR spectra are shown in Figure 4.5. Both LTO nanocrystals exhibit similar weight loss behaviors, including adsorbed water evaporation below 200 °C (6 wt% for LTO-230 and 10 wt% for LTO-220) and residual organic compounds combustion (4 wt% for LTO-230 and 8 wt% for LTO-220) between 320 to 420 °C. The accompanying MS data can be a supporting tool for confirming the organic groups like benzoate or isopropoxide on the surface: water (m/e = 18), carbon dioxide / ethylene oxide / acetaldehyde etc. (m/e = 44), $C_2H_5O^+$ / CHO_2^+ (m/e = 45) and CH_4^+ / O^+ (m/e = 16).

The FTIR spectra were recorded in the spectral range from 4000 to 400 cm^{-1} using a KBr pellet method. Not surprisingly, two intense bands are centered at 3400 cm^{-1} (OH stretching

vibration; ν_{OH}) and 1630 cm^{-1} (OH bending vibration; δ_{OH}) from adsorbed water. The strong band at ~682 cm^{-1} is attributed to the IR-active F_{1u} vibrational mode of the LTO spinel lattice.[147] Spectra range from 1800 to 1200 cm^{-1} can give fingerprint information about carbonate and benzoate. One group of vibration bands (1513, 1435 and 868 cm^{-1}) represents the OCO_2 asymmetrical stretching vibrations (ν_3) and bending vibration (ν_2) of lithium carbonate.[162] As shown in XPS, there is more carbonate and less benzoate in LTO-220 than LTO-230, consequently the carbonate vibration bands are much stronger in LTO-220 than LTO-230. In the FTIR of LTO-230, the vibration bands (1598, 1497 and 1450 cm^{-1}) are characteristic of the skeletal vibrations of the aromatic ring and the vibration bands (1552 and 1408 cm^{-1}) are associated to asymmetrical and symmetrical stretching vibrations ($-COO^-$), denoting that benzoate species are adsorbed.[163-165] The coordination mode of the $-COO^-$ group linked to the LTO surface can be assessed by the difference of frequency between the two carboxylate stretching vibrations ($\Delta = \upsilon_{as} - \upsilon_s$) accounts to Δ = 144 cm^{-1}, indicating a bridging bidentate coordinated benzoate species.[162]

Combining the data from XPS, TG-MS and FTIR, we can deduce that benzoate and *iso*-propoxide etc. species are located on the surface of LTO nanocrystals. The benzoate on the surface provides an attracted force between nanocrystals by π-π conjugate valence to form some crystals aggregates or clusters, as found in literature.[166] When the temperature is as high as 250 °C, LTO aggregates with size of several micrometers can be found from SEM. On the other side, the residual alkoxide on the surface can further hydrolyze to make nanocrystals with negative charges. The electrostatic repelling force between nanocrystals makes them dispersible in water. As shown in XPS and FTIR, the higher temperature induces more benzoate and less alkoxide, resulting in a poor dispersibility. In order to avoid the impact of organic compounds on the surface of nanocrystals on their electrochemical performance, the samples were treated at 400 °C for one hour to remove organic compounds.

4.2.3 Morphology of LTO nanocrystals

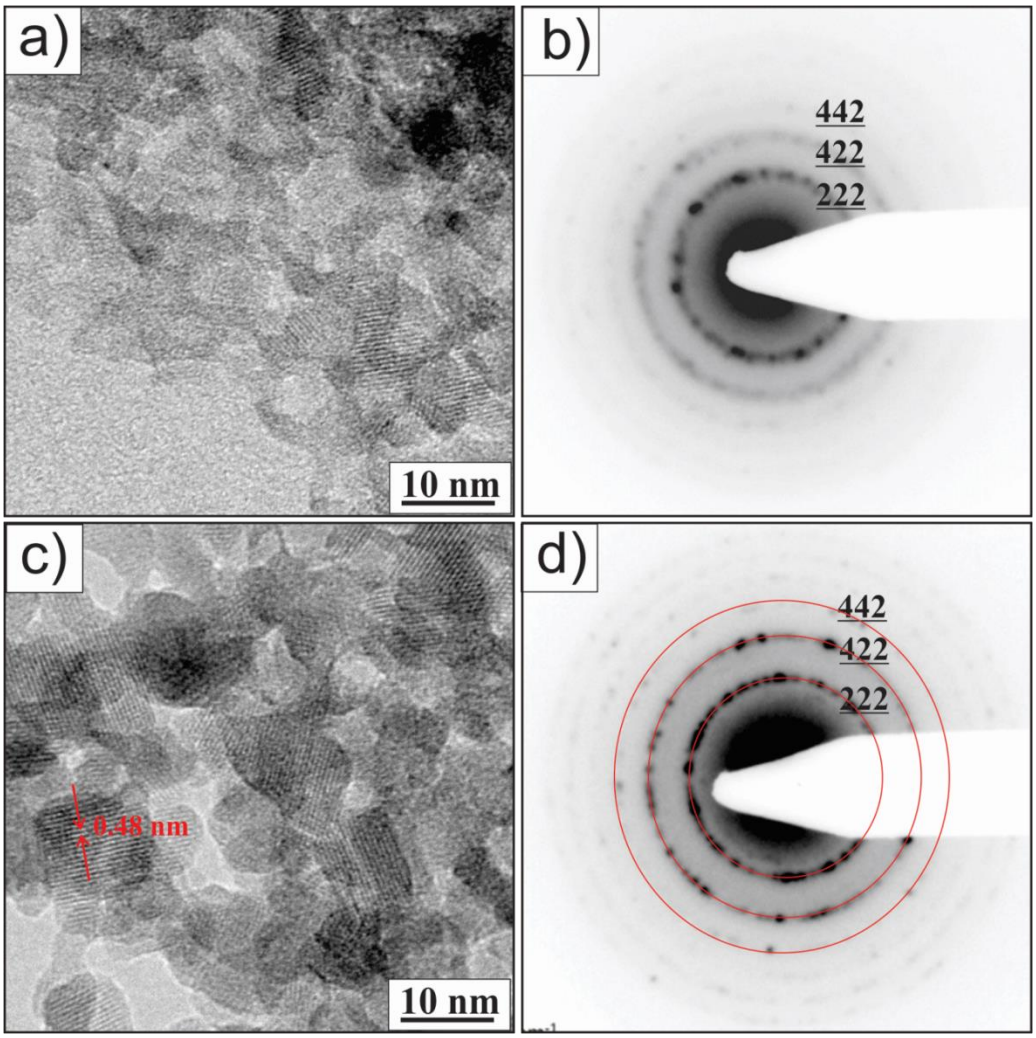

Figure 4.6 HRTEM images and SAED (selected area electron diffraction). (a) and (b) for LTO-220. (c) and (d) for LTO-230.

The representative HRTEM images of LTO nanocrystals are shown in Figure 4.6. The results indicate that the nanocrystals are spherical and the average particle size increases from around 4 nm to 7 nm with the increase of temperature. Good crystallinity of the LTO nanocrystals can be achieved by increasing reaction temperature to 230 °C and a well-defined crystalline structure with a lattice spacing of 0.48 nm is corresponding to the distance between the (111) planes of LTO spinel (Figure 4.6 c). The three diffraction rings could be assigned to the crystalline facet (222), (422) and (442) of spinel LTO according to JCPDS card 00-049-0207, proving that these ultra-small nanocrystals are highly crystalline.

As mentioned above, when reaction temperature is high enough, LTO nanocrystals will aggregate to mesocrystals. The SEM images of LTO-250 shown in Figure 4.7 perfectly prove the proposal. The several micrometer LTO spheres can be observed at low magnification SEM images and the microspheres are composed of numerous nanocrystals seeing Figure 4.7c.

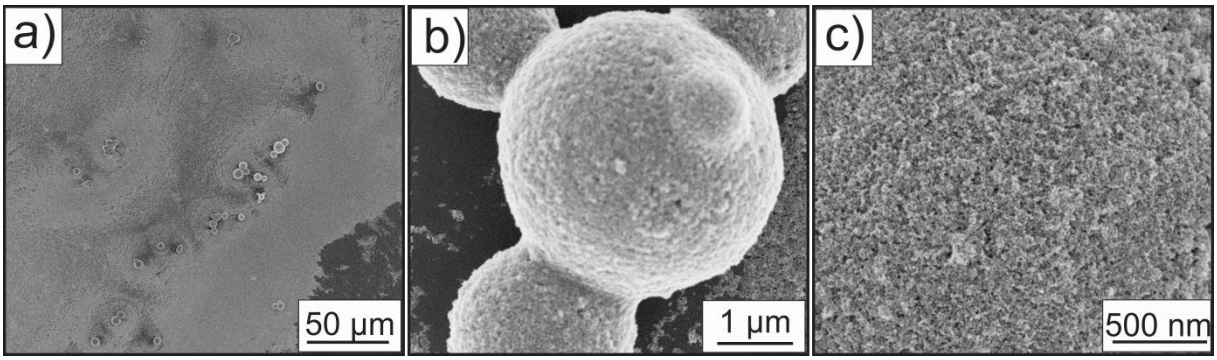

Figure 4.7 SEM images of LTO-250 nanocrystals with different magnifications.

4.2.4 Formation mechanism of LTO nanocrystals

The formation mechanism of M-O-M in non-aqueous routes relies on the condensation reaction between the oxygen donor and the metal precursor. Dependent on the eliminated molecular, five distinct pathways for the M-O-M formation are alkyl halide elimination, ether elimination, condensation of carboxylate group, C-C coupling of benzylic alcohols and alkoxide molecules and aldol/ketamine condensation.[62, 63, 134, 167] In order to investigate the potential formation mechanism of LTO, the liquid reaction products from Ti(O-*iso*-Pr)$_4$, Ti(OEt)$_4$ and Ti(OBu)$_4$ were collected and analyzed by gas chromatography mass spectrometry (GC-MS). The results are shown in Figure 4.8 and Appendix Figure 4. From the GC-MS data, the main products based on the precursors of Ti(OEt)$_4$ and Ti(OBu)$_4$ are toluene and benzaldehyde. The formation mechanism for LTO formation from these two precursors can be following: firstly metallic lithium reacts with benzyl alcohol to form lithium benzyl alkoxide (step 1); after adding Ti(OEt)$_4$ and Ti(OBu)$_4$, the alcohol exchange reaction can happen to some extent (step 2); the main reaction is similar with Meerwein-Ponndorf-Verley reduction to form toluene, benzaldehyde and titanium hydrate, which is following condensation reaction with titanium alkoxide or lithium benzyl alkoxide to form Ti−O−Ti or Ti−O−Li (step 3 and step 4).[168] However the reaction based on Ti(O-*iso*-Pr)$_4$ is much more complicated than those based on Ti(OEt)$_4$ and Ti(OBu)$_4$. Except from toluene and benzaldehyde, three more products (benzyl ether, 4-phenyl-2-butanol and 1,5-diphenyl-3-pentanol) are found. For the reaction from Ti(O-*iso*-Pr)$_4$, two side reactions were proposed: one is ester elimination reaction, which is normally seen in the preparation of HfO_2 nanocrystals in benzyl alcohol; the other one is C−C cleavage reaction, which is normally seen in the preparation of $BaTiO_3$ nanocrystals.[169, 170] The small amounts of 1,5-diphenyl-3-pentanol in the reaction mixture are derived from the reaction between 4-phenyl-2-butanol and Ti(O-*iso*-Pr)$_4$ in an analogous side reaction 1. The produced benzaldehyde can further react with alkoxide to form benzoate, seeing step 5. This process explained the formation of

benzoate on the surface and the much higher account of toluene than benzaldehyde. In the preparation of yttria and zirconia at high temperature, this process can be observed as well.[165, 171, 172]

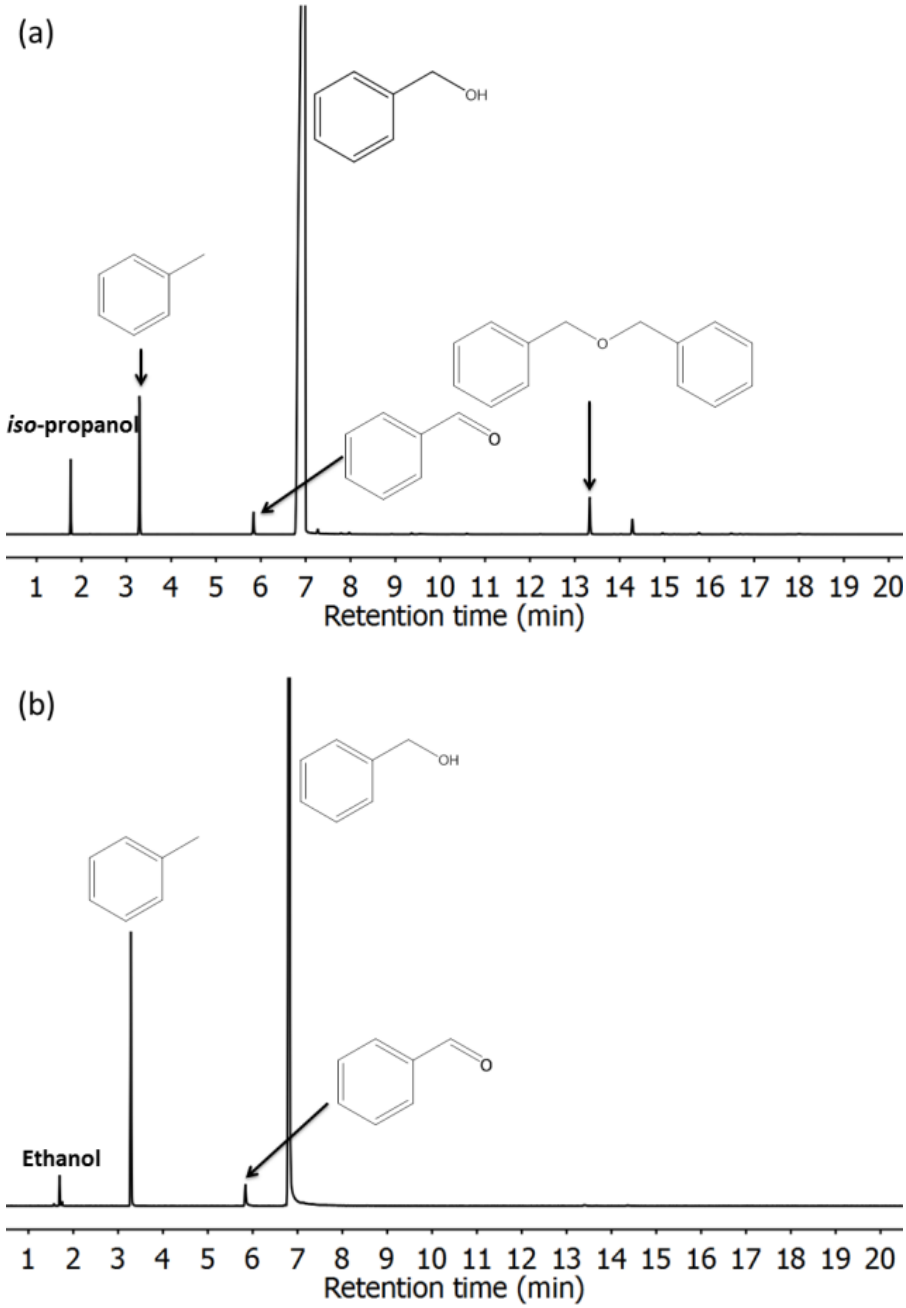

Figure 4.8 The gas chromatography mass spectra of liquid reaction products. (a) for Ti(O-*iso*-Pr)$_4$ aand (b) for Ti(OEt)$_4$. The peaks are assigned to different compounds marked in molecular structure according to the recorded MS data.

Step 1

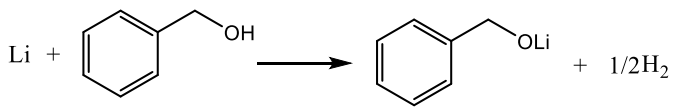

Step 2

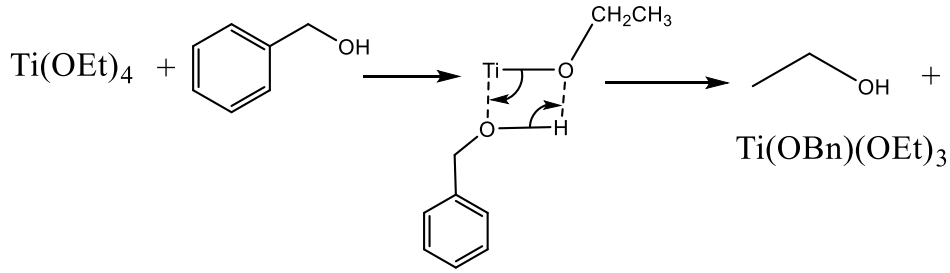

Step 3

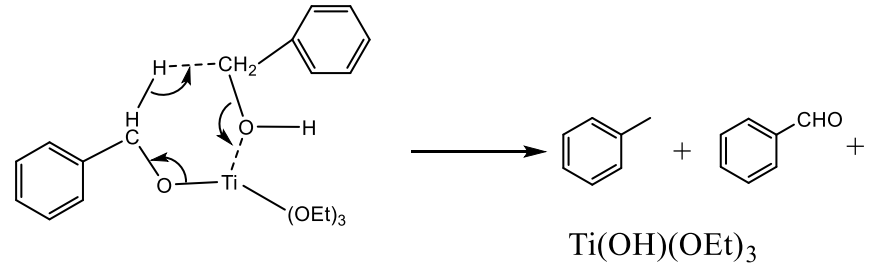

Step 3 Side reaction 1

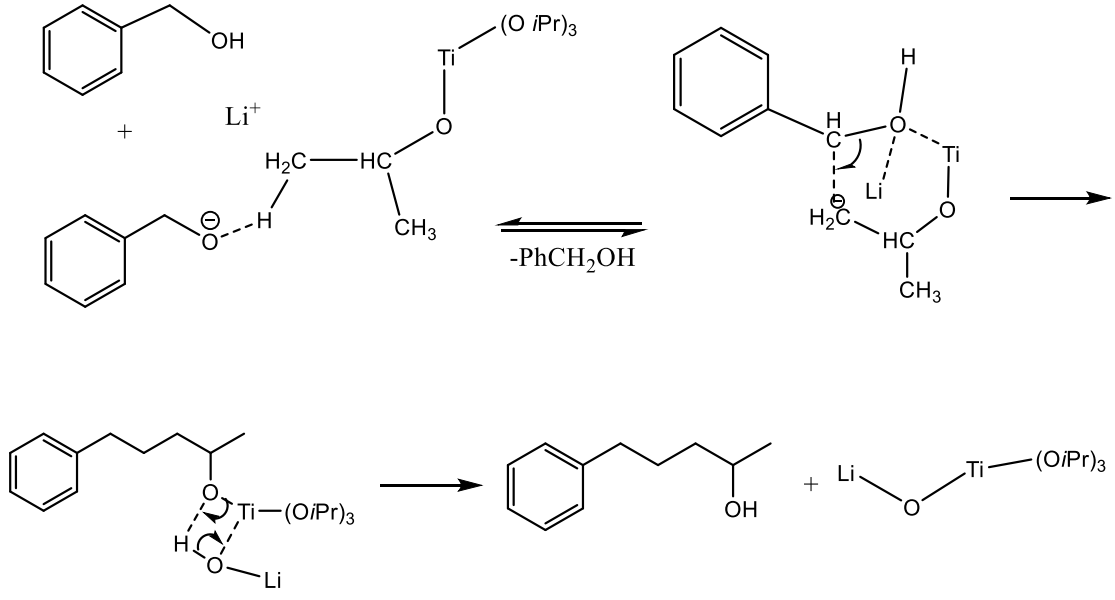

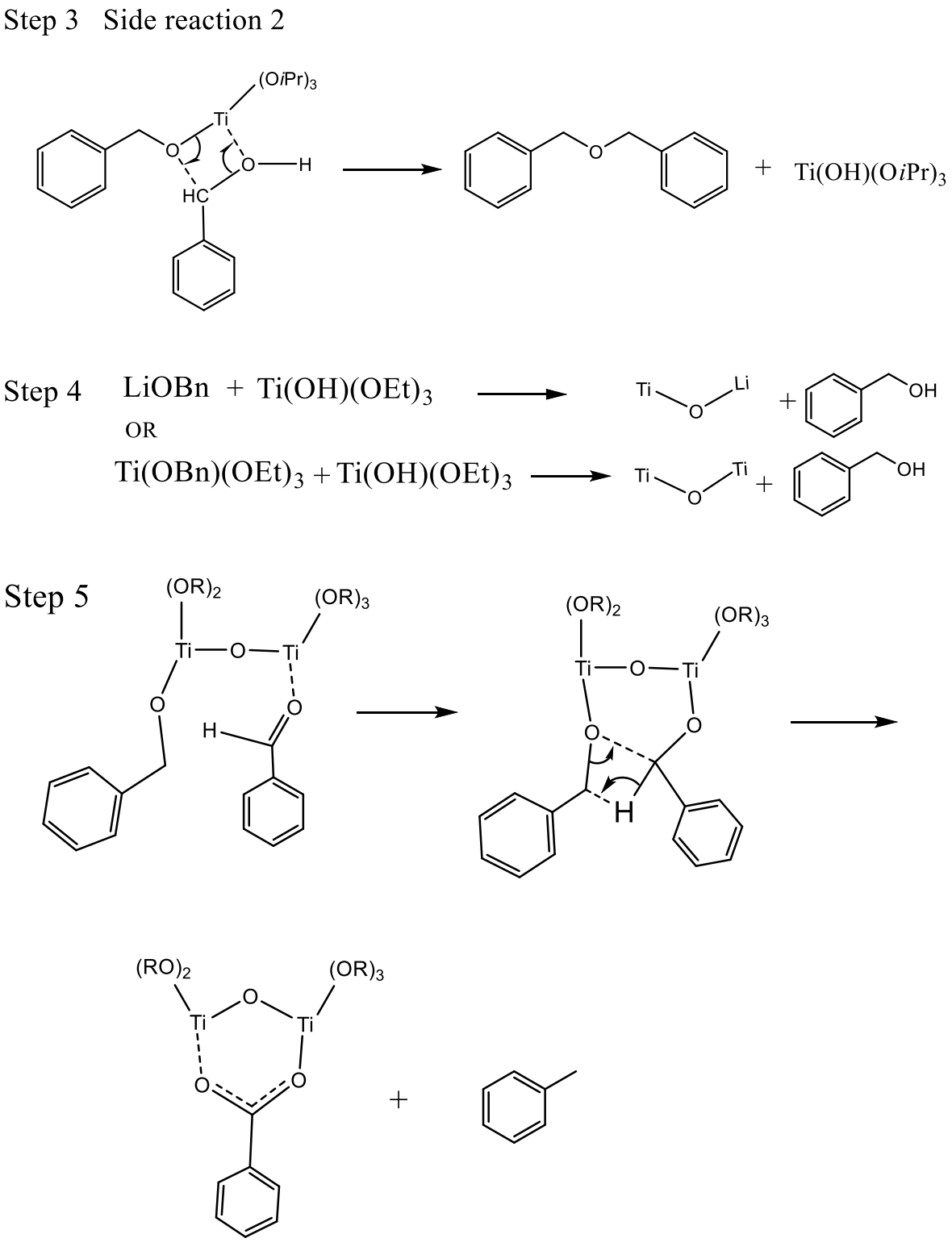

Figure 4.9 The proposed reaction mechanism for the formation of LTO nanocrystals from Ti(O-*iso*-Pr)$_4$, Ti(OEt)$_4$ and Ti(OBu)$_4$.

4.2.5 Crystallite size effect on electrochemical performance

LTO-220 (3.8 nm) and LTO-230 (6.0 nm) were selected to investigate the crystallite size effects on the electrochemical performance. The working electrodes for LTO-220 and LTO-230 were prepared in this way: 12 mg LTO nanoparticles were dispersed into 2 mL water and 0.05 mL of such dispersion was spread on an ITO substrate, and then the electrode was dried at 120 °C for 1 h. All the electrochemistry tests were carried out in traditional three-electrode system with Li metal as reference and counter electrode. All of the potentials in this thesis are referred to Li^+/Li couple. The electrolytes were 1 mol/L lithium perchlorate in propylene carbonate.

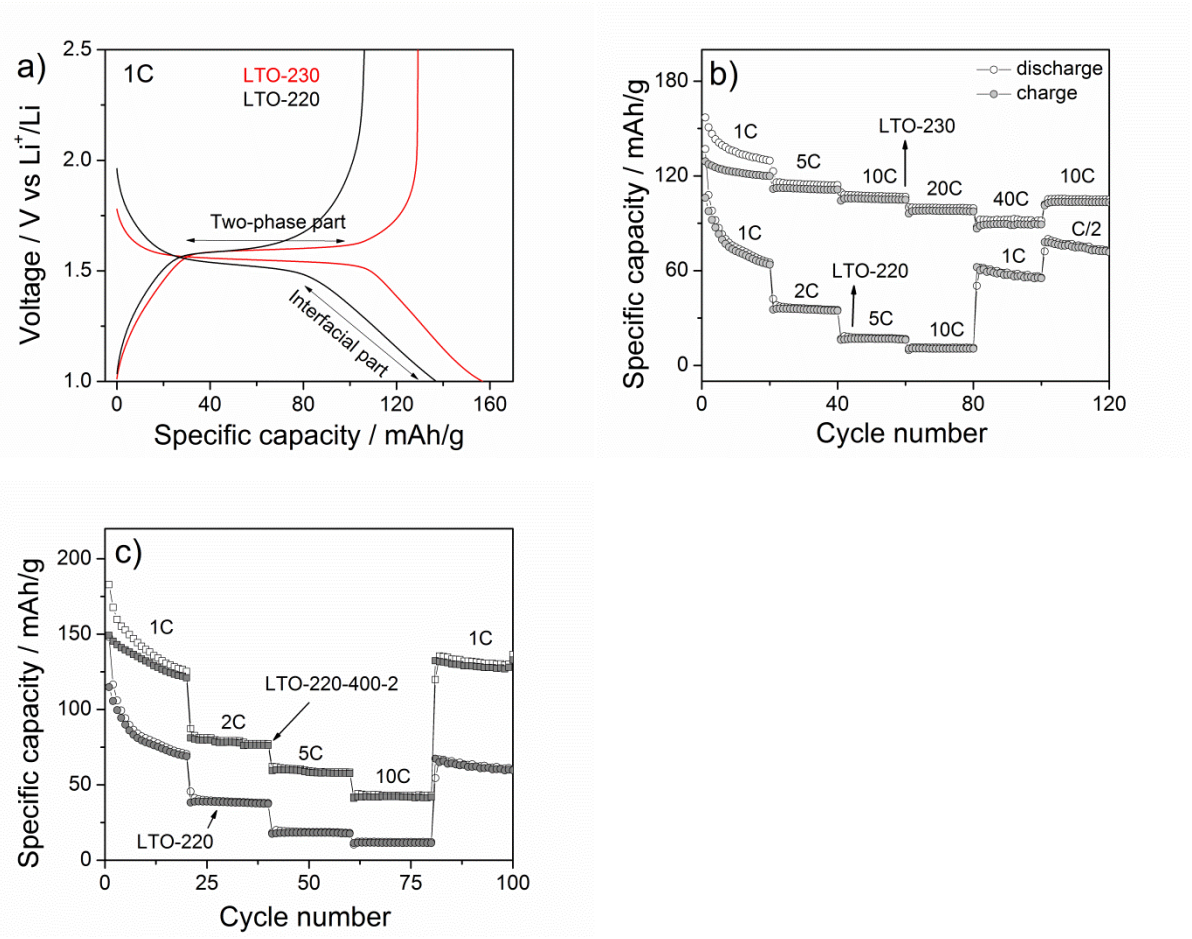

Figure 4.10 (a) Galvanostatic discharge/charge profiles of LTO. Black curve and red curve are for LTO-220 and LTO-230 at 1C, respectively. (b) Rate capacity of LTO-220 and LTO-230. (c) Rate capacity of LTO-220 and LTO-220 annealed at 400 °C for 2 h.

Galvanostatic charge/discharge curves of LTO nanocrystals with different crystallite sizes are presented in Figure 4.10a. The profiles exhibit a distinct intercalation and de-intercalation plateau at 1.55 and 1.60 V, respectively. These plateaus are characteristic of the topotactic transformation of LTO to rock salt-type $Li_7Ti_5O_{12}$ (two phase equilibrium part) and vice versa. The slopes before and after the plateau were recognized as the interfacial charge storage

(Interfacial part).[173] Both nanocrystals present smaller specific capacity than theoretical one (175 mA/g), which can be caused by the organic function group on the surface. The electrochemical performance of LTO-220 and LTO-220-400-2 are shown in Figure 4.10c. After annealed at 400 °C for 2 hours, the specific capacity and rate capacity both get enhanced. It has been shown that the surface organic functions can hinder the Li^+ ions and electron transport at the interface.[60] LTO-220 shows shorter two phase part and longer interfacial part than LTO-230, which is attributed to the smaller crystallite size of LTO-220. After 20 cycles at 1C, the specific capacity of LTO-220 dramatically drops from 150 to 60 mA/g. This can be assigned to the fierce interface restructuring induced by huge interfacial charge storage. As proven by Wagemaker et. al, the profound interfacial charge storage will strongly restructure the surface and consequently generates large irreversible capacity loss.[26] LTO-230 nanocrystals present excellent rate capacity (90 mA/g at 40C), which is derived from small crystallite size (6 nm), small interfacial charge storage and high crystallinity.

4.3 Nb^{5+} and Al^{3+}-doped LTO nanocrystals

4.3.1 Preparation of doped LTO nanocrystals

The preparation of doped LTO nanocrystals is based on the same protocol with the one of LTO nanocrystals, and the only difference is that 5 at% of titanium precursors were substituted by doped element precursors. For instance, 20 mg lithium are added into 25 mL benzyl alcohol at 70 °C for 2 hours and then stoichiometric $Ti(O\text{-}iso\text{-}Pr)_4$ and $Nb(OEt)_5$ or $Al(O\text{-}iso\text{-}Pr)_3$ are introduced. After stirring one hour, the homogeneous reaction solution was transferred into 45 mL autoclave, and the reaction happens at 230 °C for three days. After cooling down, the samples were collected and washed by acetone for three times and then dried at room temperature.

To avoid the effects of the organic compounds on their surface on electrochemical performance, the nanocrystals were treated at 400 °C for one hour. From TGA, the organic compounds can be totally removed at 400 °C. The TGA-DTA data are shown in Figure 4.13. After 400 °C heat treatment for one hour, the crystallite size of doped LTO nanocrystals remains unchanged (seeing XRD patterns in Appendix Figure 6a). Without specific explanation, the nanocrystals characterized and applied in electrochemistry are the ones treated at 400 °C for 1 hour. The surface area is determined by N_2 physisorption measurements and the results are shown in Appendix Figure 5. The BET surface area for Al:LTO and Nb:LTO are 334 and 239 m^2/g respectively. The morphology of doped LTO

nanocrystals were characterized by high resolution TEM and the images are shown in Figure 4.11. The doped LTO nanocrystals are spherical and the average particle sizes are 4 nm for Al:LTO and 6 nm for Nb:LTO respectively. In comparison with LTO nanocrystals size shown above, the particle sizes get smaller after doping. The crystalline lattices can be clearly observed in Nb:LTO and Al:LTO nanocrystals, which confirmed that the obtained materials are highly crystalline.

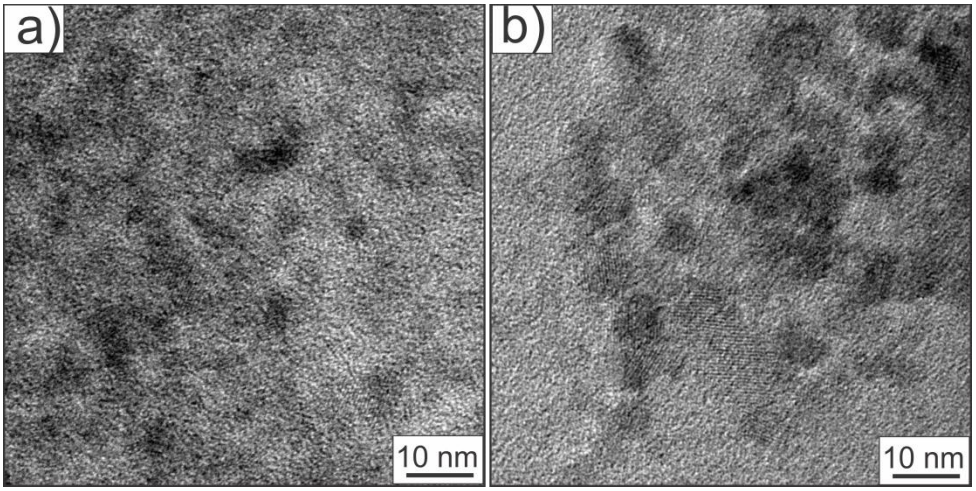

Figure 4.11 TEM images of Al:LTO (a) and Nb:LTO (b) nanocrystals.

4.3.2 Microstructure of doped LTO nanocrystals

In order to probe the microstructure of doped LTO nanocrystals, XRD with the Rietveld refinement and Raman spectroscopy were carried out. The XRD patterns of Nb and Al:LTO are shown in Figure 4.12. The XRD patterns are identical with characteristic spinel structure according to JCPDS card 00-049-0207, confirming that the doped LTO nanocrystals present spinel structure without any impurity phases such as TiO_2, Al_2O_3 and Nb_2O_5. The patterns are analyzed by the Rietveld refinement as well and the results shown in Figure 3.12 (b) and (c). The obtained crystalline parameters are shown in table 4.2. The R_{wp} values are 7.25, 7.02 and 5.96 for pure LTO, Nb:LTO and Al:LTO respectively, indicating the good refinements. Compared with pure LTO, the lattice parameters increase from 8.3557 to 8.3593 Å for Nb: LTO, and decrease to 8.3240 Å for Al:LTO. This can be assigned to the substitution of Ti^{4+} (74.5 pm) with larger Nb^{5+} (78 pm) and smaller Al^{3+} (67 pm) according to the Vegard's law. The crystallite sizes for Nb:LTO and Al:LTO are 5.2 ± 0.9 nm and 3.2 ± 0.6 nm, which are consistent with observation from TEM. In comparison with pure LTO nanocrystals, the crystallite size of Al:LTO significantly decreases, which is attributed to the suppression of particle crystallization due to high level doping.[66, 174] From the analysis of XRD patterns, it can be stated that Nb or Al are well incorporated with LTO. In order to obtain similar

crystallite size, the Al:LTO nanocrystals were treated at 600 for 2 hours (Al:LTO-600). The crystallite size of Al:LTO-600 are 7.6 nm. The XRD pattern is shown in Appendix Figure 5.

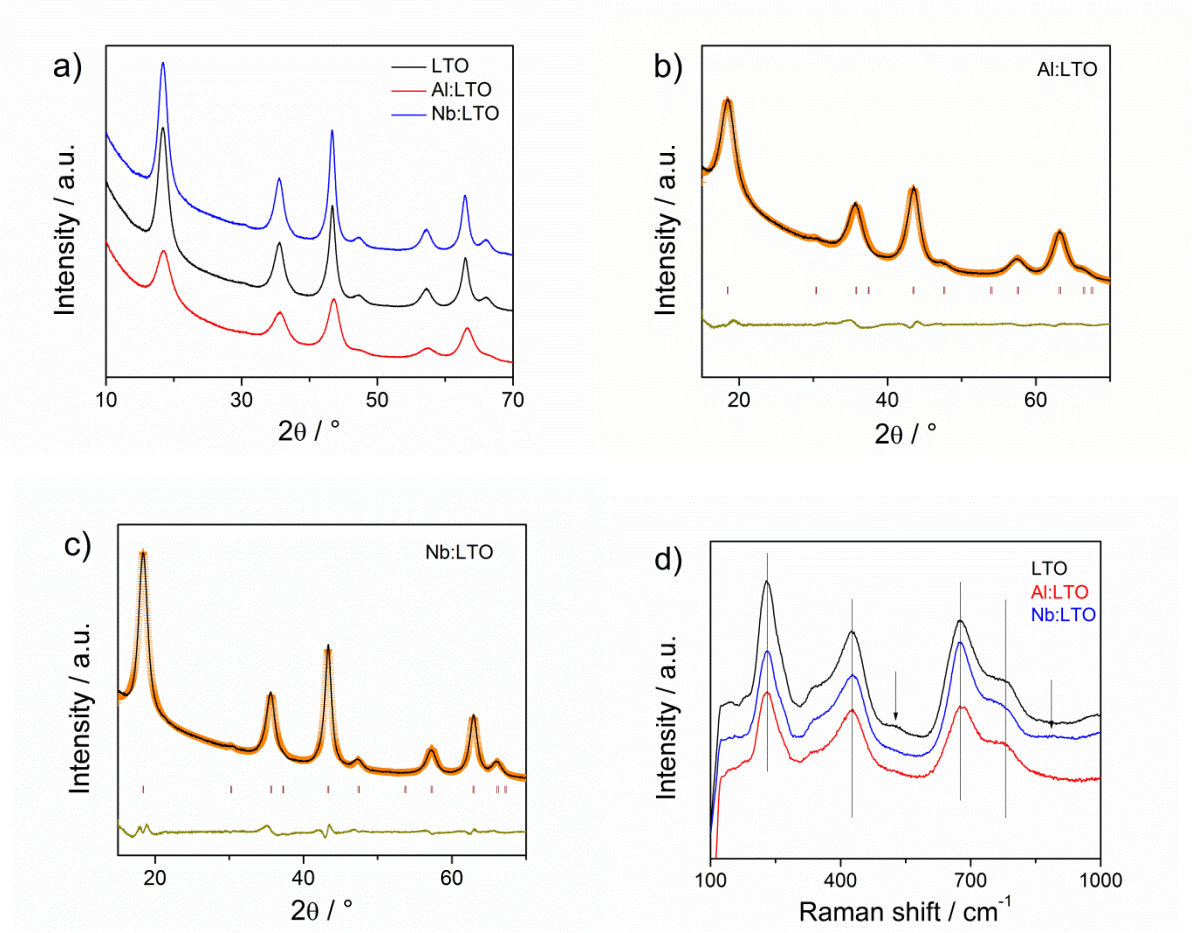

Figure 4.12 Structure of doped LTO nanocrystals. (a) XRD patterns of annealed LTO nanocrystals. (b) and (c) The refined XRD patterns of Al:LTO and Nb:LTO. (d) Raman spectra of doped LTO nanocrystals.

Table 4.2 Refined structural parameters of doped LTO obtained by Rietveld analysis.

	LTO-230	Nb:LTO	Al:LTO	Al:LTO-600
Lattice parameters (Å)	8.3578	8.3593	8.3240	8.3490
Average grain size (nm)	6.8 ± 0.6	5.2 ± 0.9	3.2 ± 0.6	7.6 ± 1.4
Average maximum microstrain	10.2	35.10	93.97	36.73
R_{wp} (%)	8.80	7.02	5.96	3.32
Goodness of fit, χ^2	29.7	9.75	5.23	18.2

The doped LTO nanocrystals were checked by Raman spectroscopy as well for its sensitivity to unit cell changes. The obtained Raman spectra are shown in Figure 4.12 (d). As explained

above, the five characteristic vibrations combined with two defect bands of spinel LTO can be clearly observed. For Nb:LTO sample, one broad and weak vibration band can be found at around 880 cm^{-1}, which is commonly assigned to the vibration mode of the terminal Nb=O bonds.[83, 175, 176] This phenomenon occurred at Nb:TiO_2 as well, seeing chapter 3. From the literature, niobium has the trend to form such terminal bonds on the surfaces for Nb doped materials, independent on preparation methods.[126] Additionally, the antisite defect band at about 510 cm^{-1} is missing after doping.

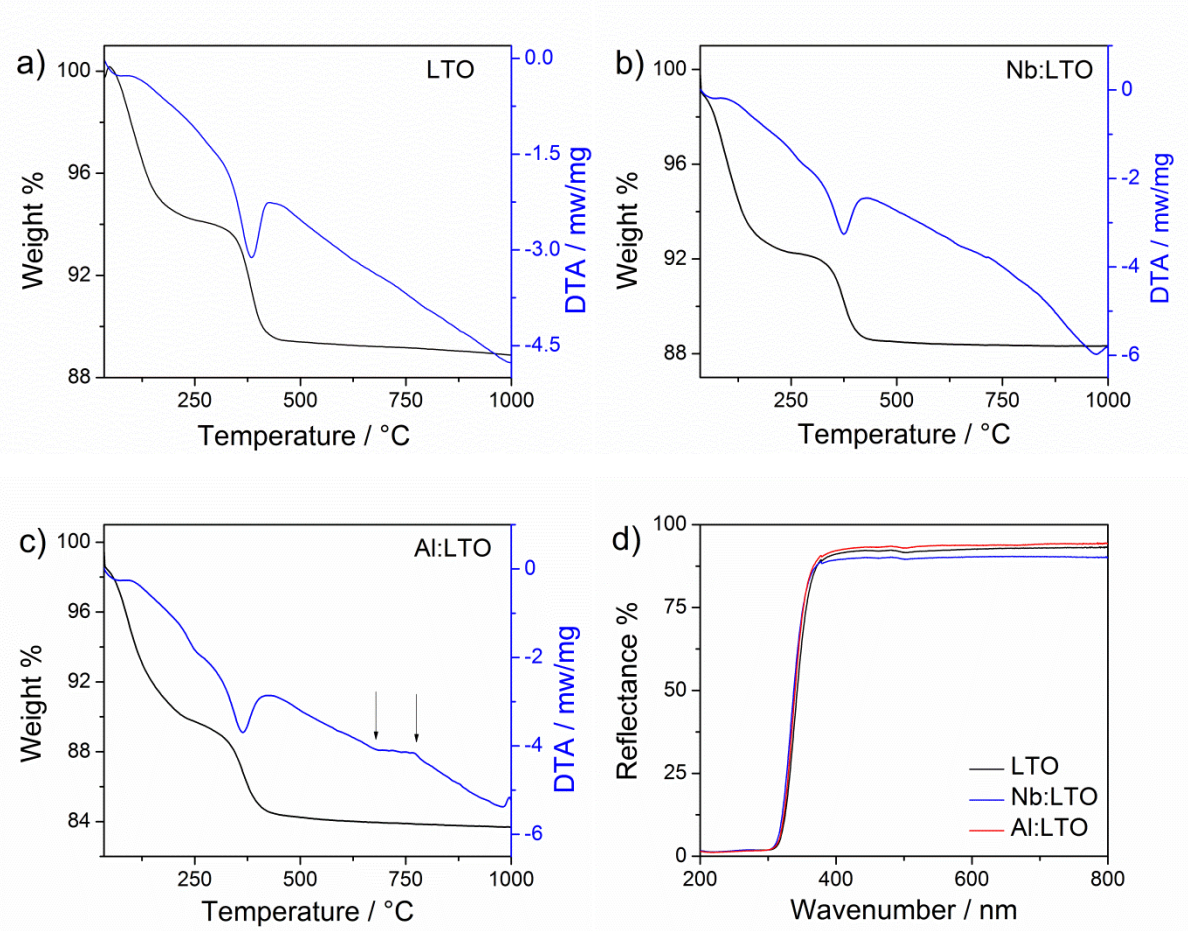

Figure 4.13 Thermal gravimetric analysis and differential thermal analysis of as-made doped LTO nanocrystals. (a) LTO. (b) Nb:LTO. (c) Al:LTO. (d) The UV-visible reflectance spectra of doped LTO nanocrystals.

In order to study whether there are any amorphous phases or not, the thermogravimetric analysis along with differential thermal analysis (TG-DTA) was carried out. Those materials present similar TG curves comprising two weight losses: one below 200 °C assigned to the desorption of water and the other one between 350 to 400 °C derived from the combustion of residual organic compounds. The DTA curve for Nb:LTO is a smoothly gradually decreased curve with a peak around 375 °C. As we know, the crystallization temperatures for anatase TiO_2 and spinel LTO are around 450 and 500 °C respectively. There are no thermal exchange

processes in this temperature range in both cases, which indicates no amorphous TiO_2 or LTO phases in both cases. For Al:LTO, there is a phase transformation process at temperature ranges of 680 to 780 °C, which is corresponding to the formation of the rutile TiO_2 (seeing XRD patterns in Appendix Figure 6b).

To determine the optical bandgap, the UV-visible absorption spectra were carried out on Perkin-Elmer Lambda 750 UV-Vis-NIR spectrophotometer. The results were shown in Figure 4.13. The optical band gap can be deduced following the way introduced in chapter 3, indicating 3.71 and 3.75 eV for Al:LTO and Nb:LTO. The experimental value for optical band gap of bulk LTO is approx. 3.8 eV and no quantum phenomenon appears. In addition, the band gaps barely change even the doping level reaching more than 10 at%.

In order to gain more insight into the composition and chemical state of doped LTO nanocrystals, XPS measurements were carried out. The survey XPS spectra prove the existence of the Al and Nb element and absence of other contaminants except from C. The element content analysis indicates the formula of $Li_{3.7}Ti_{4.8}Nb_{0.2}O_x$ and $Li_{3.1}Ti_{4.35}Al_{0.65}O_x$, which can be confirmed by ICP-MS. The percent ratio between lithium and the sum of titanium and doped element for LTO, Nb:LTO and Al:LTO are 82, 74 and 62 respectively, which indicates the Li^+ ions vacancies induced by doping. Since the surface components of doped LTO are expected to be similar with pure LTO, which is already elaborated above, the chemical state and configuration of metal elements (Ti, Nb, Al) will be paid much attention here. The core level of Ti 2p, Nb 3d and Al 2p are shown in Figure 4.14. To calibrate the charging effects, the C−C peak position was shifted to 284.80 eV. From the XPS spectra of Ti 2p core level, a doublet peak with the area ratio of 2 and splitting energy of 5.70 eV is presented and the binding energy of Ti $2p_{3/2}$ are 458.52 eV for Al:LTO and 258.51 eV for Nb:LTO, which is the same with pure LTO. From XPS spectrum of Nb 3d core level, a doublet peak with area ratio of 1.5 and splitting energy of 2.66 eV was observed and Binding energy of Nb $3d_{5/2}$ is 207.14 eV, which corresponds to Nb^{5+}. The XPS spectrum of Al 2p core level is shown in Figure 4.14 as well and the binding energy for $2p_{3/2}$ and $2p_{1/2}$ are 73.74 and 74.44 eV. There is no reduced Ti^{4+}, Nb^{5+} or Al^{3+} in doped LTO nanocrystals.

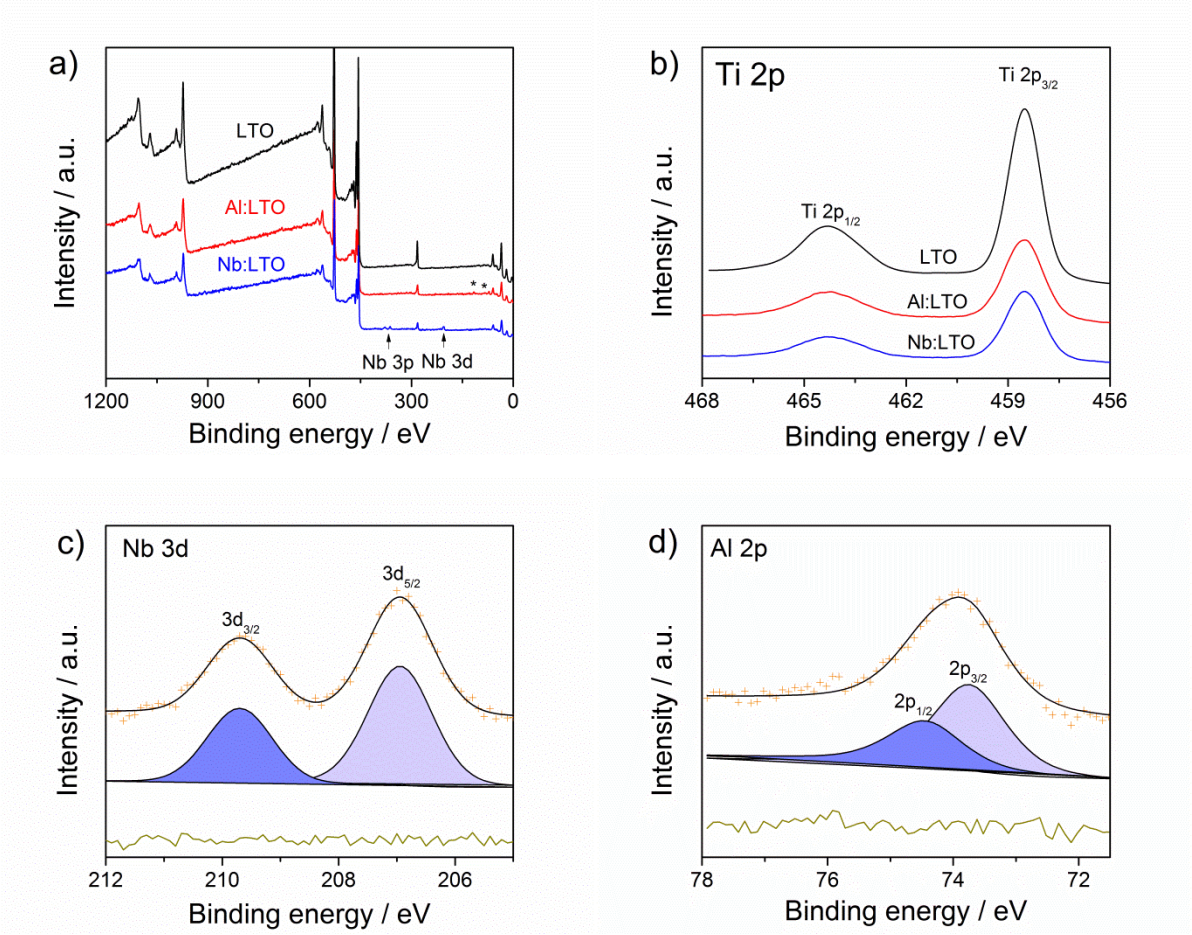

Figure 4.14 XPS survey of doped LTO nanocrystals. (a) XPS survey spectra and (b) Ti 2p core level spectra. Black curves for pure LTO, red curves for Al:LTO and blue curves for Nb:LTO. (c) and (d) XPS spectra of Nb 3d and Al 2p core level. The black curves stand for raw data, orange curves are for the sum of fitting data, and dark yellow curves represent the difference between observed data and fitted data, respectively.

From the element content and electrical neutrality of nanocrystals, we can deduce that Nb^{5+} substitutes the Ti^{4+} as our assumption, which induces some Li vacancies to satisfy the electrical neutrality. The process can be described as

$$Nb_2O_5(Li_4Ti_5O_{12}) \rightarrow 2\,Nb_{Ti}^{\bullet} + 2V_{Li}^{'} + 5O_O^{\times}.$$

For Al:LTO, the Al^{3+} ions were designed to substitute Ti^{4+} to create the Li^{+} ions interstitials, but the fact is much complicated. In fact, the shortage of Li^{+} ions in Al:LTO implies that Al^{3+} ions not only substitute Ti^{4+} ions but also some Li^{+} ions. This process can be a mixture of the two following cases:

$$Al_2O_3(Li_4Ti_5O_{12}) \rightarrow Al_{Ti}^{'} + Al_{Li}^{\bullet\bullet} + V_{Li}^{'} + 3O_O^{\times} \text{ or } 3Al_2O_3(Li_4Ti_5O_{12}) \rightarrow 4\,Al_{Ti}^{'} + 2Al_{Li}^{\bullet\bullet} + 9O_O^{\times}.$$

It is worth noting that the Li^{+} ions located at 8*a* sites are electroactive and will migrate to 16*c* (Wyckhoff) sites during the charge and discharge process. The substitution or deficiencies of Li^{+} ions at 8*a* sites consequently influence the electrochemical performance such as the capacity or the intercalation potential.[84, 177]

In conclusion, from the XRD measurements, the doping elements are well incorporated in the LTO. From TG-DTA analysis, there are no amorphous LTO or TiO_2 phases in (un)doped LTO. From the XPS measurements, there is no reduced Ti^{4+}, Nb^{5+} or Al^{3+} in three samples and the content for Nb and Al are 4 at% and 13 at% respectively. Combining the elements content and crystalline structures, it is deduced that, in case of Nb:LTO, Nb^{5+} ions replace Ti^{4+} ions at 16*d* positions and as a result Li vacancies at 8*a* or 16*d* are created; in case of Al:LTO, Al^{3+} ions not only substitute Ti^{4+} at 16*d* but also Li^{+} ions at 8*a* or 16*d*.

4.3.3 Conductivity measurements

For conductivity measurements, the samples treated at 400 °C for one hour were pressed into a pallet with a diameter of 1.0 cm and a thickness of 0.1 cm. Both sides of the pallet were coated with gold layers with a diameter of 0.8 cm and a thickness of 200 nm as conducting layers. The conductivity measurements were carried out by electrochemical impedance equipment in a temperature-controlled oven where the temperature was stabilized at 25, 45, 65, 85 and 95 °C respectively. The frequency of an AC voltage with amplitude of 50 mV was tuned from 0.01 Hz to 7 MHz. The results are shown in Figure 4.15. The conductivity at 25 °C increases from 2.50×10^{-8} to 3.51×10^{-8} and 1.20×10^{-7} S/cm after Nb^{5+} ions and Al^{3+} ions doping respectively. The conductivity is comparable with the reports from literature.[178, 179] For solid conductivity, the relationship between conductivity and temperature can be described by the Arrhenius equation: $\sigma T = \sigma_{o}\exp\left(-\frac{E_o}{kT}\right)$, where σ is the conductivity (S/cm), T is the temperature (K), σ_0 is the conductivity constant, k is the Boltzmann constant (0.86×10^{-4} eV/K) and E_0 is the activation energy (eV). The activation energy for pure LTO, Nb:LTO and Al:LTO are 0.60, 0.63 and 0.599 eV respectively.

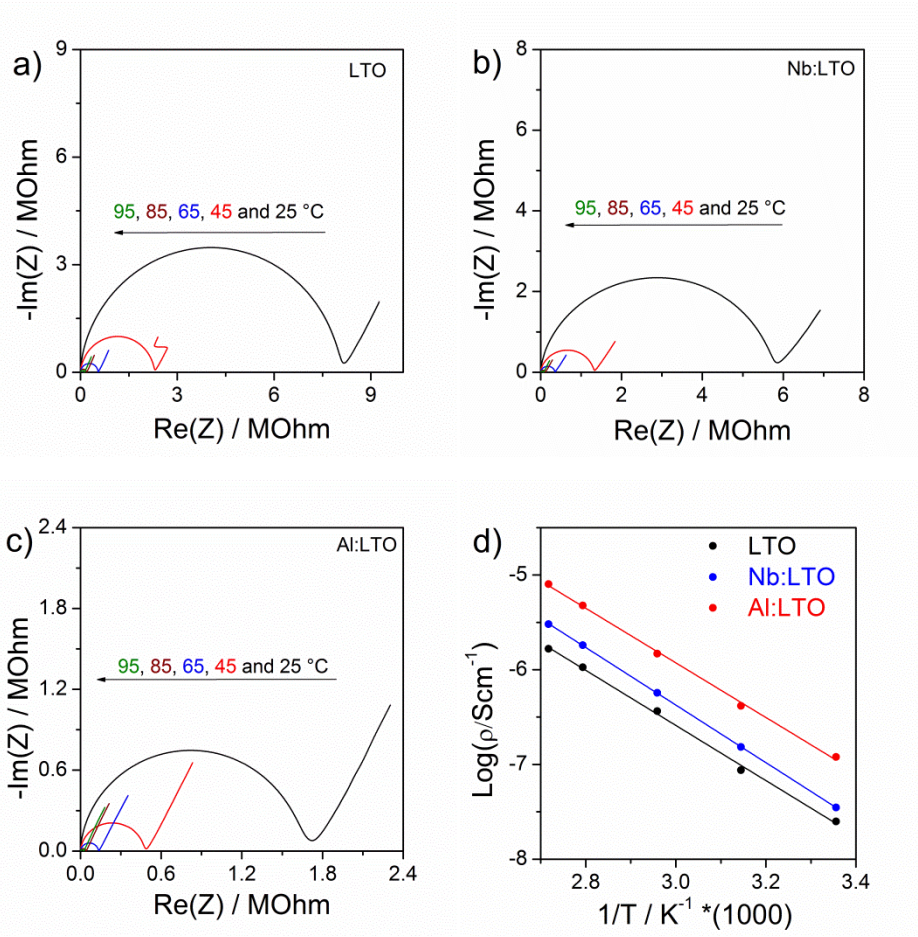

Figure 4.15 Temperature dependent impedance spectra of doped LTO pallets, (a) for LTO; (b) for Nb:LTO and (c) for Al:LTO. (d) Relationship between temperature and conductivity.

Summarily speaking, the conductivity of Al:LTO increases 5 times compared with undoped LTO. One possible reason is the created Li^+ vacancies. The reason for the higher conductivity of Al:LTO than Nb:LTO is the higher doping level.

4.3.4 Doping effect on electrochemical performance

The electrochemical performance of LTO and doped LTO nanocrystals as anode materials in a half-cell with lithium metal as counter electrode were evaluated by galvanostatic charge/discharge profiles. The results are shown in Figure 4.16. The galvanostatic profiles of LTO and Nb:LTO present two typical plateaus with 1.55 V and 1.60 V corresponding to Li^+ ions intercalation and de-intercalation process.[173, 180] The absence of the plateaus of anatase, rutile etc. in the profiles can further confirm the phase pure materials. Compared with commercial LTO materials (the results are shown in Appendix Figure 7a), the profiles of nanomaterials possess gradient slope after the two phase equilibrium plateau due to interfacial charge storage.[47, 60, 136, 181] The decrease of specific capacity of Nb:LTO compared with pure LTO may be attributed to the deficiency of Li^+ ions after the substitution of Ti^{4+} with Nb^{5+}.

The specific capacity of pure LTO and Nb:LTO are still higher than the theoretical value (175 mAh/g), which can be on account of the large interfacial charge storage. This effect is much more obvious in Al:LTO for its smaller crystallite size than pure LTO and Nb:LTO. In case of Al:LTO, the intercalation potential is 1.51 V, lower than the one of Nb:LTO and LTO (1.55 V). There are several possible reasons for this: the first is that the Li^+ ions at 8*a* sites were substituted by Al^{3+}, blocking the Li^+ ions diffusion path; the second is that the great interfacial charge storage distorts the interfacial crystalline structure.

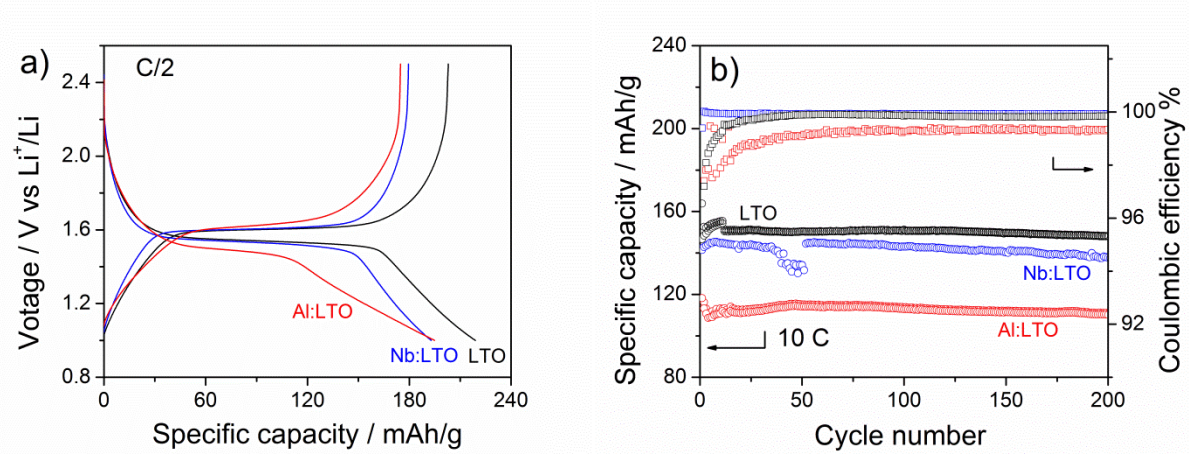

Figure 4.16 (a) Galvanostatic profiles of LTO, Nb:LTO and Al:LTO half cells at C/2 and (b) the cycling capacity and Coulombic efficiency as a function of cycle number.

The cycling stabilities of LTO and doped LTO nanocrystals as anode materials were evaluated at 10C. At high C rates, the counter electrode (lithium foil) can be restructured (dendrites and SEI formed at the surface of Lithium) after long cycling time, which can result in the capacity attenuation. For this reason, the stability measurements were conducted for only 200 cycles and the results are shown in Figure 4.16b. From the results, the specific capacity for all materials decreases to certain extent (150 to 148 mAh/g for LTO, 144 to 138 mAh/g for Nb:LTO and 114 to 110 mAh/g for Al:LTO) after 200 cycles. The Coulombic efficiency for LTO, Nb:LTO and Al:LTO are excellent at 10C, 99.8% for LTO, 99.9% for Nb: LTO and 99.3% for Al:LTO.

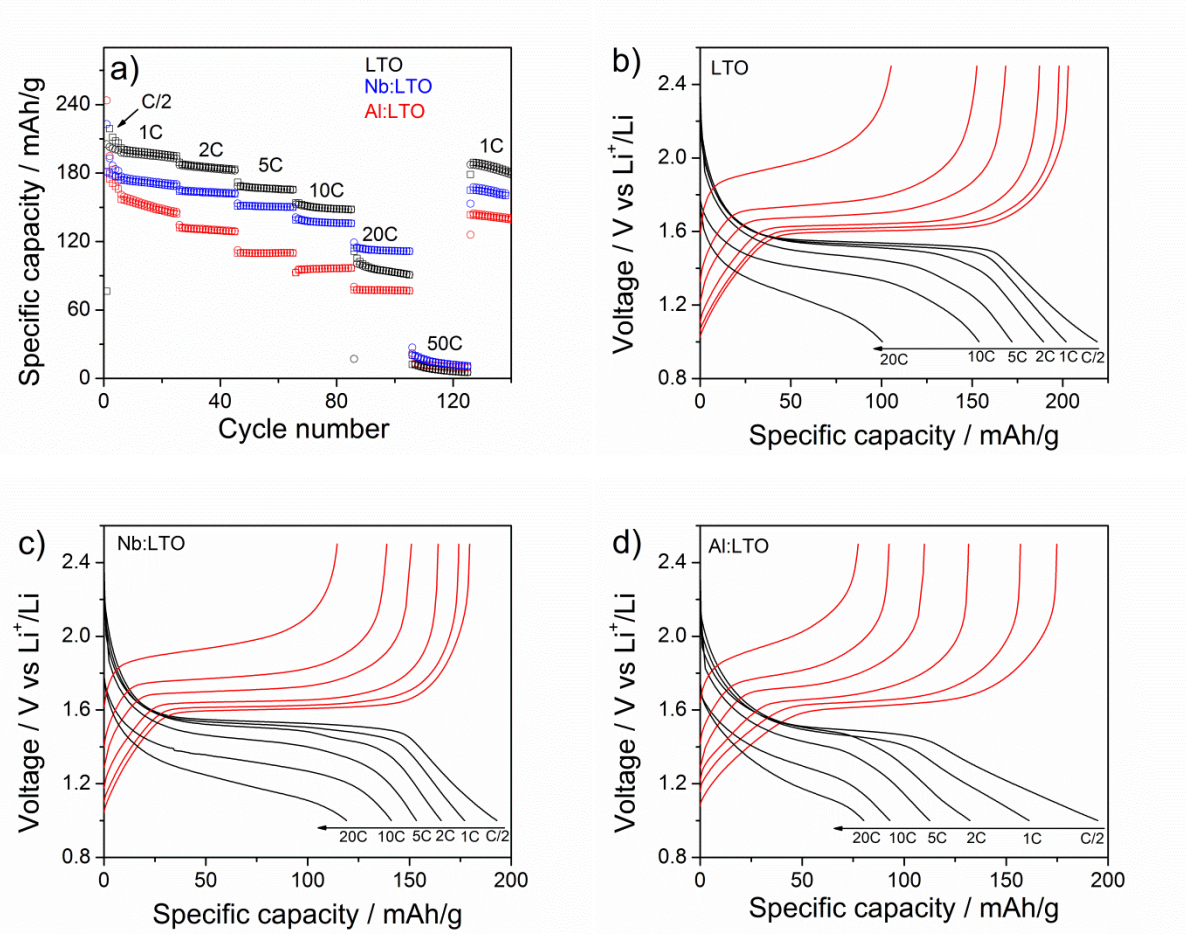

Figure 4.17 Rate capabilities of half cells using doped LTO nanocrystals. (a) After the first five "activation" cycles at C/2 were completed, the rate was gradually increased to 50C. Only the specific lithiation capacities are shown for clarity. (b), (c) and (d) Representative voltage–capacity curves for different C-rates for LTO, Nb:LTO and Al:LTO.

The rate performance of LTO and doped LTO nanocrystals were assessed as well with the charge and discharge rate both increasing from C/2 to 50C, and the rate capacity and voltage-capacity curves are shown in Figure 4.17. At slower charge and discharge rate (less than 10C), pure LTO nanocrystals present the best capacity performance (200 mAh/g at 1C to 153 mAh/g at 10C) compared with Nb:LTO (175 mAh/g at 1C to 140 mAh/g at 10C). On the other hand Nb:LTO possesses less capacity loss than LTO with increasing C-rates and electrochemical performance of Nb:LTO is better than LTO at 20C, which may be derived from the improved conductivity. The specific capacity of Nb:LTO at 20C is around 120 mA/g, much better than commercial LTO and in the literature report.[60, 65, 94, 182] Although the specific capacity of Al:LTO is lower than LTO and Nb:LTO, the stability at fast discharge and charge process (5C, 10C and 20C) is as good as LTO and Nb:LTO. From the profiles, the plateau voltage difference during intercalation and extraction process is gradually increasing and the plateaus nearly disappear at 20C for Al:LTO and LTO due to the ohmic losses. From the results the increased conductivity can buffer the ohmic losses to some extent.

4.4 Summary

In this chapter, LTO nanocrystals with size of several nanometers were successfully prepared based on benzyl alcohol protocol. The reaction conditions such as concentrations, reaction temperature (more than 220 °C), and the precursors of titanium (for its alkoxides) have little effects on crystalline structure of the final products. The residue organic groups on the surface nanocrystals such as benzoic group and unreacted alkoxide group have been proven by XPS, TG-MS and FTIR. They play a crucially important role in dispersing nanocrystals in solvents. The formation mechanism of LTO nanocrystals was studied by GC-MS, indicating different reaction pathway for different precursors of titanium. The main reaction is the Meerwein-Ponndorf-Verley reaction with side reaction of C−C cleavage reaction and benzyl ether elimination reaction. In the following aluminum- and niobium-doped LTO nanocrystals were prepared. Our research shows that the enhanced conductivity arises from Li^+ vacancies after doping. The nanocrystals possess excellent electrochemical performance (120 mAh/g at 20C for Nb:LTO) and barely no attenuation after 200 cycles at 10C.

CHAPTER 5
POROUS LTO STRUCTURES FROM SOL-GEL PROCESS AND NANOCRYSTALS

5.1 Preparation of mesoporous LTO from sol-gel process

Porous networks surrounded by nanocrystals have been regarded as one of most efficient approaches for the fabrication of next-generation energy storage materials on account of the available electrolyte-transport access. Mesoporous LTO films from sol-gel process were prepared by dip- or spin-coating in the previous reports, but those methods are not practical for producing micrometer-thick electrodes for commercial LIBs.[69, 77, 183] Furthermore, the synthesis approaches for mesoporous thin films with crystalline framework cannot be directly transferred to the generation of corresponding mesoporous powders. One reason for this is that the crystallization process will result in a severe restructuring. The tailor-made copolymer of PIB_{50}-*b*-PEO_{45} possesses higher combustion temperature and forms big and stable micelles. Those features are beneficial for preparing porous materials. Here mesoporous LTO powders were synthesized based on the PIB_{50}-*b*-PEO_{45} template.

The preparation of mesoporous LTO powder is in the following way. A solution is prepared by dissolving lithium acetate (104.0 mg), titanium(IV) butoxide (670.4 mg) and PIB_{50}-*b*-PEO_{45} (80 mg) in a mixed solvent of ethanol (2 mL), 2-methoxyethanol (2 mL) and glacial acetic acid (0.3 mL). The homogeneous solution was transferred into a petri dish and dried at the climate chamber at room temperature. The dried samples were aging at 300 °C for 4 hours. Eventually, the LTO powder was crystallized at the temperatures ranging from 600 °C to 700 °C at different ramp of 5 °C/min and 10 °C/min. The copolymer not only plays a role of a structure directing agent but also stabilizes the gel products by chelating with metal ions. Therefore without the copolymer, it is impossible to prepare phase-pure LTO in our case. The precise control of heat treatment can guarantee the phase-pure material with mesoporisty.

5.1.1 The effect of heat treatment on the crystalline structure

Powder X-ray diffraction and Raman spectroscopy were used to analyze the phase composition after heat treatment with different temperature stages and heating rates. Representative XRD pattern of LTO heated to 600 °C at a rate of 10 °C/min is shown in Figure 5.1a. This material exhibits the desired crystalline spinel structure in accordance with the JCPDS card No. 26-1198 for cubic LTO ($Fd\bar{3}m$) and no other phases are found. The XRD pattern was analyzed by the Rietveld refinement. The *R*-factors are R_p=11.9 %, R_{wp}=10.7 %, R_{exp}=2.5% (χ^2=18.1) and reveal a reasonable fitting. The average crystallite size for LTO is

7.5 ± 0.5 nm. XRD data collected using automatic divergence slits are able to decrease the limited detection concentration of different phases (seeing Figure 5.1b). The measurement indicates the impurity phase of monoclinic Li_2CO_3 (less than 3 wt%) and the fraction of anatase TiO_2 is <1 wt% (below the detection limit). The impact of the polymer on the crystallization process was investigated by preparing LTO powder in the same protocol without using polymers (seeing Appendix Figure 8a). Other reflections of anatase TiO_2 are clearly observed and the refinement analysis of this pattern indicates the amount of around 10 wt%. Consequently the copolymer PIB_{50}-*b*-PEO_{45} is crucial for preparing phase-pure LTO powder.

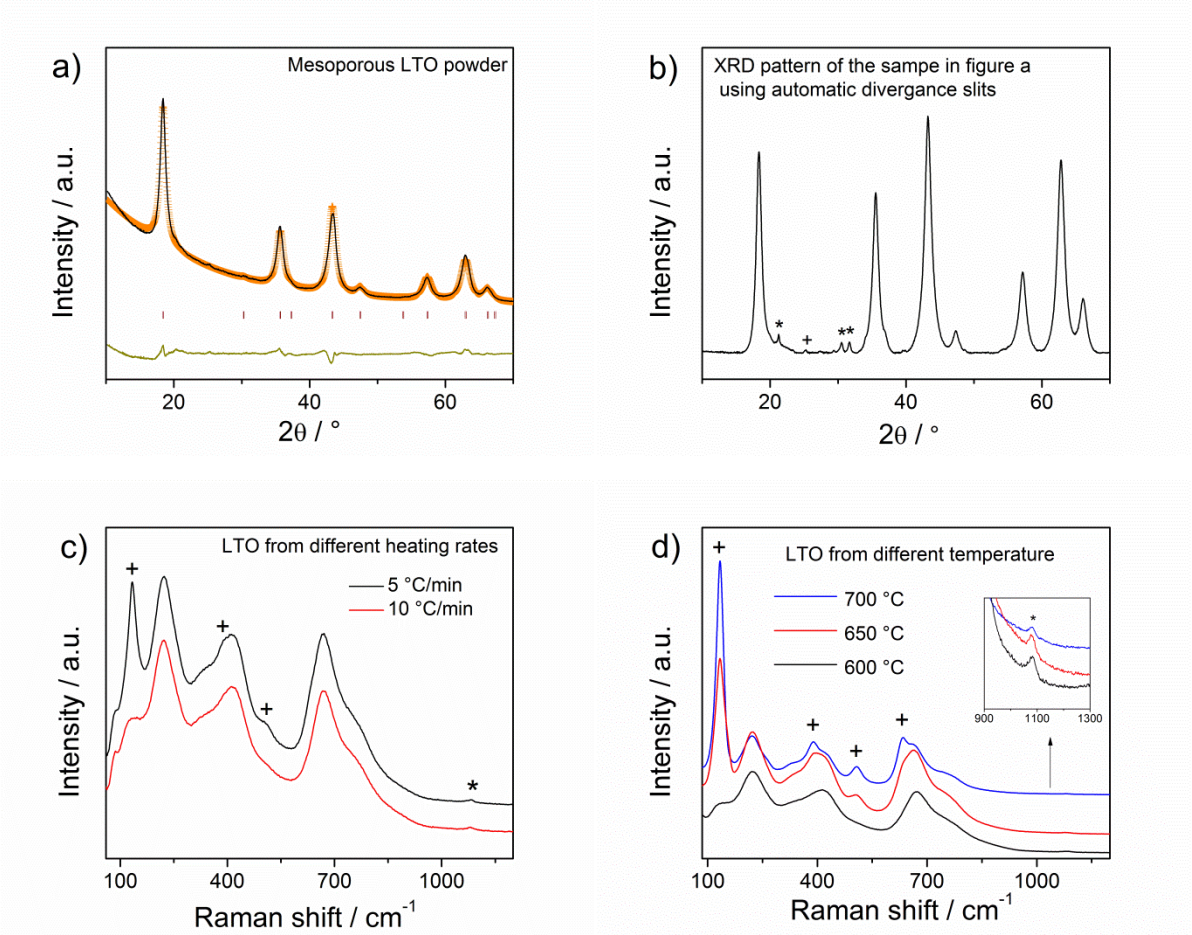

Figure 5.1 (a) Rietveld refinement of XRD pattern of prepared mesoporous LTO after heating to 600 °C (10 °C/min). Black solid curve and orange curve represent the experimental and fitting curves. The bars stand for peak position. (b) XRD pattern of the same sample as in (a) using automatic divergence slits during XRD measurements. (c) Raman spectra of mesoporous LTO heated at rates of 5 °C/min and 10 °C/min to 600 °C. (d) Raman spectra of mesoporous LTO heated to 600, 650 and 700 °C at rates of 10 °C/min and the zoom-in figure in the range of 900 to 1300 cm^{-1}. All impurity anatase (TiO_2) signals are indicated by "+" and Li_2CO_3 signals are marked by asterisks.

Raman spectra of mesoporous LTO prepared at different heating rates (5 °C/min and 10 °C/min) are presented in Figure 5.1c. Overall, all of predicted Raman bands (employing a

rate of 10 °C/min) at approx. 221 cm^{-1} (F_{2g}), 271 cm^{-1} (F_{2g}), 352 cm^{-1} (F_{2g}), 418 cm^{-1} (E_g) and 670 cm^{-1} (A_{1g}) are from vibration bands of spinel LTO, in fair agreement with the previous results of LTO nanocrystals. The defect-related band mode 748 cm^{-1} (shoulder) is attributable to antisite defects. Additionally, a weak Raman band located at 1081 cm^{-1} is attributed to the symmetric stretching vibration of carbonate in Li_2CO_3.[184] With the increase of temperature, the peak intensity is getting weaker and weaker. Interestingly, the heating rates and final temperatures both possess strong influence on the phase composition. Raman spectra of LTO samples subjected to 650 and 700 °C at a rate of 10 °C/min) are shown in Figure 5.1d. The Raman bands of anatase TiO_2 located at about 135 cm^{-1} (E_g), 390 cm^{-1} (B_{1g}), 510 cm^{-1} (A_{1g} + B_{1g}) and 630 cm^{-1} (E_g) can be clearly observed when the heating rate and final temperature were tuned. From the above analysis, a strictly-controlled heat treatment is required to avoid the formation of anatase phase.

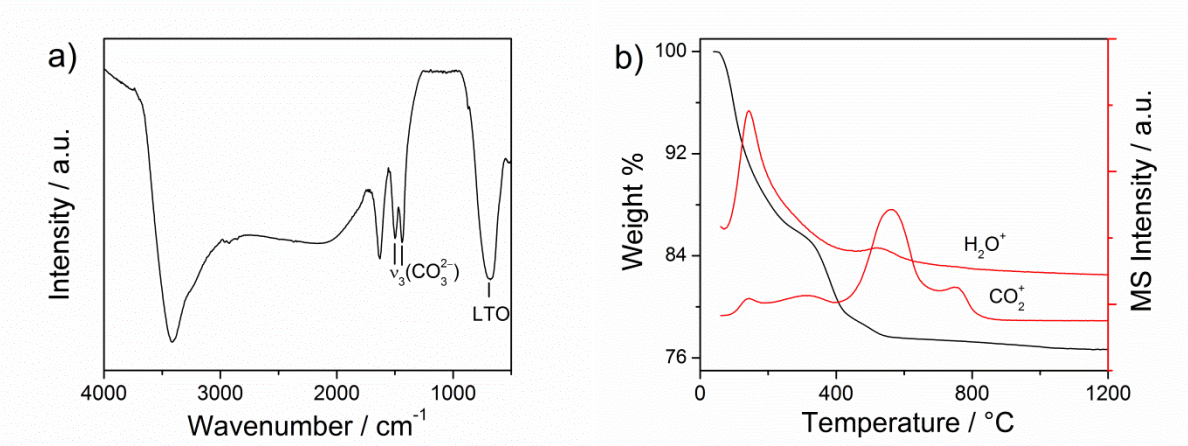

Figure 5.2 (a) KBr-pellet FTIR spectrum and (b) TG-MS data of the precursor mixture. The major decomposition of both the polymer and inorganic precursor compounds occurs in the temperature range between 200 and 400 °C. Formed Li_2CO_3 decomposes at $\vartheta \geq 700$ °C (see shoulder in the CO_2^+ signal).

The FTIR spectrum of mesoporous LTO powder is shown in Figure 5.2a. A pronounced double band at 1440 and 1500 cm^{-1} can be assigned to $\nu_3(CO_3^{2-})$ asymmetrical stretching vibrations of Li_2CO_3 while the absorption at about 680 cm^{-1} is derived from the F_{1u} vibrational mode of the spinel lattice.[184] Not surprisingly, two intense bands are centered at 1630 cm^{-1} (O−H bending vibration; δOH) and 3400 cm^{-1} (O−H stretching vibration; νOH) from adsorbed water. The formation of minor amounts of Li_2CO_3 is suggested in following way: the sol-gel derived LTO reacts with gaseous CO_2 from the thermal combustion of the PIB_{50}-*b*-PEO_{45}. Similar behavior has been observed for Li_2O and synthetic lithium ceramics, such as Li_2ZrO_3 and Li_4SiO_4. These materials readily react with CO_2 to form carbonate species at elevated temperatures.[185] The decomposition temperature of Li_2CO_3 is more than

700 °C, which is confirmed by TG-MS (Figure 5.2b). Although mesoporous LTO contains trace amounts of Li_2CO_3, it has been shown that its presence can be beneficial for the stabilization of porous mesostructures, moreover, it does not negatively affect the electrochemical properties.[160, 186, 187]

5.1.2 In-depth XPS analysis of mesoporous LTO

To gain more insights into the atomic bonding configuration and chemical composition of mesoporous LTO, XPS measurements with Ar^+ etching process were carried out. Figure 5.3 depicts XPS scans of survey spectrum and the C 1s and Ti 2p core levels before and after "etching" with Ar^+ ions. XPS in combination with Ar^+ ion sputtering permits depth profiling and allows the identification of the chemical composition of the particle surface. Associated survey spectra can be found in Figure 5.3 a. The XPS survey has revealed that C, Li, Ti, and O core levels can be found apart from a weak Ar signal after the sputtering process. The Ti 2p spectrum in Figure 4.3 b shows a single doublet of the $2p_{3/2}$ and $2p_{1/2}$ lines due to spin-orbit splitting at binding energies of (458.44 ± 0.05) eV and 464.14 ± 0.05) eV, in line with LTO nanocrystals mentioned in the above chapter. It is well known that the Ti^{4+} ions will become partially reduced to Ti^{3+} and Ti^{2+} after sputtering. When looking at the deconvoluted C 1s core level spectrum, in total four XPS peaks can be distinguished at binding energies of (284.80 ± 0.05) eV, (286.37 ± 0.05) eV, (288.82 ± 0.05) eV and (289.88 ± 0.05) eV due to carbon species with different chemical bonding/oxidation states. The lowest binding energy can be attributed to C−H or C−C bonds, whose quantity remains virtually constant over the entire sputtering process. Additionally, the medium binding energies can be assigned to C−O−C and O−C=O bonds from incompletely combusted templates. Lastly, the highest binding energy is due to Li_2CO_3, whose content substantially decreases with increasing sputtering time, which leads us to consider that created carbonate is largely situated on the surface. This fact can be justified with the consideration that residual carbon from the thermal decay process preferably combusts on the solid/air interface by the supply of ambient (atmospheric) oxygen. Finally, the XPS analysis confirms the results from the XRD, FTIR and Raman measurement and suggests significant amounts of Li_2CO_3 accumulated on the surface.

The optical properties of the polymer-templated LTO powder were investigated by UV-Visible reflectance spectrum (showing in Figure 5.3d). The analysis based on the method mentioned in Chapter 3 indicates an indirect band gap $E_{bandgap}$=3.43 eV, slightly smaller than the results of nanocrystals.

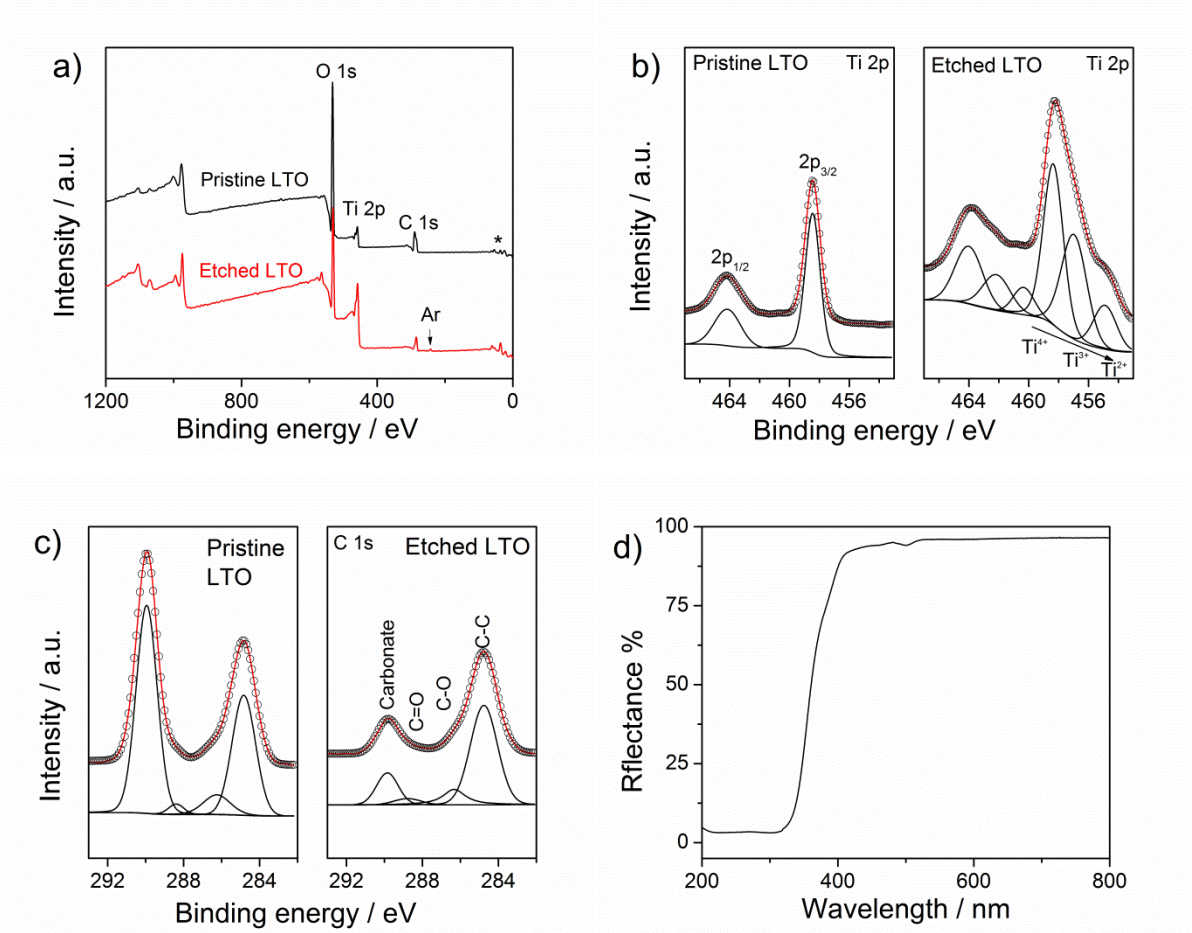

Figure 5.3 XPS survey spectrum of the mesoporous LTO powder heated to 600 °C at a rate of 10 °C/min. The asterisk mark indicates Li 1s core level regions at low binding energy. High-resolution XPS scans of the Ti 2p (b) and C 1s (c) core level prior to and after Ar^+ sputtering. (d) The UV-visible reflectance spectrum of mesoporous LTO powder.

5.1.3 Morphology and porosity of mesoporous LTO

Morphology of mesoporous LTO powder was investigated by SEM and TEM, shown in Figure 5.4. The samples exploited from the dish are bulk-like with size of around hundred micrometers. From the high-resolution SEM and TEM, the pore structure is ordered, and pore size distribution in samples is uniform and average size is approx. 9 nm (Figure 5.4b and c). High-Resolution TEM shows that numerous crystals surrounding the pores are connected with each other to form mesoporous bulks. The crystallite size from TEM observation is around 10 nm, which is in line with the results of XRD refinement.

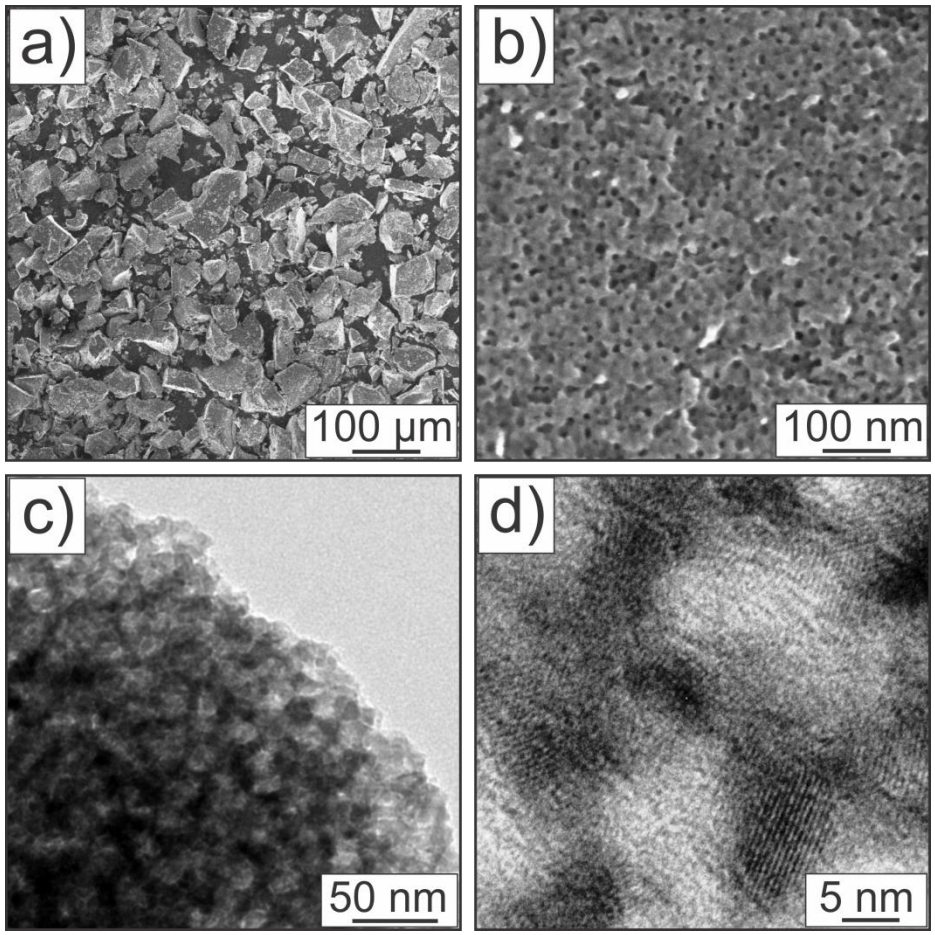

Figure 5.4 Morphology of mesoporous LTO powders heated to 600 °C at a rate of 10 °C/min. SEM images with low magnification (a) and high magnification (b). TEM images with low (c) and high magnification (d).

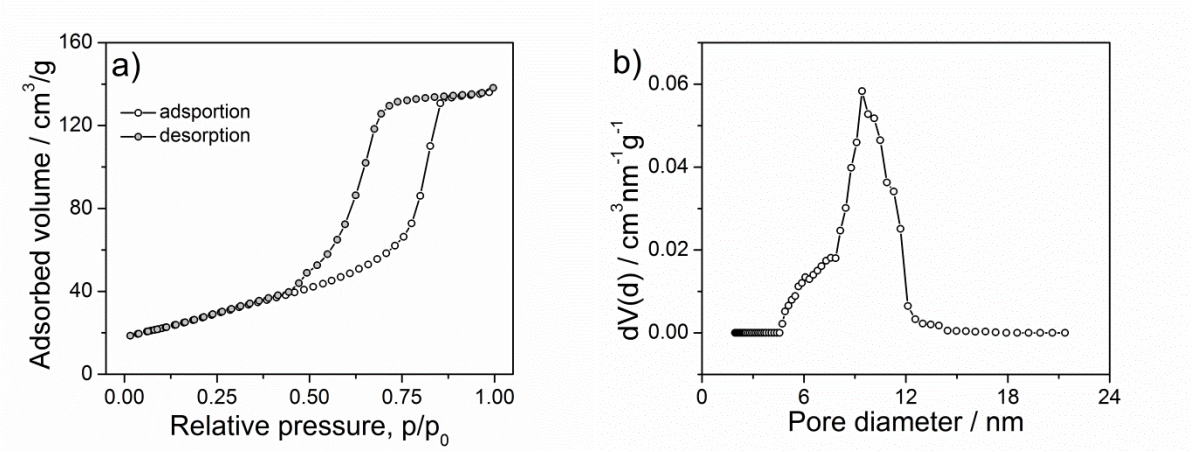

Figure 5.5 (a) N_2 physisorption isotherms at 77 K of mesoporous LTO powder heated to 600 °C employing a rate of 10 °C/min. (b) Corresponding pore size distribution obtained by NLDFT method based on adsorption branch.

To investigate the mesoporosity, N_2 physisorption was performed at 77 K (see Figure 5.5a). The isotherm corresponds to type IV according to the classification from IUPAC recommendations and exhibits H1 type hysteresis. A recently developed NLDFT model (nonlocal density functional theory) assuming spherical and cylindrical shape is applied to the

adsorption branch for the determination of the pore size distribution, shown in Figure 5.5b. The analysis provides a pore size distribution of 6 to 12 nm, centering at an average diameter of (9 ± 1) nm, which is in good accordance with the results from SEM. The total mesopore volume is 0.20 cm^3/g, indicating approx. 40% porosity with respect to the whole volume, while the specific surface area is 100 m^2/g. The high surface area and continuous pores can provide an access of electrolyte to the surface of active materials, which favors materials with high rate capacity.[41, 129, 188]

5.1.4 Electrochemical performance of mesoporous LTO

The electrochemical performances of mesoporous LTO powders were conducted at BELLA lab in KIT under the assistance of Dr. Torsten Brezesinski and the data were published in *ChemNanoMat* **2015,** 1, (6), 415-421.

The working electrode was fabricated by coating a water-based slurry with 80 wt % LTO and 5 wt% poly(vinyl alcohol) [PVA] and 15 wt% carbon black. PVA was chosen as the polymer binder for its favourable dispersion and adhesion properties.[189] The data were collected in the range of 1.0 and 2.5 V with respect to Li^+/Li by a MACCOR battery cycler and 1C is corresponding to175 mAh/g. The galvanostatic charge and discharge profiles of the tenth and 100th cycles at C/2 are shown in Figure 5.6b. The profiles present a distinct insertion and extraction plateau at 1.55 and 1.60 V, respectively. These plateaus are the feature of the transformation of LTO to rock salt-type $Li_7Ti_5O_{12}$ and vice versa. After 100 cycles at C/2, the overpotential (potential difference between intercalation and de-intercalation process) scarcely increase, thereby indicating the excellent cycle stability of the half-cells. The cycle stability and Coulombic efficiency at C/2 are shown in Figure 5.6a. The large capacity loss at first cycle is attributable to the non-negligible amounts of surface functional groups on the surface of LTO, as indicated by XPS. The Coulombic efficiency can reach to nearly 100% after 50 cycles. The cycle stability of the half-cells is excellent with only 4.6% attenuation between the fifth and 300th cycles.

The rate performance of the mesoporous LTO as anode material for LIBs is shown in Figure 5.6c, and corresponding charge/discharge profiles are presented in Figure 5.6 d. The specific capacity fades by only 12% when the C-rate is increased to 5C and even at 10C the half-cells deliver a specific capacity of more than 100 mAh/g. Thus the data in Figure 5.6 (c) and (d) suggests that mesoporous LTO are in principle suitable for high power applications.

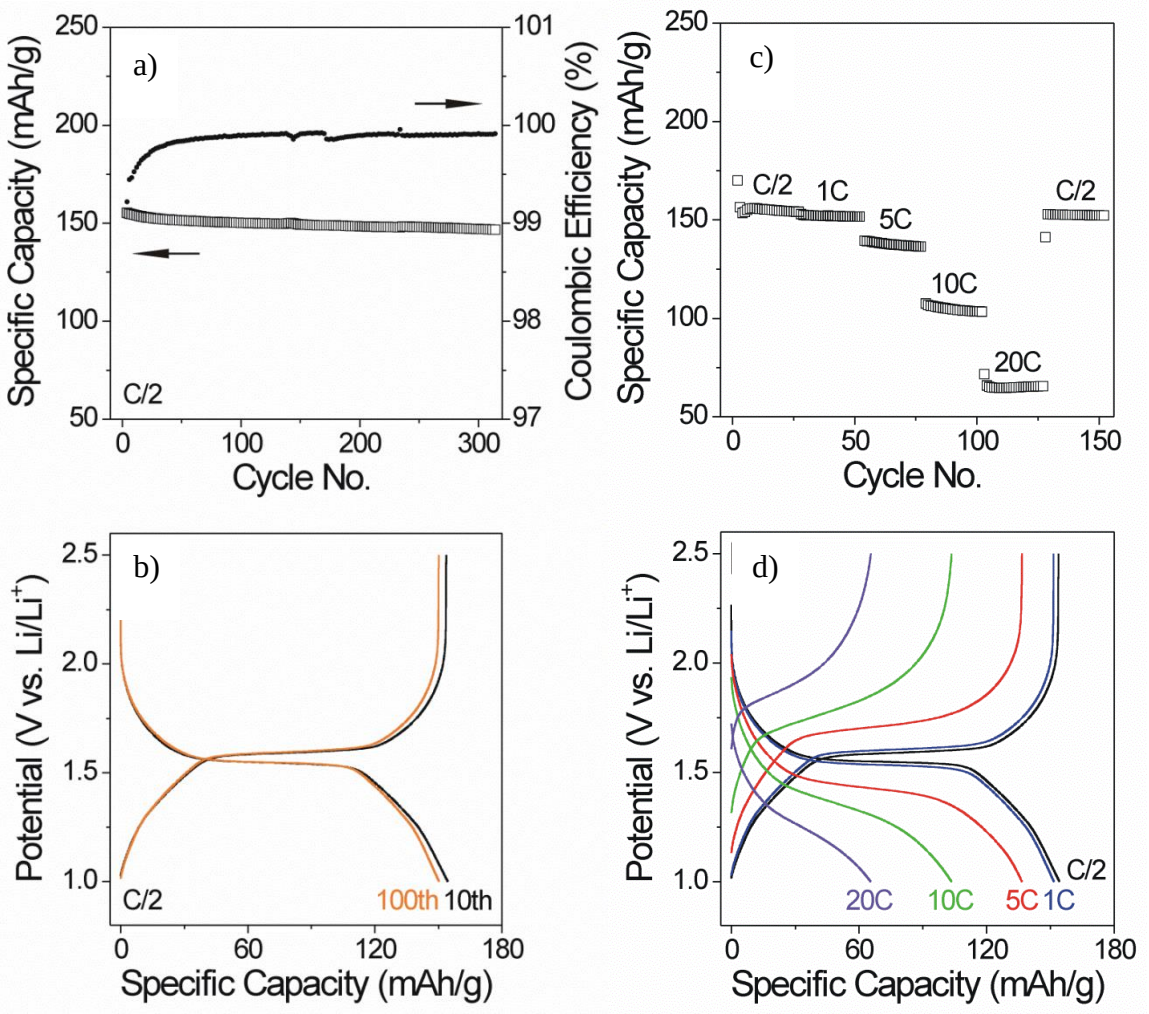

Figure 5.6 The electrochemical performance of mesoporous LTO powders. (a) Both the specific capacity and Coulombic efficiency are shown as a function of cycle number. (b) Galvanostatic charge and discharge profiles for the 10th and 100th cycles. (c) Rate capability of the LTO half-cells. (d) The voltage-capacity curves at the different C-rates.[76]

5.2 Porosity effect on electrochemical performance

As shown above, it is possible to prepare mesoporous LTO powder using sol-gel process, but it requires well-controlled heat treatment process to avoid anatase phase. The electrochemical performance (including specific capacity and rate capacity) of the mesoporous powder are not as good as the nanocrystals mentioned in chapter 4. Since the nanocrystals and mesoporous powders possess different specific surface area and crystallite sizes and both of differences have significant impacts on the electrochemical performance, it is not reasonable to evaluate the impact of mesoporosity on electrochemical performance by the direct comparison of these two systems (the nanocrystals and mesoporous powders from sol-gel process). The LTO nanocrystals mentioned in chapter 4 provide a chance to prepare different pore size systems with similar crystallinity and specific surface area and such porous systems are suitable to assess the function of different porosities in electrochemical charge storage system. In the

following sections, EISA and electrospinning are used to fabricate LTO thin films with different pore size systems and mesoporous LTO fibers based on nanocrystals assembly, and their electrochemical performance will be studied as well.

5.2.1 Preparation of porous LTO films from preformed nanocrystals

The dip-coating solution for mesoporous films (PIB_{50}-*b*-PEO_{45} templated films) is prepared in the following way: 60 mg LTO nanocrystals were dispersed into 1 mL water and a solution containing 45 mg PIB_{50}-*b*-PEO_{45} in mixture solvents of 0.5mL ethanol and 0.5 mL 2-methoxylethanol was added into LTO dispersion drop by drop. Then the homogenous dip-coating solution was obtained. The parameters for dip-coating are the speed of 5 mm/s, the humidity of 75 RH%, and temperature of 15 to 20 °C. The as-made film was dried at 120 °C for 3 h and then stabilized at 300 °C for another 6 h. PIB_{50}-*b*-PEO_{45} can be removed by heating up to 600 °C at the ramp of 10 °C/min.

The macroporous (80 nm polystyrene beads templated) LTO films was prepared following the way published before[190]: the dip-coating solution is composed of 2 mL 3 wt% polystyrene beads dispersion and 0.6 mL 5 wt% LTO nanocrystals dispersion. The parameters for dip-coating are the speed of 5 mm/s, the humidity of 80 RH%, and temperature of 15 to 20 °C. After drying, the film was subjected to UV radiation for 12 hours to remove PS beads.

5.2.2 Morphology of porous LTO films

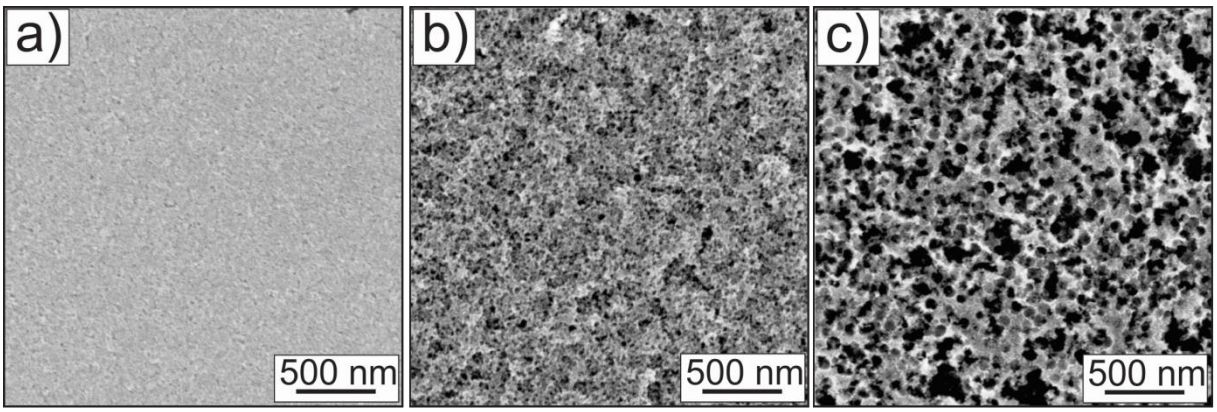

Figure 5.7 Morphology of LTO films. (a) untemplated film, (b) mesoporous film and (c) macroporous film.

Untemplated, mesoporous and macroporous LTO films are all prepared by dip-coating and the optimized preparation conditions are shown above. The morphology of untemplated, mesoporous and macroporous LTO films are shown in Figure 5.7. No cracks can be found in untemplated film. Figure 5.7b shows the morphology of mesoporous LTO film, indicating the

pore sizes in the range of 10 to 20 nm. The mesoporous pores are not arranged as orderly as the films from sol-gel process. In additional, the mesopores in TiO_2 films obtained from nanocrystals shown in chapter 3, are much more ordered than the pores in LTO film. The reason behind will be elaborated in the following section. The morphology of macroporous film is shown in Figure 5.7c. The pore size is around 80 nm, identical to the template size. As studied in the literature, it is a challenge to obtain the ordered macroporous films from the co-assembly of 80 nm PS beads and nanocrystals.[190]

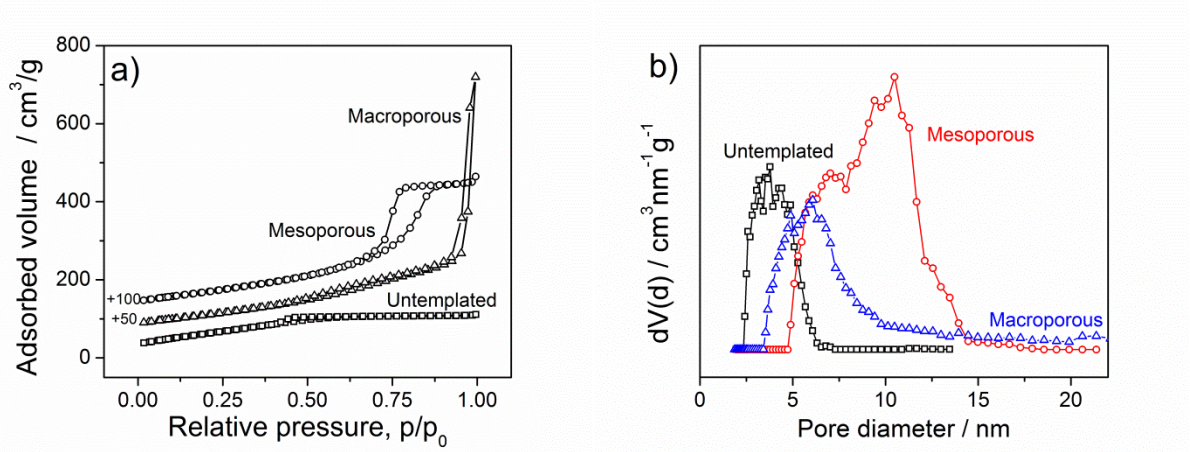

Figure 5.8 N_2 physisorption isotherms (77 K) of porous LTO powders and the corresponding pore size distribution obtained by NLDFT based on adsorption branch. Black, red and blue curves are for untemplated, mesoporous and macroporous LTO powders, respectively.

The porosity was analyzed in detail *via* N_2 physisorption at 77 K on their powder products and the isotherms are shown in Figure 5.8. The specific BET surface area of untemplated, mesoporous and macroporous LTO are almost the same, 235, 254 and 224 m^2/g, respectively. The specific surface area is comparable with the preformed nanocrystals. The similar surface area can avoid the effect of surface area on electrochemical performance. The isotherm of mesoporous products presents type IV according to the classification from IUPAC recommendations and exhibits H1 type hysteresis, indicating spherical or cylindrical continuous pores. The pore size distribution based on the NLDFT calculation from adsorption branch indicates 5 to 15 nm for mesoporous powder, comparable with the results of mesoporous powder from the sol-gel process. The isotherms and pore size distributions of untemplated and PS beads templated powders are shown in Figure 5.8 as well. The pore sizes for untemplated and macroporous films are from 2.5 to 6 nm and 4 to 10 nm, respectively, which may be derived from the interspace between nanocrystals.

5.2.3 Electrochemical performance of porous LTO films

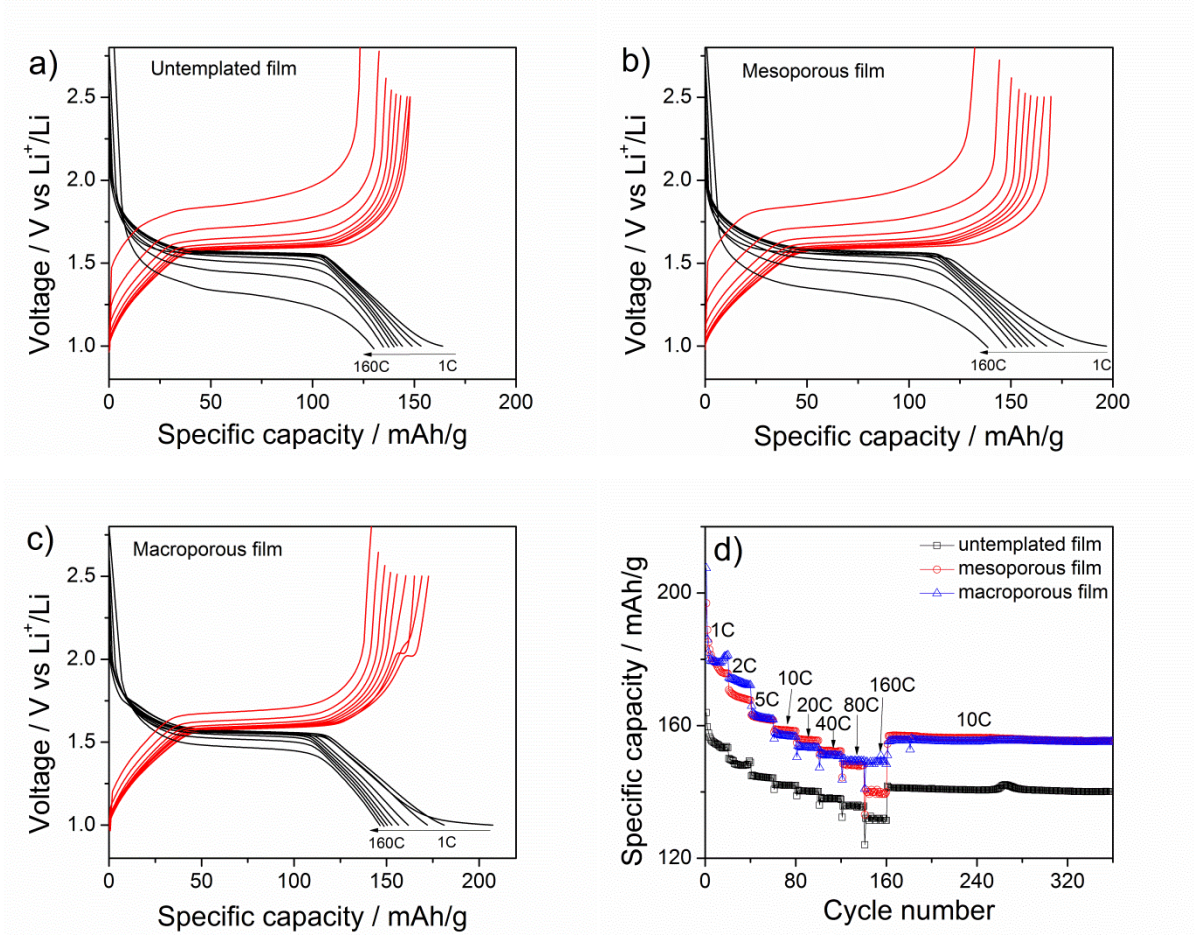

Figure 5.9 Galvanostatic profiles at different discharge and charge rates of LTO films in 1 M $LiClO_4$ in propylene carbonate. (a) untemplated film. (b) Mesoporous film. (d) Macroporous film. (d) Specific capacities of untemplated, mesoporous and macroporous LTO films at different C-rates, 1C=175 mAh/g. The active material mass was estimated from CV data shown in Apendix Figure 8. The charge and discharge rates are 1C, 2C, 5C, 10C, 20C, 40C, 80C and 160C.

The galvanostatic charge and discharge profiles of LTO films with different pore sizes are shown in Figure 5.9. The voltage plateau at 1.55 V and 1.60 V (at 1C) represents the two phase region where lithium-poor phase (spinel $Li_4Ti_5O_{12}$) and lithium-rich phase ($Li_7Ti_5O_{12}$) coexisted during the Li^+ insertion and extraction. For macroporous film, trace anatase induces the second plateau at 1.75 and 2.0 V, which can be confirmed by cyclic voltammograms (seeing Appendix Figure 10). As the discharge and charge rate increases, the overpotential significantly increases, especially for dense film and mesoporous film, which is caused by kinetic-limited concentration polarization. For the macroporous film, the overpotential increases in a small magnitude. Pores lying in the films provide diffusion path for electrolytes, which can be a buffer for such polarization at fast charge and discharge process.

The specific rate capacity of LTO films at different discharge and charge rate are shown in Figure 5.9d. The specific capacity at the charge and discharge rate of 160C for macroporous, mesoporous and dense LTO films are 149 mAh/g and the 140 mAh/g for and 132 mAh/g respectively. Such high rate capacity is mainly attributed to the porous system. After 200 cycles at a rate of 10C, the capacity decrease from 155.5 to 155.1 mAh/g, from156.8 to 155.4 mAh/g and 141.7 to140.1 mAh/g for macroporous, mesoprous and dense film respectively, indicating the excellent stability for all films.

5.2.4 Formation mechanism of mesopores

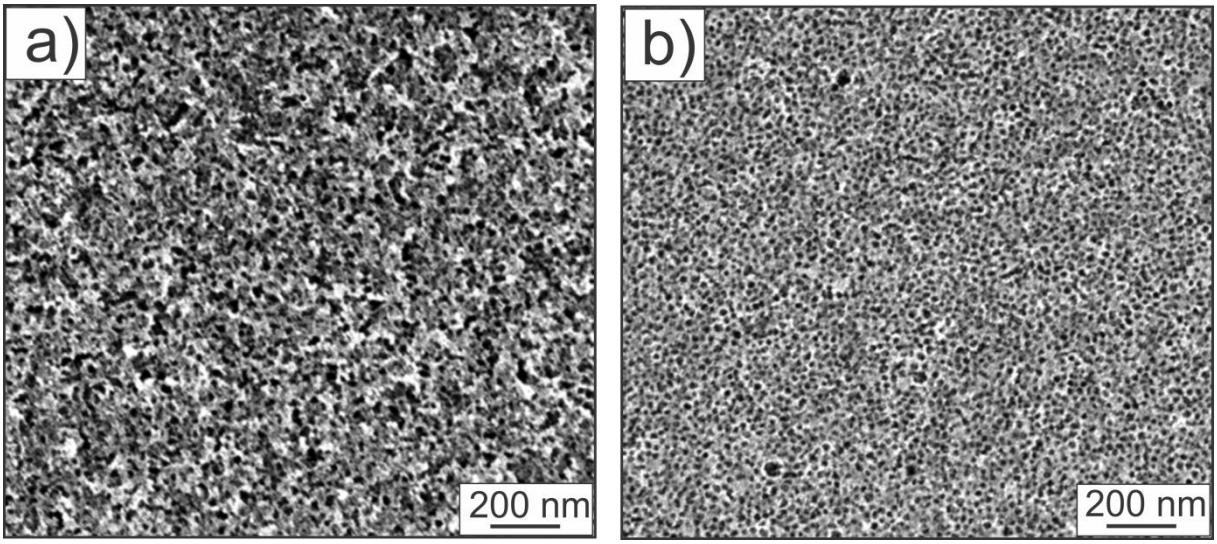

Figure 5.10 SEM images of mesoporous LTO (a) and TiO_2 (b) films

Figure 5.10 compared the mesoporous LTO and TiO_2 films both prepared from their nanocrystals. The mesoporous structure in TiO_2 film is much more ordered than in LTO film. These can be caused by two different preparation parameters. One of them is the solvent composition. Only 10 vol% water was used for preparation of mesoporous TiO_2 films while 50 vol% water for LTO. The other difference is the nanocrystal. Therefore the properties of the copolymer of PIB_{50}-*b*-PEO_{45} in different solvents were first studied. The DLS measurements of PIB_{50}-*b*-PEO_{45} in pure water and mixture solvents of water and ethanol with volumetric ratio of (1:1 and 1:9) are shown in Appendix Figure 11. The micelle sizes in pure water, mixture solvents with ratio of 1:9 and 1:1 are centred at 30, 25 and 50nm respectively, which indicates that the polymers in 1:1 mixture solvent form more loose micelles structure than in the other two systems. The micelle with loose structure cannot be a good template because the ultra-small nanocrystals can penetrate into the micelle instead of around it. The zeta potentials of these micelles are all slightly negative.

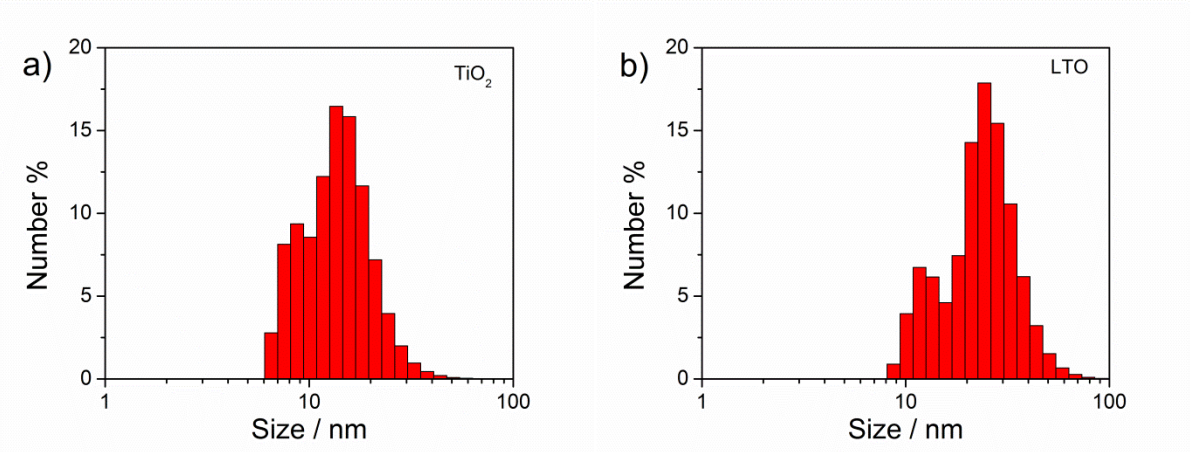

Figure 5.11 DLS measurements of TiO_2 nanocrystals and LTO nanocrystals.

The particles sizes and zeta potentials of TiO_2 and LTO nanocrystals were investigated as well. TiO_2 and LTO nanocrystals possess similar size distribution (seeing Figure 5.11) but quite different zeta potentials. The size distributions are centred at 8 and 16 nm for TiO_2 nanocrystals and 11 and 22 nm for LTO nanocrystals. The zeta potentials of LTO and TiO_2 nanocrystals are −60 and 40 mV, respectively. The pH value of TiO_2 dispersion is 1 while 11 for LTO dispersion. The acidic property of TiO_2 dispersion is stemmed from the further hydrolysis of Ti−Cl group on the surface to form H^+, while the basic property for LTO dispersion is from OH^- produced by the further hydrolysis of Ti−OBn or Li−OBn. As the zeta potential of TiO_2 is opposite with diblock copolymer micelle, the self-assembly between TiO_2 nanocrystals and micelles can be facilitated by the electrostatic attraction. The opposite situation occurs in the LTO case.

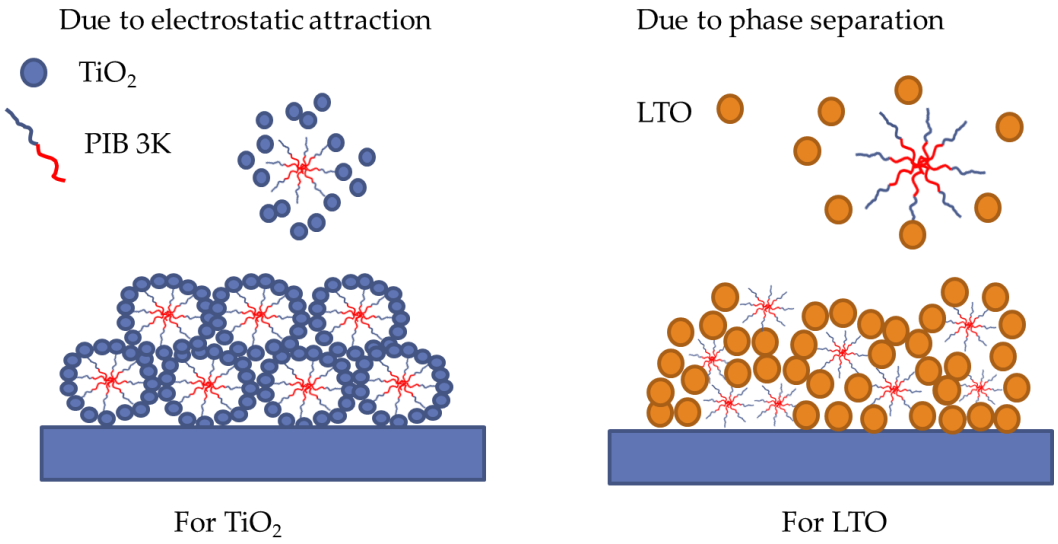

Figure 5.12 Illustration of mesoporous pore formation in TiO_2 and LTO system.

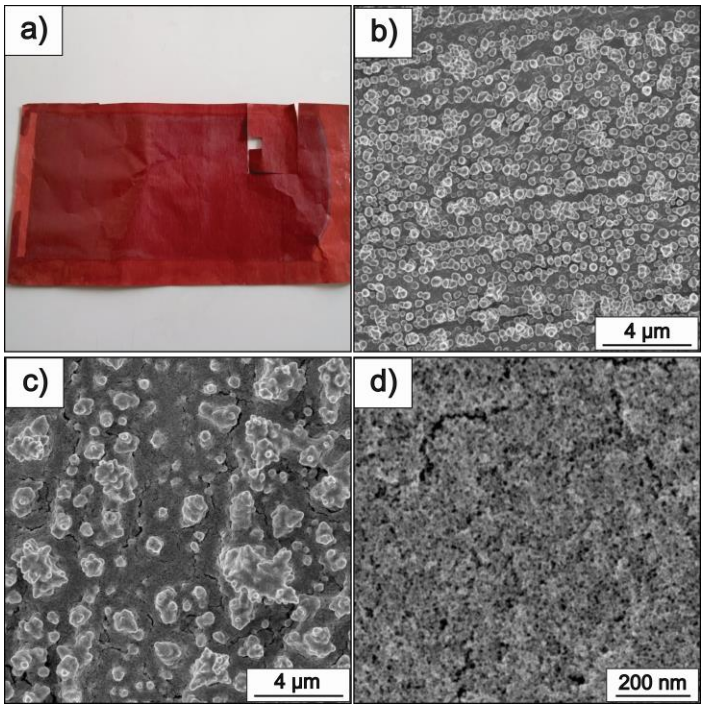

Figure 5.13 Morphology of mesoporous LTO film on copper substrate. (a) Digital picture indicating the coating area of 18×8 cm^2. SEM images of uncoated (b) and coated (c) copper substrate. (d) High resolution SEM image of mesoporous LTO film on copper substrate.

In summary, the ordered mesoporous structure in TiO_2 film is stemmed from the self-assembly between small nanocrystals and tense micelles under the assistance of the electrostatic attraction. The mesopores in LTO system are formed by the phase separation of micelles and nanocrystals, which cannot guarantee the uniformed pore size and ordered pore structure.

The large-scaled mesoporous LTO film can be prepared by a doctor blading coating and the morphology of this film is shown in Figure 5.13. To avoid oxidation of copper substrate, the polymer template was removed by UV-radiation instead of calcination. From the SEM image (Figure 5.13d), the mesopores distributed in LTO films on a copper substrate can be observed.

5.3 Preparation of mesoporous LTO fibers based on nanocrystals

Electrospinning is a classic method to prepare nanofibers. There were some reports about electrospun LTO nanofibers from a sol-gel process according to the literature, but porous LTO fibers and LTO composite fibers were not reported yet.[191-195] Herein the porous LTO and LTO/rGO (reduced graphene oxide referred to as rGO) fibers can be prepared by electrospinning the freshly-prepared LTO nanocrystals with structure directing polymers of PEO 1000K. The detailed preparation information is following: 40 mg PEO 1000K were added to and totally dissolved in 1 mL LTO dispersion (in water) containing 25 mg LTO

nanocrystals. For the LTO/rGO composite fiber, the solvent was replaced by 1mL 0.1 wt% graphene dispersion in water. For both samples, the electrospinning was carried out at room temperature with a voltage of 1 kV/cm and a pump rate of 0.3 mL/h. After electrospinning, the as-made fibers were subjected to 500 $^{\circ}$C for 1 hour under Ar flow of 50 SCCM. After cooling down, the fibers were obtained.

5.3.1 Morphology of LTO fibers

The morphology of LTO fibers after the calcination to remove polymers are shown in Figure 5.14. The morphology of electrospun LTO can be easily tuned from porous spheres, to needles and fibers by increasing the concentration of structure directing polymers. Increasing polymer concentration can increase the viscosity of electrospinning solution, which leads to the fiber morphology. The pores can be clearly observed in these spheres, needles and fibers, which are stemmed from the phase separation process of nanocrystals and PEO polymers. The polymer not only plays the role of generating the fiber morphology but also is of great importance for pore formation. Phase separation phenomenon between organic polymers and inorganic salts is normally observed in the preparation of monolith materials such as SiO_2 and TiO_2.[196-199] Claas *et al*. had studied in detail the phase separation of nanocrystals and polymers in a mixed solution of polar and nonpolar solvents.[200] But it is the first time to report phase separation process in a single-solvent system to form mesopores. As mentioned above, LTO nanocrystals are negatively charged and have no attractive force with PEO; therefore it is easy to form two phases. From Figure 5.14 (c) to (e), the crack or collapse of fibers after the removal of polymers can be avoided by increasing the concentration of nanocrystals. The optimized solution composition for preparing LTO fibers is 40 mg PEO 1000 K polymer and 35 mg LTO nanocrystals in 1 mL water.

As mentioned in Chapter 1, the electronic conductivity of LTO is quite low and the doping has been introduced to increase its intrinsic conductivity in Chapter 3. Here the attention will be paid on designing a mixed nanostructure between LTO nanocrystals and conductive agents.[191, 195] The composite LTO fiber with conductive agents such as reduced graphene oxides (rGO) can be obtained by electrospinning the mixed solution of rGO and LTO dispersion. The morphology of 10 wt% LTO/rGO fibers is shown in Figure 5.14f. The diameters of LTO fibers and composite fibers are both around 220 nm and mesopores with a size of 20 nm are clearly observed in the fibers.

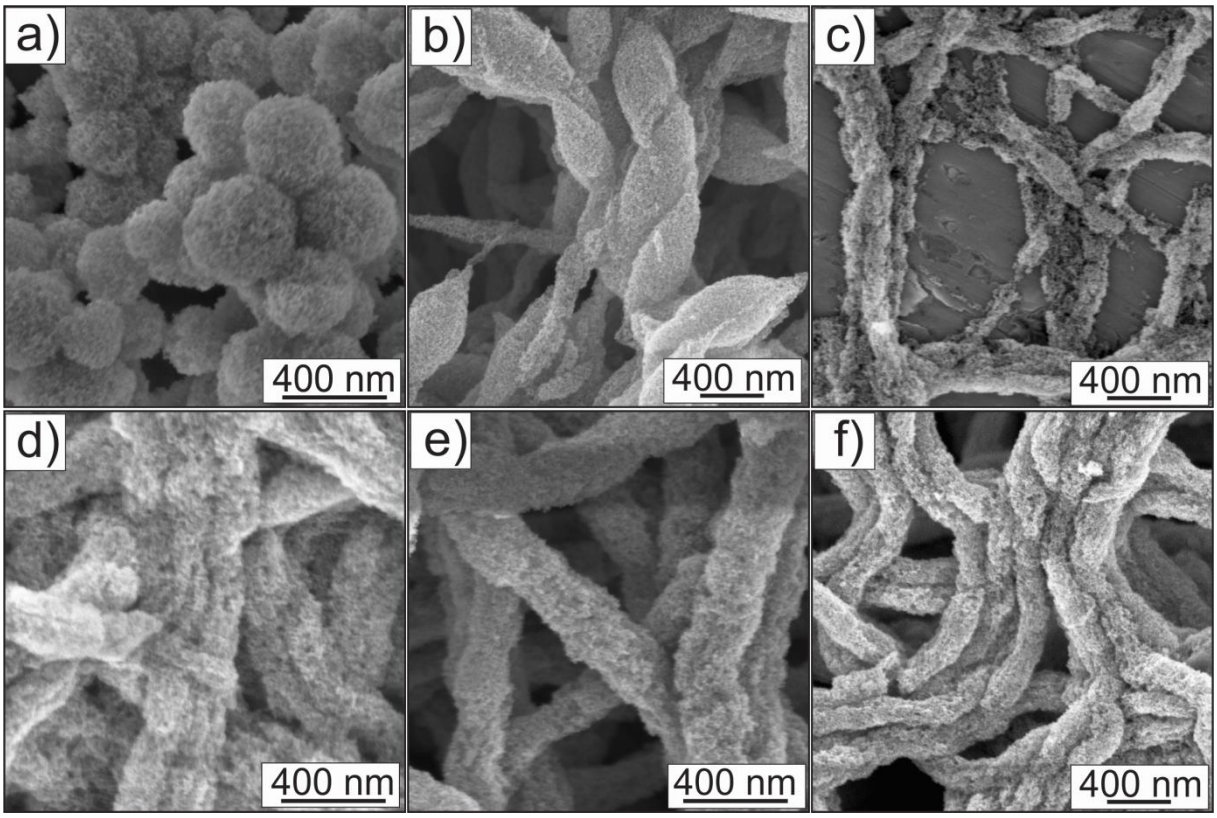

Figure 5.14 SEM images of LTO fibers obtained at different conditions, from (a) to (c), the concentration of PEO 1000 K increasing from 30, 35 to 40 mg/mL while the concentration of LTO nanocrystals are constant to 25 mg/mL; from (c) to (e), the concentration of LTO nanocrystals increasing from 25, 30 to 35 mg/mL with the concentration of PEO 1000K of 40 mg/mL; (f) LTO/rGO composite fibers obtained at the same condition with (e).

To investigate the porosity in these fibers, N_2 physisorption measurement at 77K was carried out and the results are showed on Figure 5.15. The pore size distribution obtained from the adsorption branch based on NLDFT theory and the results are shown in Figure 5.15b. Both materials present similar mesoporous structure and the average pore sizes are around 10 and 9 nm for LTO and LTO/rGO fibers, respectively. This implies the rGO has little effect on the pore structure. The BET surface area are 240 and 270 m^2/g for LTO and LTO/rGO fibers respectively and the higher specific surface area of LTO/rGO fiber may be caused by the existence of reduced graphene oxides.

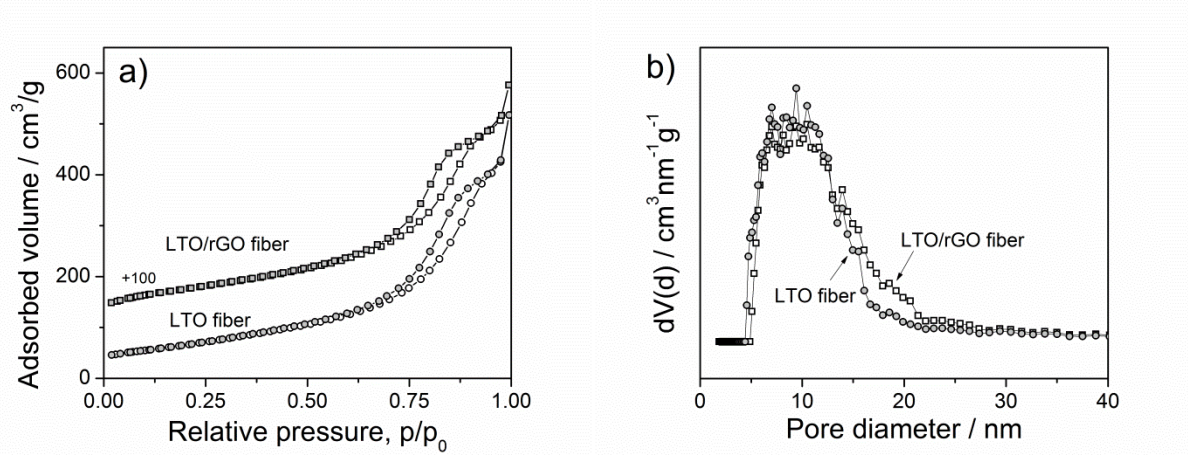

Figure 5.15 (a) N_2 physisorption isotherms of LTO and LTO/rGO fibers and (b) corresponding pore size distributions. Circles are for LTO fibers and squares are for LTO/rGO fibers.

5.3.2 Phase structure of LTO and LTO/rGO fibers

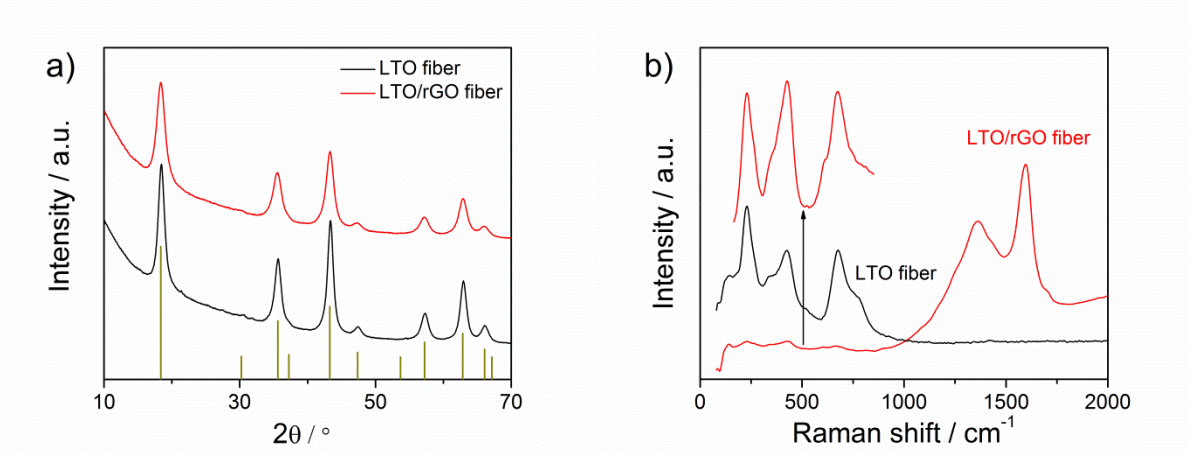

Figure 5.16 Crystalline phases of LTO fibers. (a) XRD patterns of LTO and LTO/rGO fibers, the vertical lines stand for the standard data from JCPDS card 26-1198. (b) Raman spectra of LTO and LTO/rGO fibers. Black curve is for LTO fibers and red curve is for LTO/rGO.

The XRD patterns of LTO and LTO/rGO fibers are shown in Figure 5.16. The XRD patterns are in good agreement with characteristic spinel LTO compared with JCPDS card 26-1198. The crystalline sizes from Scherrer equation are 5.0 and 5.6 nm for LTO/rGO and LTO fibers, nearly the same with pure LTO nanocrystals. The Raman spectra of LTO and LTO/rGO fibers are shown in Figure 5.17b, and the results indicate that the crystalline structure of LTO fibers remains pure spinel phase, identical with pure nanocrystals. Two strong Raman peaks in LTO/rGO fibers located at 1364 and 1594 cm^{-1} can be ascribed to the D band and G band of carbon, which confirms the existence of rGO.[201] The rGO content was measured by TGA and the results indicate 13 wt% rGO.

5.3.3 Electrochemical performance of LTO fibers

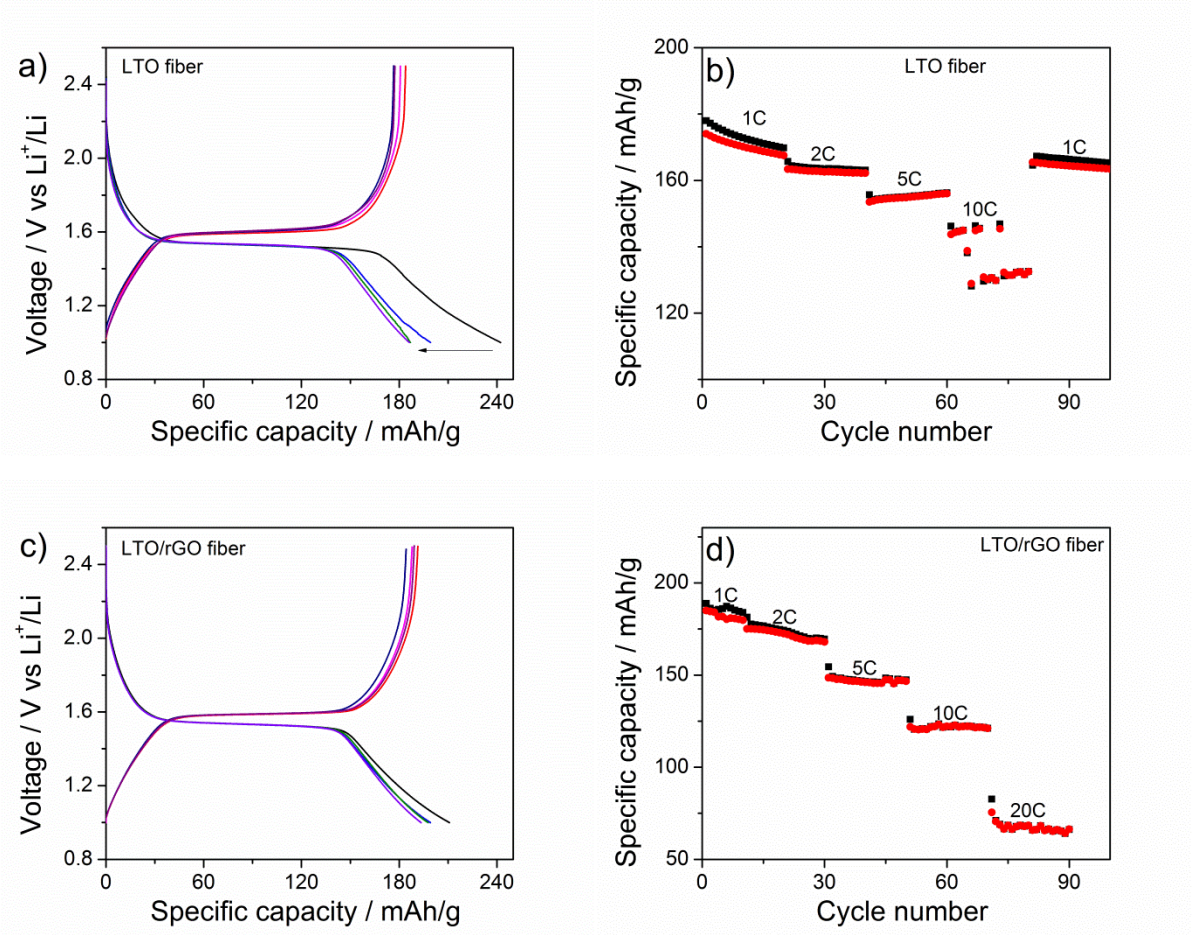

Figure 5.18 Electrochemical performance of LTO and LTO/rGO fibers. (a) Galvanostatic discharge/charge curves at C/2 and (b) rate capacity of LTO fibers. (c) Galvanostatic discharge/charge curves at C/2 and (d) rate capacity of LTO/rGO fibers. 1C=175 mAh/g.

The electrochemical properties of LTO fibers and LTO/rGO fibers are evaluated by galvanostatic discharge and charge curves, and the results are shown in Figure 5.18. For both materials, the discharge plateau potentials are both around 1.55 V vs Li^+/Li, which is perfectly matched with the previous reports. The specific capacities of both materials at a discharge and charge rate of 10C are around 130 mAh/g. Compared with LTO nanocrystals showed in Chapter 4, the morphology of mesoporous fiber does not improve the electrochemical performance. Adding rGO does not improve the rate capacity, and the reason may be the grafted graphene (more than10 wt%) hindering the diffusion of Li^+ ion.

5.4 Summary

Although mesoporous LTO powders were successfully prepared by a polymer-templated sol-gel process, the preparation condition is quite strict and the electrochemical performance is not comparable with nanocrystals on account of the differences in crystallite sizes and specific surface area. In order to investigate the impacts of porosity on the electrochemical performance, the nanocrystals were used as building blocks to construct porous systems with different pore size but similar crystallite sizes and specific surface area. The results indicate that macroporous system can improve the rate capacity (160C). Further the LTO and LTO/rGO fibers have been studied. The mesoporous LTO fiber presents similar electrochemical properties with LTO nanocrystals. Compared with nanocrystals, the mesoporous system and fiber morphology scarcely improve the electrochemical performance. At last the formation mechanism of mesopores in different systems was investigated. The results showed that the co-assembly between TiO_2 nanocrystals and polymer micelles is mainly attributable to the electrostatic attraction. In case of LTO, LTO nanocrystals and micelles are just randomly packing.

CHAPTER 6
CONCLUSIONS AND OUTLOOKS

The titanium-based nanomaterials including anatase TiO_2 and spinel LTO with crystallite size less than 10 nm were prepared by a non-aqueous approach. The main focuses are the impacts of the crystallite size and doping on the crystalline structure and electrochemical performance. These nanocrystals were used as building blocks to generate mesoporous and macroporous films, and the pore size effect on electrochemistry was investigated as well.

Anatase TiO_2 and doped TiO_2 nanocrystals were prepared by a novel non-aqueous approach based on *tert*-amyl alcohol and a primary alcohol (1-hexanol, 1-decanol etc.) was introduced into this system in order to improve the crystallinity. After Nb^{5+} incorporated with anatase lattice, the vacancies of Ti^{4+} were created. When Nb content increases to 5 at%, reduced Ti^{4+} was found. The 5 at% Nb:TiO_2 presents the best conductivity and the best electrochemical performance as anode material for LIBs. The pseudocapacitive effect in mesoporous Nb:TiO_2 films was investigated and the results indicated that the pseudocapacitive contribution is conductivity-dependent.

LTO nanocrystals were prepared based on a benzyl alcohol route and the effects of the reaction parameters including reaction temperature, precursors and concentration on the products were studied in detail. The results showed that the crystallite size can increase to certain extent with the increase of reaction temperature. When the reaction temperature is as high as 250 °C, the nanocrystals aggregate into big mesocrystals attributable to the benzoate on the surface. The GC-MS data indicated that the reaction mainly undergoes the similar Meerwein-Ponndorf-Verley reaction to form the toluene and benzaldehyde. Two different aliovalent ions of Nb^{5+} and Al^{3+} were used to substitute Ti^{4+} ions in LTO. The results indicated that the Nb^{5+} were located at 16*d* sites in the TiO_6 octahedron as expected but Al^{3+} ions tend to substitute Li^+ ions in 8*a* in the LiO_4 tetrahedron. After doping the conductivity of LTO gets improved. The specific capacity of Al:LTO and Nb:LTO are smaller than the one of LTO nanocrystals, which may be attributable to the substitution of Li^+ ions in 8*a* site in case of Al:LTO and Li^+ ions vacancies in case of Nb:LTO.

Mesoporous LTO powder can be obtained from sol-gel process under the strictly controlled heat treatment. However the performance of mesoporous LTO powder is not comparable than LTO nanocrystals we prepared. This can be assigned to the low specific surface area and the big crystallite size of mesoporous LTO powder. In order to assess the pore effect on electrochemistry, the LTO nanocrystals were used as building blocks to construct mesoporous

and macroporous films, which can guarantee the comparable specific surface area of the films and the similar crystallite size of active materials. The electrochemical results from mesoporous and macroporous films indicated that the macroporous LTO films present the best rate capacity at 160C.

LITERATURE

1. Yoshino, A., The Birth of the Lithium-Ion Battery. *Angewandte Chemie-International Edition* **2012,** 51, (24), 5798-5800.
2. Tarascon, J. M.; Armand, M., Issues and challenges facing rechargeable lithium batteries. *Nature* **2001,** 414, (6861), 359-367.
3. Vetter, J.; Novak, P.; Wagner, M. R.; Veit, C.; Moller, K. C.; Besenhard, J. O.; Winter, M.; Wohlfahrt-Mehrens, M.; Vogler, C.; Hammouche, A., Ageing mechanisms in lithium-ion batteries. *Journal of Power Sources* **2005,** 147, (1-2), 269-281.
4. Etacheri, V.; Marom, R.; Elazari, R.; Salitra, G.; Aurbach, D., Challenges in the development of advanced Li-ion batteries: a review. *Energy & Environmental Science* **2011,** 4, (9), 3243-3262.
5. Aurbach, D.; Markovsky, B.; Weissman, I.; Levi, E.; Ein-Eli, Y., On the correlation between surface chemistry and performance of graphite negative electrodes for Li ion batteries. *Electrochimica Acta* **1999,** 45, (1-2), 67-86.
6. Zhang, W.-J., A review of the electrochemical performance of alloy anodes for lithium-ion batteries. *Journal of Power Sources* **2011,** 196, (1), 13-24.
7. Liu, X. H.; Liu, Y.; Kushima, A.; Zhang, S.; Zhu, T.; Li, J.; Huang, J. Y., In Situ TEM Experiments of Electrochemical Lithiation and Delithiation of Individual Nanostructures. *Advanced Energy Materials* **2012,** 2, (7), 722-741.
8. Key, B.; Bhattacharyya, R.; Morcrette, M.; Seznec, V.; Tarascon, J.-M.; Grey, C. P., Real-Time NMR Investigations of Structural Changes in Silicon Electrodes for Lithium-Ion Batteries. *Journal of the American Chemical Society* **2009,** 131, (26), 9239-9249.
9. Huang, J. Y.; Zhong, L.; Wang, C. M.; Sullivan, J. P.; Xu, W.; Zhang, L. Q.; Mao, S. X.; Hudak, N. S.; Liu, X. H.; Subramanian, A., In situ observation of the electrochemical lithiation of a single SnO_2 nanowire electrode. *Science* **2010,** 330, (6010), 1515-1520.
10. Gao, X. P.; Bao, J. L.; Pan, G. L.; Zhu, H. Y.; Huang, P. X.; Wu, F.; Song, D. Y., Preparation and electrochemical performance of polycrystalline and single crystalline CuO nanorods as anode materials for Li ion battery. *Journal of Physical Chemistry B* **2004,** 108, (18), 5547-5551.
11. Grugeon, S.; Laruelle, S.; Herrera-Urbina, R.; Dupont, L.; Poizot, P.; Tarascon, J. M., Particle size effects on the electrochemical performance of copper oxides toward lithium. *Journal of the Electrochemical Society* **2001,** 148, (4), A285-A292.
12. Li, Y.; Tan, B.; Wu, Y., Mesoporous Co_3O_4 nanowire arrays for lithium ion batteries with high capacity and rate capability. *Nano Letters* **2008,** 8, (1), 265-270.
13. Wang, Z.; Zhou, L.; Lou, X. W., Metal Oxide Hollow Nanostructures for Lithium-ion Batteries. *Advanced Materials* **2012,** 24, (14), 1903-1911.
14. Zhou, G.; Wang, D.-W.; Li, F.; Zhang, L.; Li, N.; Wu, Z.-S.; Wen, L.; Lu, G. Q.; Cheng, H.-M., Graphene-Wrapped Fe_3O_4 Anode Material with Improved Reversible Capacity and Cyclic Stability for Lithium Ion Batteries. *Chemistry of Materials* **2010,** 22, (18), 5306-5313.
15. Wu, H. B.; Chen, J. S.; Hng, H. H.; Lou, X. W., Nanostructured metal oxide-based materials as advanced anodes for lithium-ion batteries. *Nanoscale* **2012,** 4, (8), 2526-2542.
16. Wang, F.; Yu, H.-C.; Chen, M.-H.; Wu, L.; Pereira, N.; Thornton, K.; Van der Ven, A.; Zhu, Y.; Amatucci, G. G.; Graetz, J., Tracking lithium transport and electrochemical reactions in nanoparticles. *Nature Communication* **2012,** 3, 1201.
17. Armstrong, M. J.; Panneerselvam, A.; O'Regan, C.; Morris, M. A.; Holmes, J. D., Supercritical-fluid synthesis of FeF_2 and CoF_2 Li-ion conversion materials. *Journal of Materials Chemistry A* **2013,** 1, (36), 10667-10676.
18. Wen, X.; Wei, X.; Yang, L.; Shen, P. K., Self-assembled FeS_2 cubes anchored on reduced graphene oxide as an anode material for lithium ion batteries. *Journal of Materials Chemistry A* **2015,** 3, (5), 2090-2096.
19. Chen, Z. H.; Belharouak, I.; Sun, Y. K.; Amine, K., Titanium-Based Anode Materials for Safe Lithium-Ion Batteries. *Advanced Functional Materials* **2013,** 23, (8), 959-969.
20. Zhu, G.-N.; Wang, Y.-G.; Xia, Y.-Y., Ti-based compounds as anode materials for Li-ion batteries. *Energy & Environmental Science* **2012,** 5, (5), 6652-6667.

21. Milne, N. A.; Skyllas-Kazacos, M.; Luca, V., Crystallite Size Dependence of Lithium Intercalation in Nanocrystalline Rutile. *Journal of Physical Chemistry C* **2009,** 113, (30), 12983-12995.
22. Armstrong, A. R.; Armstrong, G.; Canales, J.; Garcia, R.; Bruce, P. G., Lithium-ion intercalation into TiO_2-B nanowires. *Advanced Materials* **2005,** 17, (7), 862-865.
23. Gao, Q.; Gu, M.; Nie, A.; Mashayek, F.; Wang, C.; Odegard, G. M.; Shahbazian-Yassar, R., Direct Evidence of Lithium-Induced Atomic Ordering in Amorphous TiO_2 Nanotubes. *Chemistry of Materials* **2014,** 26, (4), 1660-1669.
24. Ferg, E.; Gummow, R. J.; de Kock, A.; Thackeray, M. M., Spinel Anodes for Lithium-Ion Batteries. *Journal of The Electrochemical Society* **1994,** 141, (11), L147-L150.
25. Ouyang, C. Y.; Zhong, Z. Y.; Lei, M. S., Ab initio studies of structural and electronic properties of $Li_4Ti_5O_{12}$ spinel. *Electrochemistry Communications* **2007,** 9, (5), 1107-1112.
26. Borghols, W. J. H.; Wagemaker, M.; Lafont, U.; Kelder, E. M.; Mulder, F. M., Size Effects in the $Li_{4+x}Ti_5O_{12}$ Spinel. *Journal of the American Chemical Society* **2009,** 131, (49), 17786-17792.
27. Ohzuku, T.; Ueda, A.; Yamamoto, N., Zero-Strain Insertion Material Of $Li[Li_{1/3}Ti_{5/3}]O_4$ For Rechargeable Lithium Cells. *Journal of the Electrochemical Society* **1995,** 142, (5), 1431-1435.
28. Chen, J. S.; Tan, Y. L.; Li, C. M.; Cheah, Y. L.; Luan, D.; Madhavi, S.; Boey, F. Y. C.; Archer, L. A.; Lou, X. W., Constructing Hierarchical Spheres from Large Ultrathin Anatase TiO_2 Nanosheets with Nearly 100% Exposed (001) Facets for Fast Reversible Lithium Storage. *Journal of the American Chemical Society* **2010,** 132, (17), 6124-6130.
29. Kavan, L.; Grätzel, M.; Rathouský, J.; Zukalb, A., Nanocrystalline TiO_2 (Anatase) Electrodes: Surface Morphology, Adsorption, and Electrochemical Properties. *Journal of The Electrochemical Society* **1996,** 143, (2), 394-400.
30. Lindström, H.; Södergren, S.; Solbrand, A.; Rensmo, H.; Hjelm, J.; Hagfeldt, A.; Lindquist, S.-E., Li^+ Ion Insertion in TiO_2 (Anatase). 2. Voltammetry on Nanoporous Films. *The Journal of Physical Chemistry B* **1997,** 101, (39), 7717-7722.
31. Ohzuku, T.; Kodama, T.; Hirai, T., Electrochemistry of anatase titanium dioxide in lithium nonaqueous cells. *Journal of Power Sources* **1985,** 14, (1–3), 153-166.
32. Wagemaker, M.; Kearley, G. J.; van Well, A. A.; Mutka, H.; Mulder, F. M., Multiple Li Positions inside Oxygen Octahedra in Lithiated TiO_2 Anatase. *Journal of the American Chemical Society* **2003,** 125, (3), 840-848.
33. Bruce, P. G.; Scrosati, B.; Tarascon, J.-M., Nanomaterials for rechargeable lithium batteries. *Angewandte Chemie-International Edition* **2008,** 47, (16), 2930-2946.
34. Jamnik, J.; Maier, J., Nanocrystallinity effects in lithium battery materials - Aspects of nano-ionics. Part IV. *Physical Chemistry Chemical Physics* **2003,** 5, (23), 5215-5220.
35. Wagemaker, M.; Borghols, W. J. H.; Mulder, F. M., Large impact of particle size on insertion reactions. A case for anatase Li_xTiO_2. *Journal of the American Chemical Society* **2007,** 129, (14), 4323-4327.
36. Zhu, K.; Wang, Q.; Kim, J.-H.; Pesaran, A. A.; Frank, A. J., Pseudocapacitive Lithium-Ion Storage in Oriented Anatase TiO_2 Nanotube Arrays. *The Journal of Physical Chemistry C* **2012,** 116, (22), 11895-11899.
37. Yu, P.; Li, C.; Guo, X., Sodium Storage and Pseudocapacitive Charge in Textured $Li_4Ti_5O_{12}$ Thin Films. *The Journal of Physical Chemistry C* **2014,** 118, (20), 10616-10624.
38. Conway, B. E.; Birss, V.; Wojtowicz, J., The role and utilization of pseudocapacitance for energy storage by supercapacitors. *Journal of Power Sources* **1997,** 66, (1–2), 1-14.
39. Brezesinski, K.; Wang, J.; Haetge, J.; Reitz, C.; Steinmueller, S. O.; Tolbert, S. H.; Smarsly, B. M.; Dunn, B.; Brezesinski, T., Pseudocapacitive Contributions to Charge Storage in Highly Ordered Mesoporous Group V Transition Metal Oxides with Iso-Oriented Layered Nanocrystalline Domains. *Journal of the American Chemical Society* **2010,** 132, (20), 6982-6990.
40. Augustyn, V.; Come, J.; Lowe, M. A.; Kim, J. W.; Taberna, P.-L.; Tolbert, S. H.; Abruna, H. D.; Simon, P.; Dunn, B., High-rate electrochemical energy storage through Li^+ intercalation pseudocapacitance. *Nature Materials* **2013,** 12, (6), 518-522.
41. Brezesinski, T.; Wang, J.; Tolbert, S. H.; Dunn, B., Ordered mesoporous alpha-MoO_3 with iso-oriented nanocrystalline walls for thin-film pseudocapacitors. *Nature Materials* **2010,** 9, (2), 146-151.

42. Muller, G. A.; Cook, J. B.; Kim, H. S.; Tolbert, S. H.; Dunn, B., High Performance Pseudocapacitor Based on 2D Layered Metal Chalcogenide Nanocrystals. *Nano Letters* **2015,** 15, (3), 1911-1917.
43. Brezesinski, T.; Wang, J.; Polleux, J.; Dunn, B.; Tolbert, S. H., Templated Nanocrystal-Based Porous TiO_2 Films for Next-Generation Electrochemical Capacitors. *Journal of the American Chemical Society* **2009,** 131, (5), 1802-1809.
44. Rauda, I. E.; Augustyn, V.; Dunn, B.; Tolbert, S. H., Enhancing Pseudocapacitive Charge Storage in Polymer Templated Mesoporous Materials. *Accounts of Chemical Research* **2013,** 46, (5), 1113-1124.
45. Kim, J. W.; Augustyn, V.; Dunn, B., The Effect of Crystallinity on the Rapid Pseudocapacitive Response of Nb_2O_5. *Advanced Energy Materials* **2012,** 2, (1), 141-148.
46. Wagemaker, M.; Mulder, F. M., Properties and Promises of Nanosized Insertion Materials for Li-Ion Batteries. *Accounts of Chemical Research* **2013,** 46, (5), 1206-1215.
47. Wang, J.; Polleux, J.; Lim, J.; Dunn, B., Pseudocapacitive Contributions to Electrochemical Energy Storage in TiO_2 (Anatase) Nanoparticles. *The Journal of Physical Chemistry C* **2007,** 111, (40), 14925-14931.
48. Opitz, M.; Yue, J.; Wallauer, J.; Smarsly, B.; Roling, B., Mechanisms of Charge Storage in Nanoparticulate TiO_2 and $Li_4Ti_5O_{12}$ Anodes: New Insights from Scan rate-dependent Cyclic Voltammetry. *Electrochimica Acta* **2015,** 168, 125-132.
49. Yao, X. L.; Xie, S.; Chen, C. H.; Wang, Q. S.; Sun, J. H.; Li, Y. L.; Lu, S. X., Comparisons of graphite and spinel $Li_{1.33}Ti_{1.67}O_4$ as anode materials for rechargeable lithium-ion batteries. *Electrochimica Acta* **2005,** 50, (20), 4076-4081.
50. Reale, P.; Panero, S.; Ronci, F.; Rossi Albertini, V.; Scrosati, B., Iron-Substituted Lithium Titanium Spinels: Structural and Electrochemical Characterization. *Chemistry of Materials* **2003,** 15, (18), 3437-3442.
51. Capsoni, D.; Bini, M.; Massarotti, V.; Mustarelli, P.; Chiodelli, G.; Azzoni, C. B.; Mozzati, M. C.; Linati, L.; Ferrari, S., Cations Distribution and Valence States in Mn-Substituted $Li_4Ti_5O_{12}$ Structure. *Chemistry of Materials* **2008,** 20, (13), 4291-4298.
52. Jung, H.-G.; Myung, S.-T.; Yoon, C. S.; Son, S.-B.; Oh, K. H.; Amine, K.; Scrosati, B.; Sun, Y.-K., Microscale spherical carbon-coated $Li_4Ti_5O_{12}$ as ultra high power anode material for lithium batteries. *Energy & Environmental Science* **2011,** 4, (4), 1345-1351.
53. Wang, C.; Wang, S.; He, Y.-B.; Tang, L.; Han, C.; Yang, C.; Wagemaker, M.; Li, B.; Yang, Q.-H.; Kim, J.-K.; Kang, F., Combining Fast Li-Ion Battery Cycling with Large Volumetric Energy Density: Grain Boundary Induced High Electronic and Ionic Conductivity in $Li_4Ti_5O_{12}$ Spheres of Densely Packed Nanocrystallites. *Chemistry of Materials* **2015,** 27, (16), 5647-5656.
54. Xia, C.; Nian, C.; Huang, Z.; Lin, Y.; Wang, D.; Zhang, C., One-step synthesis of carbon-coated $Li_4Ti_{4.95}Nd_{0.05}O_{12}$ by modified citric acid sol-gel method for lithium-ion battery. *Journal of Sol-Gel Science and Technology* **2015,** 75, (1), 38-44.
55. Lee, S. C.; Lee, S. M.; Lee, J. W.; Lee, J. B.; Lee, S. M.; Han, S. S.; Lee, H. C.; Kim, H. J., Spinel $Li_4Ti_5O_{12}$ Nanotubes for Energy Storage Materials. *The Journal of Physical Chemistry C* **2009,** 113, (42), 18420-18423.
56. Chen, J.; Yang, L.; Fang, S.; Hirano, S.-i.; Tachibana, K., Synthesis of hierarchical mesoporous nest-like $Li_4Ti_5O_{12}$ for high-rate lithium ion batteries. *Journal of Power Sources* **2012,** 200, 59-66.
57. Shen, L.; Yuan, C.; Luo, H.; Zhang, X.; Xu, K.; Xia, Y., Facile synthesis of hierarchically porous $Li_4Ti_5O_{12}$ microspheres for high rate lithium ion batteries. *Journal of Materials Chemistry* **2010,** 20, (33), 6998-7004.
58. Li, Z. Y.; Li, J. L.; Zhao, Y. G.; Yang, K.; Gao, F.; Li, X. Structure and electrochemical properties of Sm-doped $Li_4Ti_5O_{12}$ as anode material for lithium-ion batteries. *RSC Advance* **2016**, 6, 15492-15500.
59. Bresser, D.; Paillard, E.; Copley, M.; Bishop, P.; Winter, M.; Passerini, S., The importance of "going nano" for high power battery materials. *Journal of Power Sources* **2012,** 219, 217-222.
60. Shen, Y.; Eltzholtz, J. R.; Iversen, B. B., Controlling Size, Crystallinity, and Electrochemical Performance of $Li_4Ti_5O_{12}$ Nanocrystals. *Chemistry of Materials* **2013,** 25, (24), 5023-5030.

61. Niederberger, M.; Bartl, M. H.; Stucky, G. D., Benzyl Alcohol and Titanium TetrachlorideA Versatile Reaction System for the Nonaqueous and Low-Temperature Preparation of Crystalline and Luminescent Titania Nanoparticles. *Chemistry of Materials* **2002,** 14, (10), 4364-4370.
62. Niederberger, M., Nonaqueous sol-gel routes to metal oxide nanoparticles. *Accounts of Chemical Research* **2007,** 40, (9), 793-800.
63. Pinna, N.; Niederberger, M., Surfactant-free nonaqueous synthesis of metal oxide nanostructures. *Angewandte Chemie-International Edition* **2008,** 47, (29), 5292-5304.
64. Stefik, M.; Heiligtag, F. J.; Niederberger, M.; Graetzel, M., Improved Nonaqueous Synthesis of TiO_2 for Dye-Sensitized Solar Cells. *Acs Nano* **2013,** 7, (10), 8981-8989.
65. Yu, S.-H.; Pucci, A.; Herntrich, T.; Willinger, M.-G.; Baek, S.-H.; Sung, Y.-E.; Pinna, N., Surfactant-free nonaqueous synthesis of lithium titanium oxide (LTO) nanostructures for lithium ion battery applications. *Journal of Materials Chemistry* **2011,** 21, (3), 806-810.
66. Liu, Y.; Szeifert, J. M.; Feckl, J. M.; Mandlmeier, B.; Rathousky, J.; Hayden, O.; Fattakhova-Rohlfing, D.; Bein, T., Niobium-Doped Titania Nanoparticles: Synthesis and Assembly into Mesoporous Films and Electrical Conductivity. *ACS Nano* **2010,** 4, (9), 5373-5381.
67. Fominykh, K.; Chernev, P.; Zaharieva, I.; Sicklinger, J.; Stefanic, G.; Döblinger, M.; Müller, A.; Pokharel, A.; Böcklein, S.; Scheu, C.; Bein, T.; Fattakhova-Rohlfing, D., Iron-Doped Nickel Oxide Nanocrystals as Highly Efficient Electrocatalysts for Alkaline Water Splitting. *ACS Nano* **2015,** 9, (5), 5180-5188.
68. Fominykh, K.; Feckl, J. M.; Sicklinger, J.; Döblinger, M.; Böcklein, S.; Ziegler, J.; Peter, L.; Rathousky, J.; Scheidt, E.-W.; Bein, T.; Fattakhova-Rohlfing, D., Ultrasmall Dispersible Crystalline Nickel Oxide Nanoparticles as High-Performance Catalysts for Electrochemical Water Splitting. *Advanced Functional Materials* **2014,** 24, (21), 3123-3129.
69. Feckl, J. M.; Fominykh, K.; Döblinger, M.; Fattakhova-Rohlfing, D.; Bein, T., Nanoscale Porous Framework of Lithium Titanate for Ultrafast Lithium Insertion. *Angewandte Chemie International Edition* **2012,** 51, (30), 7459-7463.
70. Hoffmann, F.; Cornelius, M.; Morell, J.; Froeba, M., Silica-based mesoporous organic-inorganic hybrid materials. *Angewandte Chemie-International Edition* **2006,** 45, (20), 3216-3251.
71. Taguchi, A.; Schuth, F., Ordered mesoporous materials in catalysis. *Microporous and Mesoporous Materials* **2005,** 77, (1), 1-45.
72. Ferey, G., Microporous solids: From organically templated inorganic skeletons to hybrid frameworks ... ecumenism in chemistry. *Chemistry of Materials* **2001,** 13, (10), 3084-3098.
73. Wang, Y.; Angelatos, A. S.; Caruso, F., Template synthesis of nanostructured materials via layer-by-layer assembly. *Chemistry of Materials* **2008,** 20, (3), 848-858.
74. Stein, A.; Schroden, R. C., Colloidal crystal templating of three-dimensionally ordered macroporous solids: materials for photonics and beyond. *Current Opinion in Solid State & Materials Science* **2001,** 5, (6), 553-564.
75. Studart, A. R.; Gonzenbach, U. T.; Tervoort, E.; Gauckler, L. J., Processing routes to macroporous ceramics: A review. *Journal of the American Ceramic Society* **2006,** 89, (6), 1771-1789.
76. Yue, J.; Suchomski, C.; Brezesinski, T.; Smarsly, B. M., Polymer-Templated Mesoporous $Li_4Ti_5O_{12}$ as a High-Rate and Long-Life Anode Material for Rechargeable Li-Ion Batteries. *ChemNanoMat* **2015,** 1, (6), 415-421.
77. Haetge, J.; Hartmann, P.; Brezesinski, K.; Janek, J.; Brezesinski, T., Ordered Large-Pore Mesoporous $Li_4Ti_5O_{12}$ Spinel Thin Film Electrodes with Nanocrystalline Framework for High Rate Rechargeable Lithium Batteries: Relationships among Charge Storage, Electrical Conductivity, and Nanoscale Structure. *Chemistry of Materials* **2011,** 23, (19), 4384-4393.
78. Horie, Y.; Daizaka, K.; Mukae, H.; Guo, S. R.; Nomiyama, T. Enhancement of photocurrent by columnar Nb-doped TiO_2 compact layer in dye sensitized solar cells with low temperature process of dc sputtering. *Electrochimica Acta* **2016**, 187, 348-357.
79. Ostermann, R.; Zieba, R.; Rudolph, M.; Schlettwein, D.; Smarsly, B. M., Electrospun antimony doped tin oxide (ATO) nanofibers as a versatile conducting matrix. *Chemical Communications* **2011,** 47, (44), 12119-12121.

80. von Graberg, T.; Hartmann, P.; Rein, A.; Gross, S.; Seelandt, B.; Roeger, C.; Zieba, R.; Traut, A.; Wark, M.; Janek, J.; Smarsly, B. M., Mesoporous tin-doped indium oxide thin films: effect of mesostructure on electrical conductivity. *Science and Technology of Advanced Materials* **2011,** 12, (2).
81. Ueda, K.; Tabata, H.; Kawai, T., Magnetic and electric properties of transition-metal-doped ZnO films. *Applied Physics Letters* **2001,** 79, (7), 988-990.
82. Furubayashi, Y.; Hitosugi, T.; Yamamoto, Y.; Inaba, K.; Kinoda, G.; Hirose, Y.; Shimada, T.; Hasegawa, T., A transparent metal: Nb-doped anatase TiO_2. *Applied Physics Letters* **2005,** 86, (25).
83. De Trizio, L.; Buonsanti, R.; Schimpf, A. M.; Llordes, A.; Gamelin, D. R.; Simonutti, R.; Milliron, D. J., Nb-Doped Colloidal TiO_2 Nanocrystals with Tunable Infrared Absorption. *Chemistry of Materials* **2013,** 25, (16), 3383-3390.
84. Chen, C. H.; Vaughey, J. T.; Jansen, A. N.; Dees, D. W.; Kahaian, A. J.; Goacher, T.; Thackeray, M. M., Studies of Mg-substituted $Li_{4-x}Mg_xTi_5O_{12}$ spinel electrodes (0 <= x <= 1) for lithium batteries. *Journal of the Electrochemical Society* **2001,** 148, (1), A102-A104.
85. Dambournet, D.; Belharouak, I.; Amine, K., $MLi_2Ti_6O_{14}$ (M = Sr, Ba, 2Na) Lithium Insertion Titanate Materials: A Comparative Study. *Inorganic Chemistry* **2010,** 49, (6), 2822-2826.
86. Dambournet, D.; Belharouak, I.; Ma, J.; Amine, K., Template-assisted synthesis of high packing density $SrLi_2Ti_6O_{14}$ for use as anode in 2.7-V lithium-ion battery. *Journal of Power Sources* **2011,** 196, (5), 2871-2874.
87. Wilkening, M.; Amade, R.; Iwaniak, W.; Heitjans, P., Ultraslow Li diffusion in spinel-type structured $Li_4Ti_5O_{12}$-A comparison of results from solid state NMR and impedance spectroscopy. *Physical Chemistry Chemical Physics* **2007,** 9, (10), 1239-1246.
88. Wagemaker, M.; van Eck, E. R. H.; Kentgens, A. P. M.; Mulder, F. M., Li-Ion Diffusion in the Equilibrium Nanomorphology of Spinel $Li_{4+x}Ti_5O_{12}$. *The Journal of Physical Chemistry B* **2009,** 113, (1), 224-230.
89. Song, H.; Yun, S.-W.; Chun, H.-H.; Kim, M.-G.; Chung, K. Y.; Kim, H. S.; Cho, B.-W.; Kim, Y.-T., Anomalous decrease in structural disorder due to charge redistribution in Cr-doped $Li_4Ti_5O_{12}$ negative-electrode materials for high-rate Li-ion batteries. *Energy & Environmental Science* **2012,** 5, (12), 9903-9913.
90. Ma, Y.; Ding, B.; Ji, G.; Lee, J. Y., Carbon-Encapsulated F-Doped $Li_4Ti_5O_{12}$ as a High Rate Anode Material for Li+ Batteries. *ACS Nano* **2013,** 7, (12), 10870-10878.
91. Bai, Y.-J.; Gong, C.; Qi, Y.-X.; Lun, N.; Feng, J., Excellent long-term cycling stability of La-doped $Li_4Ti_5O_{12}$ anode material at high current rates. *Journal of Materials Chemistry* **2012,** 22, (36), 19054-19060.
92. Yi, T.-F.; Shu, J.; Zhu, Y.-R.; Zhu, X.-D.; Yue, C.-B.; Zhou, A.-N.; Zhu, R.-S., High-performance $Li_4Ti_{5-x}V_xO_{12}$ ($0 \leqslant x \leqslant 0.3$) as an anode material for secondary lithium-ion battery. *Electrochimica Acta* **2009,** 54, (28), 7464-7470.
93. Tian, B.; Xiang, H.; Zhang, L.; Li, Z.; Wang, H., Niobium doped lithium titanate as a high rate anode material for Li-ion batteries. *Electrochimica Acta* **2010,** 55, (19), 5453-5458.
94. Park, K.-S.; Benayad, A.; Kang, D.-J.; Doo, S.-G., Nitridation-Driven Conductive $Li_4Ti_5O_{12}$ for Lithium Ion Batteries. *Journal of the American Chemical Society* **2008,** 130, (45), 14930-14931.
95. Li, W.; Wang, F.; Feng, S.; Wang, J.; Sun, Z.; Li, B.; Li, Y.; Yang, J.; Elzatahry, A. A.; Xia, Y.; Zhao, D., Sol-Gel Design Strategy for Ultradispersed TiO_2 Nanoparticles on Graphene for High-Performance Lithium Ion Batteries. *Journal of the American Chemical Society* **2013,** 135, (49), 18300-18303.
96. Zuo, W.; Wang, C.; Li, Y.; Liu, J., Directly Grown Nanostructured Electrodes for High Volumetric Energy Density Binder-Free Hybrid Supercapacitors: A Case Study of CNTs//$Li_4Ti_5O_{12}$. *Scientific Reports* **2015,** 5.
97. Zhang, B.; Liu, Y.; Huang, Z.; Oh, S.; Yu, Y.; Mai, Y.-W.; Kim, J.-K., Urchin-like $Li_4Ti_5O_{12}$-carbon nanofiber composites for high rate performance anodes in Li-ion batteries. *Journal of Materials Chemistry* **2012,** 22, (24), 12133-12140.
98. Naoi, K.; Ishimoto, S.; Isobe, Y.; Aoyagi, S., High-rate nano-crystalline $Li_4Ti_5O_{12}$ attached on carbon nano-fibers for hybrid supercapacitors. *Journal of Power Sources* **2010,** 195, (18), 6250-6254.

99. Wang, D.; Choi, D.; Li, J.; Yang, Z.; Nie, Z.; Kou, R.; Hu, D.; Wang, C.; Saraf, L. V.; Zhang, J.; Aksay, I. A.; Liu, J., Self-Assembled TiO_2-Graphene Hybrid Nanostructures for Enhanced Li-Ion Insertion. *Acs Nano* **2009,** 3, (4), 907-914.
100. Dinnebier, R. E.; Billinge, S. J., Powder diffraction: theory and practice. *Royal society of chemistry* **2008**.
101. McCusker, L. B.; Von Dreele, R. B.; Cox, D. E.; Louer, D.; Scardi, P., Rietveld refinement guidelines. *Journal of Applied Crystallography* **1999,** 32, 36-50.
102. Rodriguez-Carvajal, J., FULLPROF version 2.05. *ILL [unpublished]* **July 2011**.
103. Thommes, M.; Kaneko, K.; Neimark, A. V.; Olivier, J. P.; Rodriguez-Reinoso, F.; Rouquerol, J.; Sing, K. S., Physisorption of gases, with special reference to the evaluation of surface area and pore size distribution (IUPAC Technical Report). *Pure and Applied Chemistry* **2015,** 87, (9-10), 1051-1069.
104. Ravikovitch, P. I.; Neimark, A. V., Experimental confirmation of different mechanisms of evaporation from ink-bottle type pores: Equilibrium, pore blocking, and cavitation. *Langmuir* **2002,** 18, (25), 9830-9837.
105. Thommes, M.; Smarsly, B.; Groenewolt, M.; Ravikovitch, P. I.; Neimark, A. V., Adsorption hysteresis of nitrogen and argon in pore networks and characterization of novel micro- and mesoporous silicas. *Langmuir* **2006,** 22, (2), 756-764.
106. Neimark, A. V.; Ravikovitch, P. I., Capillary condensation in MMS and pore structure characterization. *Microporous and Mesoporous Materials* **2001,** 44, 697-707.
107. Ravikovitch, P. I.; Neimark, A. V., Density functional theory of adsorption in spherical cavities and pore size characterization of templated nanoporous silicas with cubic and three-dimensional hexagonal structures. *Langmuir* **2002,** 18, (5), 1550-1560.
108. Bard, A. J.; Faulkner, L. R., Electrochemical methods: fundamentals and applications. *Wiley New York*: **1980**, 2.
109. Shin, J.-Y.; Joo, J. H.; Samuelis, D.; Maier, J., Oxygen-Deficient $TiO_{2-\delta}$ Nanoparticles via Hydrogen Reduction for High Rate Capability Lithium Batteries. *Chemistry of Materials* **2011,** 24, (3), 543-551.
110. Chen, Y.; Ma, X.; Cui, X.; Jiang, Z., In situ synthesis of carbon incorporated TiO_2 with long-term performance as anode for lithium-ion batteries. *Journal of Power Sources* **2016,** 302, 233-239.
111. Levi, M. D.; Salitra, G.; Markovsky, B.; Teller, H.; Aurbach, D.; Heider, U.; Heider, L., Solid-state electrochemical kinetics of Li-ion intercalation into $Li_{1-x}CoO_2$: Simultaneous application of electroanalytical techniques SSCV, PITT, and EIS. *Journal of the Electrochemical Society* **1999,** 146, (4), 1279-1289.
112. Ho, C.; Raistrick, I. D.; Huggins, R. A., Application Of AC Techniques To The Study Of Lithium Diffusion In Tungsten Trioxide Thin-Films. *Journal of the Electrochemical Society* **1980,** 127, (2), 343-350.
113. Van der Ven, A.; Bhattacharya, J.; Belak, A. A., Understanding Li Diffusion in Li-Intercalation Compounds. *Accounts of Chemical Research* **2013,** 46, (5), 1216-1225.
114. Wang, C.; Kasavajjula, U. S.; Arce, P. E., A Discharge Model for Phase Transformation Electrodes: Formulation, Experimental Validation, and Analysis. *The Journal of Physical Chemistry C* **2007,** 111, (44), 16656-16663.
115. Zhu, Y.; Wang, C., Galvanostatic Intermittent Titration Technique for Phase-Transformation Electrodes. *The Journal of Physical Chemistry C* **2010,** 114, (6), 2830-2841.
116. Zhu, Y.; Wang, C., Novel CV for Phase Transformation Electrodes. *The Journal of Physical Chemistry C* **2011,** 115, (3), 823-832.
117. Hebb, M. H., Electrical Conductivity Of Siliver Sulfide. *Journal of Chemical Physics* **1952,** 20, (1), 185-190.
118. Wagner, C., Investigations On Silver Sulfide. *Journal of Chemical Physics* **1953,** 21, (10), 1819-1827.
119. Zhang, W. F.; He, Y. L.; Zhang, M. S.; Yin, Z.; Chen, Q., Raman scattering study on anatase TiO_2 nanocrystals. *Journal of Physics D-Applied Physics* **2000,** 33, (8), 912-916.
120. Ohsaka, T.; Izumi, F.; Fujiki, Y., Raman spectrum of anatase, TiO_2. *Journal of Raman Spectroscopy* **1978,** 7, (6), 321-324.

121. Tian, F.; Zhang, Y.; Zhang, J.; Pan, C., Raman Spectroscopy: A New Approach to Measure the Percentage of Anatase TiO_2 Exposed (001) Facets. *The Journal of Physical Chemistry C* **2012,** 116, (13), 7515-7519.
122. Lü, X.; Yang, W.; Quan, Z.; Lin, T.; Bai, L.; Wang, L.; Huang, F.; Zhao, Y., Enhanced Electron Transport in Nb-Doped TiO_2 Nanoparticles via Pressure-Induced Phase Transitions. *Journal of the American Chemical Society* **2014,** 136, (1), 419-426.
123. Ruiz, A. M.; Dezanneau, G.; Arbiol, J.; Cornet, A.; Morante, J. R., Insights into the Structural and Chemical Modifications of Nb Additive on TiO_2 Nanoparticles. *Chemistry of Materials* **2004,** 16, (5), 862-871.
124. Lü, X.; Mou, X.; Wu, J.; Zhang, D.; Zhang, L.; Huang, F.; Xu, F.; Huang, S., Improved-Performance Dye-Sensitized Solar Cells Using Nb-Doped TiO_2 Electrodes: Efficient Electron Injection and Transfer. *Advanced Functional Materials* **2010,** 20, (3), 509-515.
125. Sheppard, L. R.; Dittrich, T.; Nowotny, M. K., The Impact of Niobium Surface Segregation on Charge Separation in Niobium-Doped Titanium Dioxide. *The Journal of Physical Chemistry C* **2012,** 116, (39), 20923-20929.
126. Gardecka, A. J.; Goh, G. K. L.; Sankar, G.; Parkin, I. P., On the nature of niobium substitution in niobium doped titania thin films by AACVD and its impact on electrical and optical properties. *Journal of Materials Chemistry A* **2015,** 3, (34), 17755-17762.
127. Yu, J.-G.; Yu, H.-G.; Cheng, B.; Zhao, X.-J.; Yu, J. C.; Ho, W.-K., The Effect of Calcination Temperature on the Surface Microstructure and Photocatalytic Activity of TiO_2 Thin Films Prepared by Liquid Phase Deposition. *The Journal of Physical Chemistry B* **2003,** 107, (50), 13871-13879.
128. Leichtweiss, T.; Henning, R. A.; Koettgen, J.; Schmidt, R. M.; Hollander, B.; Martin, M.; Wuttig, M.; Janek, J., Amorphous and highly nonstoichiometric titania (TiOx) thin films close to metal-like conductivity. *Journal of Materials Chemistry A* **2014,** 2, (18), 6631-6640.
129. Wang, Y.; Smarsly, B. M.; Djerdj, I., Niobium Doped TiO_2 with Mesoporosity and Its Application for Lithium Insertion. *Chemistry of Materials* **2010,** 22, (24), 6624-6631.
130. Mei, B.; Sanchez, M. D.; Reinecke, T.; Kaluza, S.; Xia, W.; Muhler, M., The synthesis of Nb-doped TiO_2 nanoparticles by spray drying: an efficient and scalable method. *Journal of Materials Chemistry* **2011,** 21, (32), 11781-11790.
131. Bradley, D.; Mehrotra, R. C.; Rothwell, I.; Singh, A., Alkoxo and aryloxo derivatives of metals. *Academic Press* **2001**.
132. Elm, M. T.; Hofmann, J. D.; Suchomski, C.; Janek, J.; Brezesinski, T., Ionic Conductivity of Mesostructured Yttria-Stabilized Zirconia Thin Films with Cubic Pore Symmetry-On the Influence of Water on the Surface Oxygen Ion Transport. *Acs Applied Materials & Interfaces* **2015,** 7, (22), 11792-11801.
133. Voepel, P.; Suchomski, C.; Hofmann, A.; Gross, S.; Dolcet, P.; Smarsly, B. M., In-depth mesocrystal formation analysis of microwave-assisted synthesis of $LiMnPO_4$ nanostructures in organic solution. *Crystengcomm* **2016,** 18, (2), 316-327.
134. Mutin, P. H.; Vioux, A., Nonhydrolytic Processing of Oxide-Based Materials: Simple Routes to Control Homogeneity, Morphology, and Nanostructure. *Chemistry of Materials* **2009,** 21, (4), 582-596.
135. Wagemaker, M.; Kentgens, A. P. M.; Mulder, F. M., Equilibrium lithium transport between nanocrystalline phases in intercalated TiO_2 anatase. *Nature* **2002,** 418, (6896), 397-399.
136. Shin, J.-Y.; Samuelis, D.; Maier, J., Sustained Lithium-Storage Performance of Hierarchical, Nanoporous Anatase TiO_2 at High Rates: Emphasis on Interfacial Storage Phenomena. *Advanced Functional Materials* **2011,** 21, (18), 3464-3472.
137. Shin, J.-Y.; Joo, J. H.; Adepalli, K. K.; Samuelis, D.; Maier, J. The effects of n-type doping on lithium storage in TiO_2. *Physical Chemistry Chemical Physics* **2016**, 18, 8963-8970.
138. Fehse, M.; Cavaliere, S.; Lippens, P. E.; Savych, I.; Iadecola, A.; Monconduit, L.; Jones, D. J.; Rozière, J.; Fischer, F.; Tessier, C.; Stievano, L., Nb-Doped TiO_2 Nanofibers for Lithium Ion Batteries. *The Journal of Physical Chemistry C* **2013,** 117, (27), 13827-13835.
139. Hartmann, P.; Lee, D.-K.; Smarsly, B. M.; Janek, J., Mesoporous TiO_2: Comparison of Classical Sol-Gel and Nanoparticle Based Photoelectrodes for the Water Splitting Reaction. *Acs Nano* **2010,** 4, (6), 3147-3154.

140. Sing, K. S. W.; Everett, D. H.; Haul, R. A. W.; Moscou, L.; Pierotti, R. A.; Rouquerol, J.; Siemieniewska, T., Reporting Physisorption Data for Gas/Solid Systems. In *Handbook of Heterogeneous Catalysis*, Wiley-VCH Verlag GmbH & Co. KGaA: **2008**.
141. Reitz, C.; Reinacher, J.; Hartmann, P.; Brezesinski, T., Polymer-templated ordered large-pore mesoporous anatase rutile TiO_2:Ta nanocomposite films: Microstructure, electrical conductivity, and photocatalytic and photoelectrochemical properties. *Catalysis Today* **2014,** 225, 55-63.
142. Brezesinski, T.; Wang, J.; Tolbert, S. H.; Dunn, B., Next generation pseudocapacitor materials from sol-gel derived transition metal oxides. *Journal of Sol-Gel Science and Technology* **2011,** 57, (3), 330-335.
143. Augustyn, V.; Simon, P.; Dunn, B., Pseudocapacitive oxide materials for high-rate electrochemical energy storage. *Energy & Environmental Science* **2014,** 7, (5), 1597-1614.
144. Lauria, A.; Villa, I.; Fasoli, M.; Niederberger, M.; Vedda, A., Multifunctional Role of Rare Earth Doping in Optical Materials: Nonaqueous Sol–Gel Synthesis of Stabilized Cubic HfO_2 Luminescent Nanoparticles. *ACS Nano* **2013,** 7, (8), 7041-7052.
145. Bai, X.; Pucci, A.; Freitas, V. T.; Ferreira, R. A. S.; Pinna, N., One-Step Synthesis and Optical Properties of Benzoate- and Biphenolate-Capped ZrO_2 Nanoparticles. *Advanced Functional Materials* **2012,** 22, (20), 4275-4283.
146. Mukai, K.; Kato, Y.; Nakano, H., Understanding the Zero-Strain Lithium Insertion Scheme of $Li[Li_{1/3}Ti_{5/3}]O_4$: Structural Changes at Atomic Scale Clarified by Raman Spectroscopy. *The Journal of Physical Chemistry C* **2014,** 118, (6), 2992-2999.
147. Julien, C. M.; Massot, M.; Zaghib, K., Structural studies of $Li_{4/3}Me_{5/3}O_4$ (Me = Ti, Mn) electrode materials: local structure and electrochemical aspects. *Journal of Power Sources* **2004,** 136, (1), 72-79.
148. Leonidov, I. A.; Leonidova, O. N.; Perelyaeva, L. A.; Samigullina, R. F.; Kovyazina, S. A.; Patrakeev, M. V., Structure, ionic conduction, and phase transformations in lithium titanate $Li_4Ti_5O_{12}$. *Physics of the Solid State* **2003,** 45, (11), 2183-2188.
149. Aldon, L.; Kubiak, P.; Womes, M.; Jumas, J. C.; Olivier-Fourcade, J.; Tirado, J. L.; Corredor, J. I.; Vicente, C. P., Chemical and electrochemical Li-insertion into the $Li_4Ti_5O_{12}$ spinel. *Chemistry of Materials* **2004,** 16, (26), 5721-5725.
150. Baddour-Hadjean, R.; Pereira-Ramos, J.-P., Raman Microspectrometry Applied to the Study of Electrode Materials for Lithium Batteries. *Chemical Reviews* **2010,** 110, (3), 1278-1319.
151. Krajewski, M.; Michalska, M.; Hamankiewicz, B.; Ziolkowska, D.; Korona, K. P.; Jasinski, J. B.; Kaminska, M.; Lipinska, L.; Czerwinski, A., $Li_4Ti_5O_{12}$ modified with Ag nanoparticles as an advanced anode material in lithium-ion batteries. *Journal of Power Sources* **2014,** 245, 764-771.
152. Kim, C.; Norberg, N. S.; Alexander, C. T.; Kostecki, R.; Cabana, J., Mechanism of Phase Propagation During Lithiation in Carbon-Free $Li_4Ti_5O_{12}$ Battery Electrodes. *Advanced Functional Materials* **2013,** 23, (9), 1214-1222.
153. Lippens, P.-E.; Womes, M.; Kubiak, P.; Jumas, J.-C.; Olivier-Fourcade, J., Electronic structure of the spinel $Li_4Ti_5O_{12}$ studied by ab initio calculations and X-ray absorption spectroscopy. *Solid State Sciences* **2004,** 6, (2), 161-166.
154. He, Y.-B.; Liu, M.; Huang, Z.-D.; Zhang, B.; Yu, Y.; Li, B.; Kang, F.; Kim, J.-K., Effect of solid electrolyte interface (SEI) film on cyclic performance of $Li_4Ti_5O_{12}$ anodes for Li ion batteries. *Journal of Power Sources* **2013,** 239, 269-276.
155. Guo, M.; Wang, S.; Ding, L.-X.; Zheng, L.; Wang, H., Synthesis of novel nitrogen-doped lithium titanate with ultra-high rate capability using melamine as a solid nitrogen source. *Journal of Materials Chemistry A* **2015,** 3, (20), 10753-10759.
156. Shi, Y.; Wen, L.; Li, F.; Cheng, H.-M., Nanosized $Li_4Ti_5O_{12}$/graphene hybrid materials with low polarization for high rate lithium ion batteries. *Journal of Power Sources* **2011,** 196, (20), 8610-8617.
157. Herstedt, M.; Andersson, A. M.; Rensmo, H.; Siegbahn, H.; Edström, K., Characterisation of the SEI formed on natural graphite in PC-based electrolytes. *Electrochimica Acta* **2004,** 49, (27), 4939-4947.
158. Nordh, T.; Younesi, R.; Brandell, D.; Edström, K., Depth profiling the solid electrolyte interphase on lithium titanate ($Li_4Ti_5O_{12}$) using synchrotron-based photoelectron spectroscopy. *Journal of Power Sources* **2015,** 294, 173-179.

159. Dedryvère, R.; Gireaud, L.; Grugeon, S.; Laruelle, S.; Tarascon, J. M.; Gonbeau, D., Characterization of Lithium Alkyl Carbonates by X-ray Photoelectron Spectroscopy: Experimental and Theoretical Study. *The Journal of Physical Chemistry B* **2005,** 109, (33), 15868-15875.
160. Gao, Y.; Wang, Z.; Chen, L., Stability of spinel $Li_4Ti_5O_{12}$ in air. *Journal of Power Sources* **2014,** 245, 684-690.
161. Snyder, M. Q.; DeSisto, W. J.; Tripp, C. P., An infrared study of the surface chemistry of lithium titanate spinel ($Li_4Ti_5O_{12}$). *Applied Surface Science* **2007,** 253, (24), 9336-9341.
162. Brooker, M. H.; Wang, J., Raman and infrared studies of lithium and cesium carbonates. *Spectrochimica Acta Part A: Molecular Spectroscopy* **1992,** 48, (7), 999-1008.
163. Tunesi, S.; Anderson, M. A., Surface effects in photochemistry: an in situ cylindrical internal reflection-Fourier transform infrared investigation of the effect of ring substituents on chemisorption onto titania ceramic membranes. *Langmuir* **1992,** 8, (2), 487-495.
164. Dobson, K. D.; McQuillan, A. J., In situ infrared spectroscopic analysis of the adsorption of aromatic carboxylic acids to TiO_2, ZrO_2, Al_2O_3, and Ta_2O_5 from aqueous solutions. *Spectrochimica Acta Part A: Molecular and Biomolecular Spectroscopy* **2000,** 56, (3), 557-565.
165. Pinna, N.; Garnweitner, G.; Beato, P.; Niederberger, M.; Antonietti, M., Synthesis of Yttria-Based Crystalline and Lamellar Nanostructures and their Formation Mechanism. *Small* **2005,** 1, (1), 112-121.
166. Pucci, A.; Willinger, M.-G.; Liu, F.; Zeng, X.; Rebuttini, V.; Clavel, G.; Bai, X.; Ungar, G.; Pinna, N., One-Step Synthesis and Self-Assembly of Metal Oxide Nanoparticles into 3D Superlattices. *ACS Nano* **2012,** 6, (5), 4382-4391.
167. Niederberger, M.; Pinna, N.: Metal oxide nanoparticles in organic solvents: synthesis, formation, assembly and application. *Springer Science & Business Media*, **2009**.
168. Mahrwald, R., Enantioselective C−C Bond Formation with Titanium(IV) Alkoxides—an Unusual Alkylation. *Angewandte Chemie International Edition* **2002,** 41, (8), 1361-1363.
169. Pinna, N.; Garnweitner, G.; Antonietti, M.; Niederberger, M., Non-Aqueous Synthesis of High-Purity Metal Oxide Nanopowders Using an Ether Elimination Process. *Advanced Materials* **2004,** 16, (23-24), 2196-2200.
170. Niederberger, M.; Garnweitner, G.; Pinna, N.; Antonietti, M., Nonaqueous and Halide-Free Route to Crystalline $BaTiO_3$, $SrTiO_3$, and $(Ba,Sr)TiO_3$ Nanoparticles via a Mechanism Involving C−C Bond Formation. *Journal of the American Chemical Society* **2004,** 126, (29), 9120-9126.
171. Miao, Z.; Xu, D. S.; Ouyang, J. H.; Guo, G. L.; Zhao, X. S.; Tang, Y. Q., Electrochemically induced sol-gel preparation of single-crystalline TiO_2 nanowires. *Nano Letters* **2002,** 2, (7), 717-720.
172. Bersani, D.; Lottici, P. P.; Ding, X. Z., Phonon confinement effects in the Raman scattering by TiO2 nanocrystals. *Applied Physics Letters* **1998,** 72, (1), 73-75.
173. Wagemaker, M.; Simon, D. R.; Kelder, E. M.; Schoonman, J.; Ringpfeil, C.; Haake, U.; Lützenkirchen-Hecht, D.; Frahm, R.; Mulder, F. M., A Kinetic Two-Phase and Equilibrium Solid Solution in Spinel $Li_{4+x}Ti_5O_{12}$. *Advanced Materials* **2006,** 18, (23), 3169-3173.
174. Luo, L.; Rossell, M. D.; Xie, D.; Erni, R.; Niederberger, M., Microwave-Assisted Nonaqueous Sol–Gel Synthesis: From Al:ZnO Nanoparticles to Transparent Conducting Films. *ACS Sustainable Chemistry & Engineering* **2013,** 1, (1), 152-160.
175. Kominami, H.; Oki, K.; Kohno, M.; Onoue, S.-i.; Kera, Y.; Ohtani, B., Novel solvothermal synthesis of niobium(v) oxide powders and their photocatalytic activity in aqueous suspensions. *Journal of Materials Chemistry* **2001,** 11, (2), 604-609.
176. Orel, B.; Maček, M.; Grdadolnik, J.; Meden, A., In situ UV-Vis and ex situ IR spectroelectrochemical investigations of amorphous and crystalline electrochromic Nb_2O_5 films in charged/discharged states. *Journal of Solid State Electrochemistry* **1998,** 2, (4), 221-236.
177. Lin, C. F.; Fan, X. Y.; Xin, Y. L.; Cheng, F. Q.; Lai, M. O.; Zhou, H. H.; Lu, L. $Li_4Ti_5O_{12}$-based anode materials with low working potentials, high rate capabilities and high cyclability for high-power lithium-ion batteries: a synergistic effect of doping, incorporating a conductive phase and reducing the particle size. *Journal of Materials Chemistry A* **2014**, *2*, 9982-9993.

178. Lin, C.; Ding, B.; Xin, Y.; Cheng, F.; Lai, M. O.; Lu, L.; Zhou, H., Advanced electrochemical performance of $Li_4Ti_5O_{12}$-based materials for lithium-ion battery: Synergistic effect of doping and compositing. *Journal of Power Sources* **2014,** 248, 1034-1041.
179. Cai, R.; Jiang, S.; Yu, X.; Zhao, B.; Wang, H.; Shao, Z., A novel method to enhance rate performance of an Al-doped $Li_4Ti_5O_{12}$ electrode by post-synthesis treatment in liquid formaldehyde at room temperature. *Journal of Materials Chemistry* **2012,** 22, (16), 8013-8021.
180. Kavan, L.; Procházka, J.; Spitler, T. M.; Kalbáč, M.; Zukalová, M. t.; Drezen, T.; Grätzel, M., Li Insertion into $Li_4Ti_5O_{12}$ (Spinel). *Journal of The Electrochemical Society* **2003,** 150, (7), A1000.
181. Hong, Z. S.; Zhou, K. Q.; Huang, Z. G.; Wei, M. D. Iso-Oriented Anatase TiO2 Mesocages as a High Performance Anode Material for Sodium-Ion Storage. *Scientific Reports* **2015**, *5*, 10.
182. Yu, L.; Wu, H. B.; Lou, X. W., Mesoporous $Li_4Ti_5O_{12}$ Hollow Spheres with Enhanced Lithium Storage Capability. *Advanced Materials* **2013,** 25, (16), 2296-2300.
183. Kang, E.; Jung, Y. S.; Kim, G.-H.; Chun, J.; Wiesner, U.; Dillon, A. C.; Kim, J. K.; Lee, J., Highly Improved Rate Capability for a Lithium-Ion Battery Nano- $Li_4Ti_5O_{12}$ Negative Electrode via Carbon-Coated Mesoporous Uniform Pores with a Simple Self-Assembly Method. *Advanced Functional Materials* **2011,** 21, (22), 4349-4357.
184. Pasierb, P.; Komornicki, S.; Rokita, M.; Rękas, M., Structural properties of Li_2CO_3–$BaCO_3$ system derived from IR and Raman spectroscopy. *Journal of Molecular Structure* **2001,** 596, (1–3), 151-156.
185. Mosqueda, H. A.; Vazquez, C.; Bosch, P.; Pfeiffer, H., Chemical Sorption of Carbon Dioxide (CO_2) on Lithium Oxide (Li_2O). *Chemistry of Materials* **2006,** 18, (9), 2307-2310.
186. Eckhardt, B.; Ortel, E.; Bernsmeier, D.; Polte, J.; Strasser, P.; Vainio, U.; Emmerling, F.; Kraehnert, R., Micelle-Templated Oxides and Carbonates of Zinc, Cobalt, and Aluminum and a Generalized Strategy for Their Synthesis. *Chemistry of Materials* **2013,** 25, (14), 2749-2758.
187. Eckhardt, B.; Ortel, E.; Polte, J.; Bernsmeier, D.; Goerke, O.; Strasser, P.; Kraehnert, R., Micelle-Templated Mesoporous Films of Magnesium Carbonate and Magnesium Oxide. *Advanced Materials* **2012,** 24, (23), 3115-3119.
188. Brezesinski, T.; Fischer, A.; Iimura, K.-i.; Sanchez, C.; Grosso, D.; Antonietti, M.; Smarsly, B. M., Generation of self-assembled 3D mesostructured SnO_2 thin films with highly crystalline frameworks. *Advanced Functional Materials* **2006,** 16, (11), 1433-1440.
189. Erk, C.; Brezesinski, T.; Sommer, H.; Schneider, R.; Janek, J., Toward Silicon Anodes for Next-Generation Lithium Ion Batteries: A Comparative Performance Study of Various Polymer Binders and Silicon Nanopowders. *ACS Applied Materials & Interfaces* **2013,** 5, (15), 7299-7307.
190. Schroeder, M.; Sallard, S.; Boehm, M.; Einert, M.; Suchomski, C.; Smarsly, B. M.; Mutisya, S.; Bertino, M. F., An All Low-Temperature Fabrication of Macroporous, Electrochemically Addressable Anatase Thin Films. *Small* **2014,** 10, (8), 1566-1574.
191. Xu, H. H.; Hu, X. L.; Luo, W.; Sun, Y. M.; Yang, Z.; Hu, C. C.; Huang, Y. H., Electrospun Conformal $Li_4Ti_5O_{12}$/C Fibers for High-Rate Lithium-Ion Batteries. *Chemelectrochem* **2014,** 1, (3), 611-616.
192. Lu, H.-W.; Zeng, W.; Li, Y.-S.; Fu, Z.-W., Fabrication and electrochemical properties of three-dimensional net architectures of anatase TiO_2 and spinel $Li_4Ti_5O_{12}$ nanofibers. *Journal of Power Sources* **2007,** 164, (2), 874-879.
193. Park, H.; Song, T.; Han, H.; Paik, U., Electrospun $Li_4Ti_5O_{12}$ nanofibers sheathed with conductive TiN/TiOxNy layer as an anode material for high power Li-ion batteries. *Journal of Power Sources* **2013,** 244, 726-730.
194. Wu, Y.; Reddy, M. V.; Chowdari, B. V. R.; Ramakrishna, S., Electrochemical studies on electrospun $Li(Li_{1/3}Ti_{5/3})O_4$ grains as an anode for Li-ion batteries. *Electrochimica Acta* **2012,** 67, 33-40.
195. Zhu, N.; Liu, W.; Xue, M.; Xie, Z.; Zhao, D.; Zhang, M.; Chen, J.; Cao, T., Graphene as a conductive additive to enhance the high-rate capabilities of electrospun $Li_4Ti_5O_{12}$ for lithium-ion batteries. *Electrochimica Acta* **2010,** 55, (20), 5813-5818.
196. Konishi, J.; Fujita, K.; Nakanishi, K.; Hirao, K., Monolithic TiO_2 with controlled multiscale porosity via a template-free sol-gel process accompanied by phase separation. *Chemistry of Materials* **2006,** 18, (25), 6069-6074.

197. Konishi, J.; Fujita, K.; Nakanishi, K.; Hirao, K., Phase-Separation-Induced Titania Monoliths with Well-Defined Macropores and Mesostructured Framework from Colloid-Derived Sol–Gel Systems. *Chemistry of Materials* **2006,** 18, (4), 864-866.
198. Hara, T.; Makino, S.; Watanabe, Y.; Ikegami, T.; Cabrera, K.; Smarsly, B.; Tanaka, N., The performance of hybrid monolithic silica capillary columns prepared by changing feed ratios of tetramethoxysilane and methyltrimethoxysilane. *Journal of Chromatography A* **2010,** 1217, (1), 89-98.
199. von der Lehr, M.; Weidmann, C.; Mascotto, S.; Smarsly, B. M., Hierarchically Ordered Monolithic Silica with Bimodal Porosity Obtained by Hydrolysis and Condensation of 1,4-Bis(trimethoxysilyl)arenes. *Chemie Ingenieur Technik* **2013,** 85, (11), 1700-1706.
200. Wesselt, C.; Ostermann, R.; Dersch, R.; Smarsly, B. M., Formation of Inorganic Nanofibers from Preformed TiO_2 Nanoparticles via Electrospinning. *Journal of Physical Chemistry C* **2011,** 115, (2), 362-372.
201. Faber, K.; Badaczewski, F.; Oschatz, M.; Mondin, G.; Nickel, W.; Kaskel, S.; Smarsly, B. M., In-Depth Investigation of the Carbon Microstructure of Silicon Carbide-Derived Carbons by Wide-Angle X-ray Scattering. *Journal of Physical Chemistry C* **2014,** 118, (29), 15705-15715.

APPENDIX

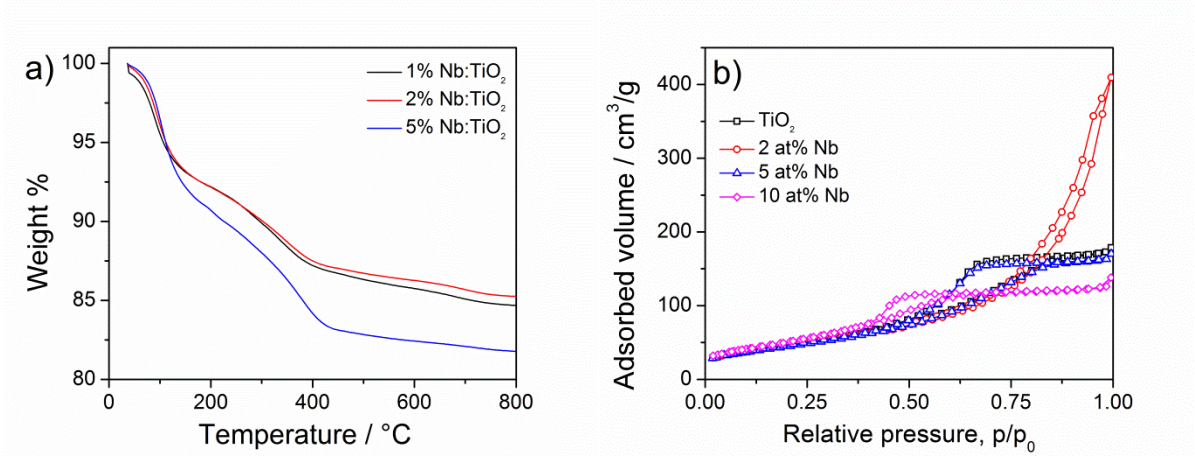

Figure 1 Thermal gravimetric analysis of as-made Nb:TiO_2 and Nitrogen adsorption and desorption isotherms (77K) of annealed Nb:TiO_2. The adsorbed water can be removed at around 100 °C and the organic residues can be totally eliminated at 400 °C. The total weight loss is in the range of 15 wt% to 18 wt%.

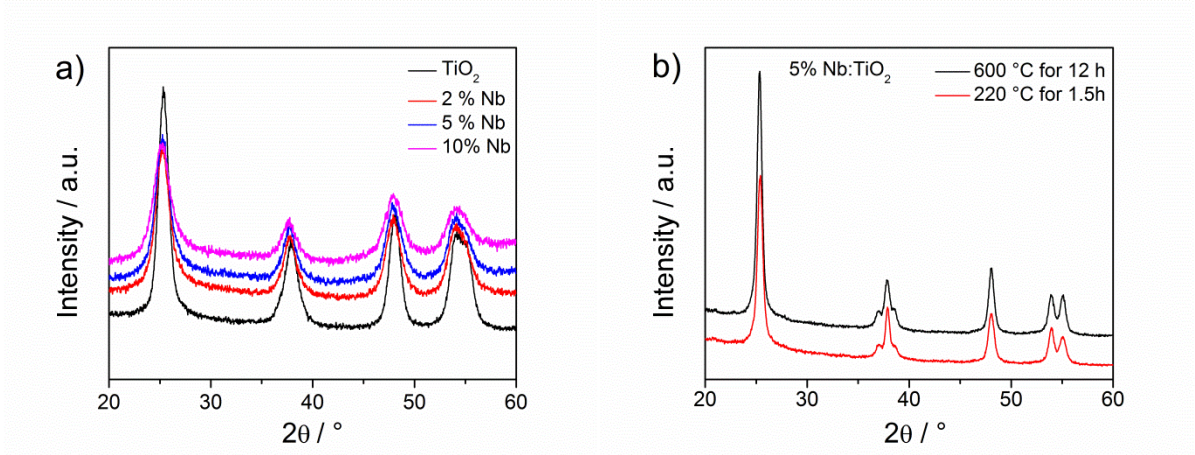

Figure 2 (a) XRD patterns of as-made TiO_2 and doped TiO_2. The crystallite sizes for as-made TiO_2, 2 at%, 5 at% and 10 at% Nb:TiO_2 are 4.7, 4.9, 4.9 and 4.2 nm respectively. (b) The XRD patterns of 5 at% Nb:TiO_2. The black curve is the nanocrystals calcined at 600 °C for 12 hours. Red curve is nanocrystals from benzyl alcohol route with reaction time of 90 min and reaction temperature of 220 °C.

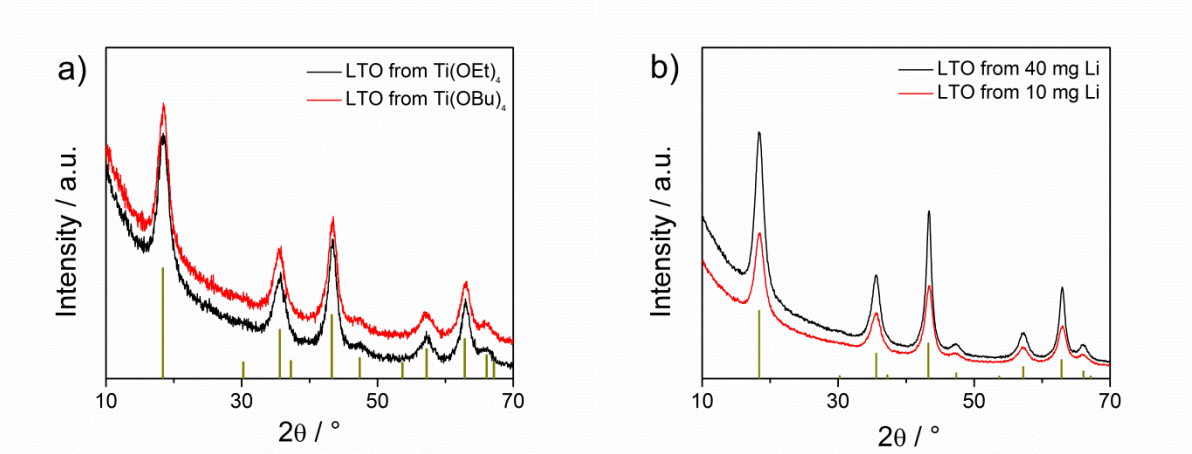

Figure 3 XRD patterns of LTO nanocrystals from different conditions. (a) LTO nanocrystals were obtained using $Ti(OEt)_4$ and $Ti(OBu)_4$ as precursors at temperature of 230 °C and the Lithium mass of 20 mg. (b) LTO nanocrystals were obtained at Lithium mass of 10 mg and 40 mg with $Ti(O\text{-}iso\text{-}Pr)_4$ as precursors at temperature of 230 °C.

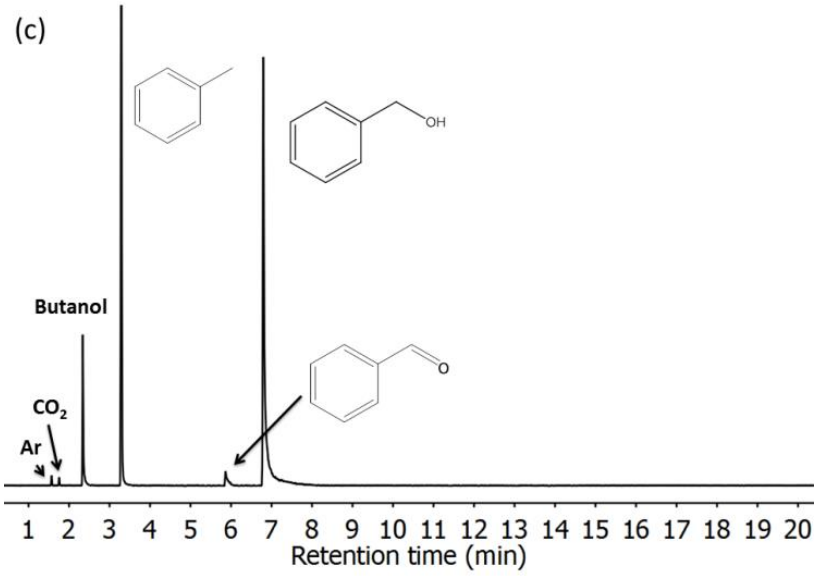

Figure 4 GC-MS of liquid reaction product from the precursor of $Ti(OBu)_4$. The same products can be found with the ones from the precursor of $Ti(OEt)_4$.

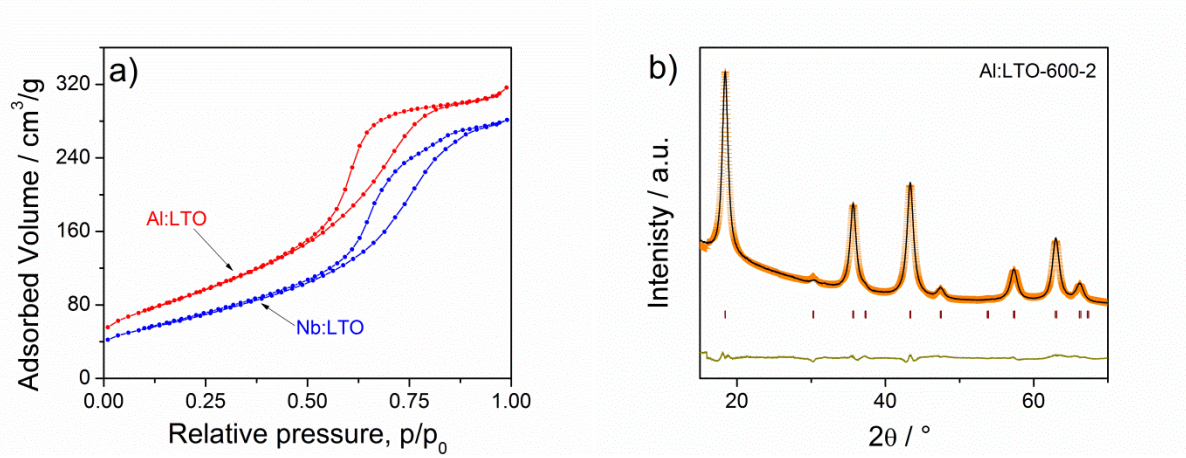

Figure 5 (a) N_2 physisorption isotherms (77K) of annealed Al:LTO and Nb:LTO and (b) XRD patterns of Al:LTO-600-2, along with the Rietveld refinement.

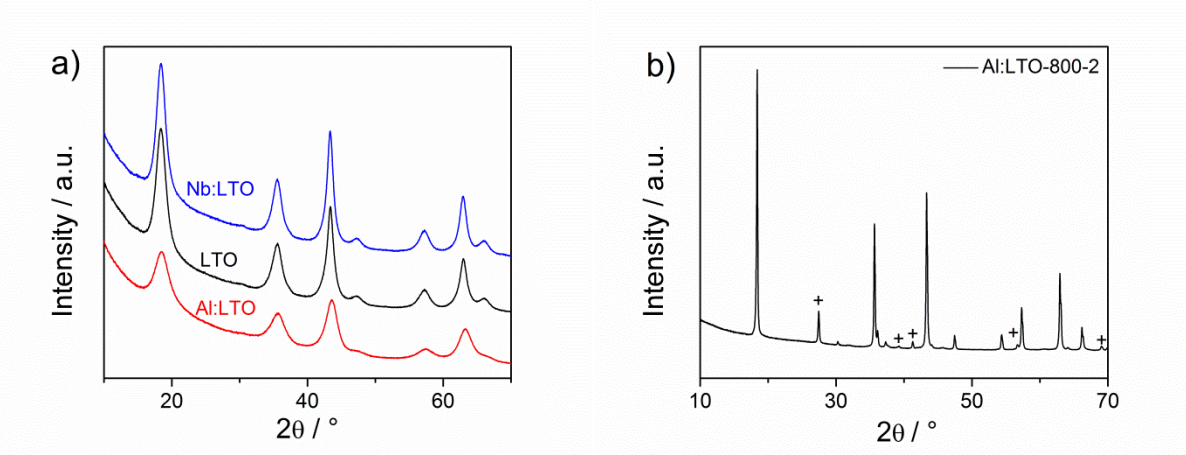

Figure 6 (a) XRD patterns of as-made doped LTO nanocrystals. (b) Al:LTO nanocrytals treated at 800 °C. The "+" stand for the diffraction peaks of rutile TiO_2.

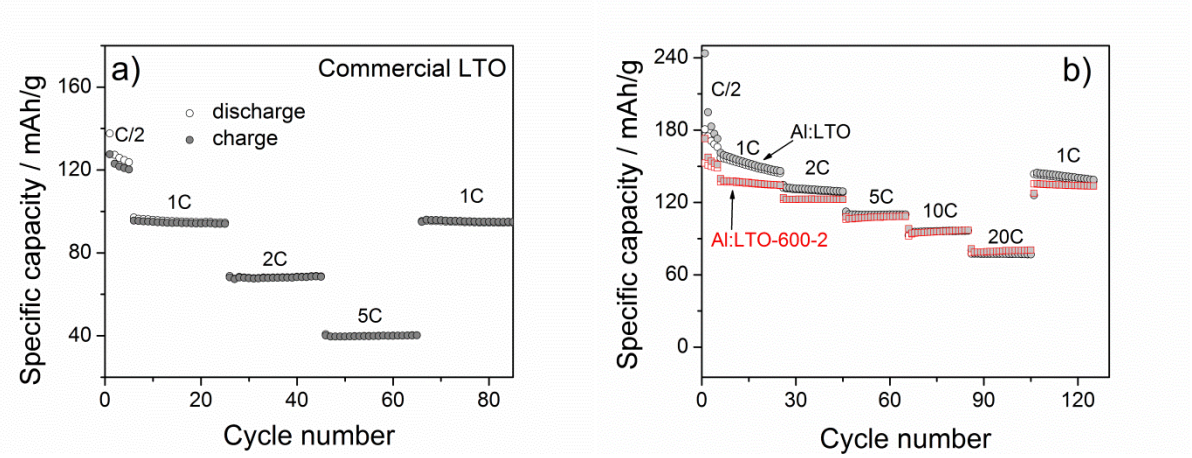

Figure 7 (a) Rate capacity of commercial LTO electrodes. The specific capacity at C/2 is only 120 mA/g, much less than theoretical value (175 mA/g), which indicates the poor rate performance of commercial LTO. (b) Rate capacity of Al:LTO and Al:LTO-600 nanocrystals. Although the specific capacity of Al:LTO is higher than Al:LTO-600 due to the significant interfacial charge storage, the stability of such capacity is much worse than Al:LTO-600.

After 20 cycles at 1C, the specific capacity of Al:LTO drops from 157 mA/g to 144 mA/g, while the drop is 2 mAh/g for Al:LTO-600.

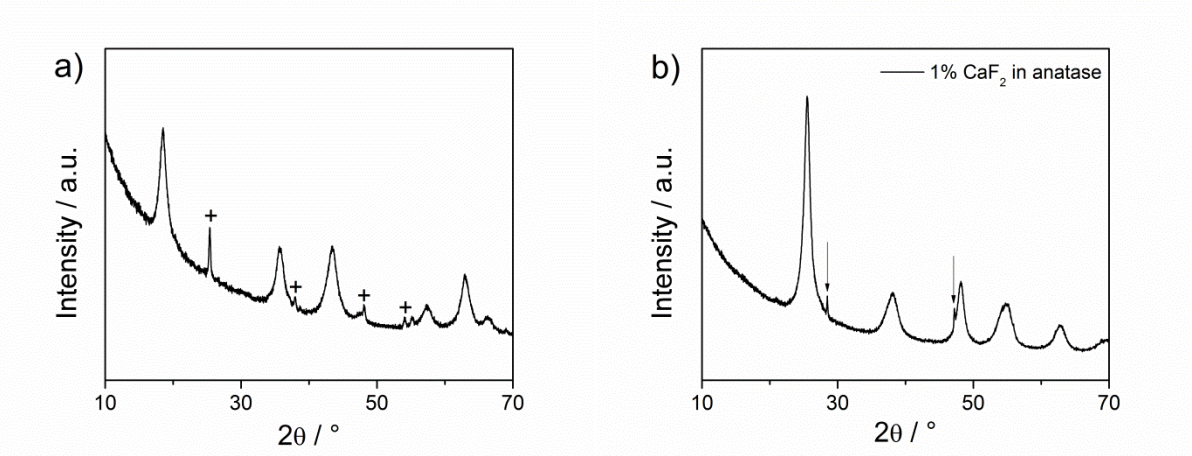

Figure 8 (a) XRD patterns of LTO powders prepared by sol-gel process without PIB_{50}-*b*-PEO_{45} copolymer. The Plus stands for anatase phase, indicating that it is not possible to obtain phase pure LTO powder without copolymers. (b) XRD patterns of 1 wt% CaF_2 in anatase. The arrows indicate the CaF_2 phase, implying the detection limit content from XRD patterns is less than 1 wt%.

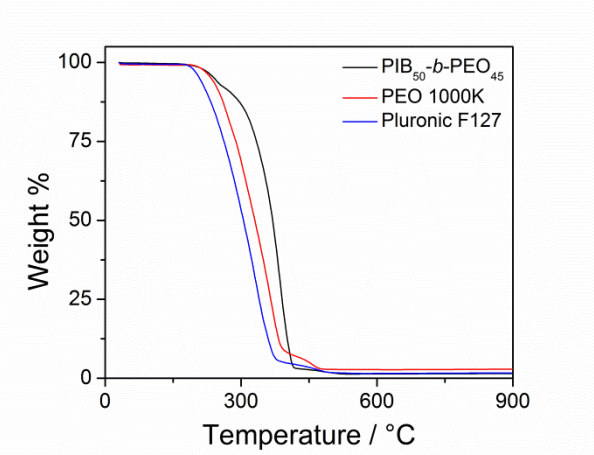

Figure 9 Thermogravimetric analyses of different polymers in air. The starting decomposition temperatures for PIB50-*b*-PEO45, PEO 1000K and Pluronic F127 are 320, 220 and 200 °C respectively. The high decomposition temperature of PIB50-*b*-PEO45 is of great help for maintaining the porous structure during the crystallization process.

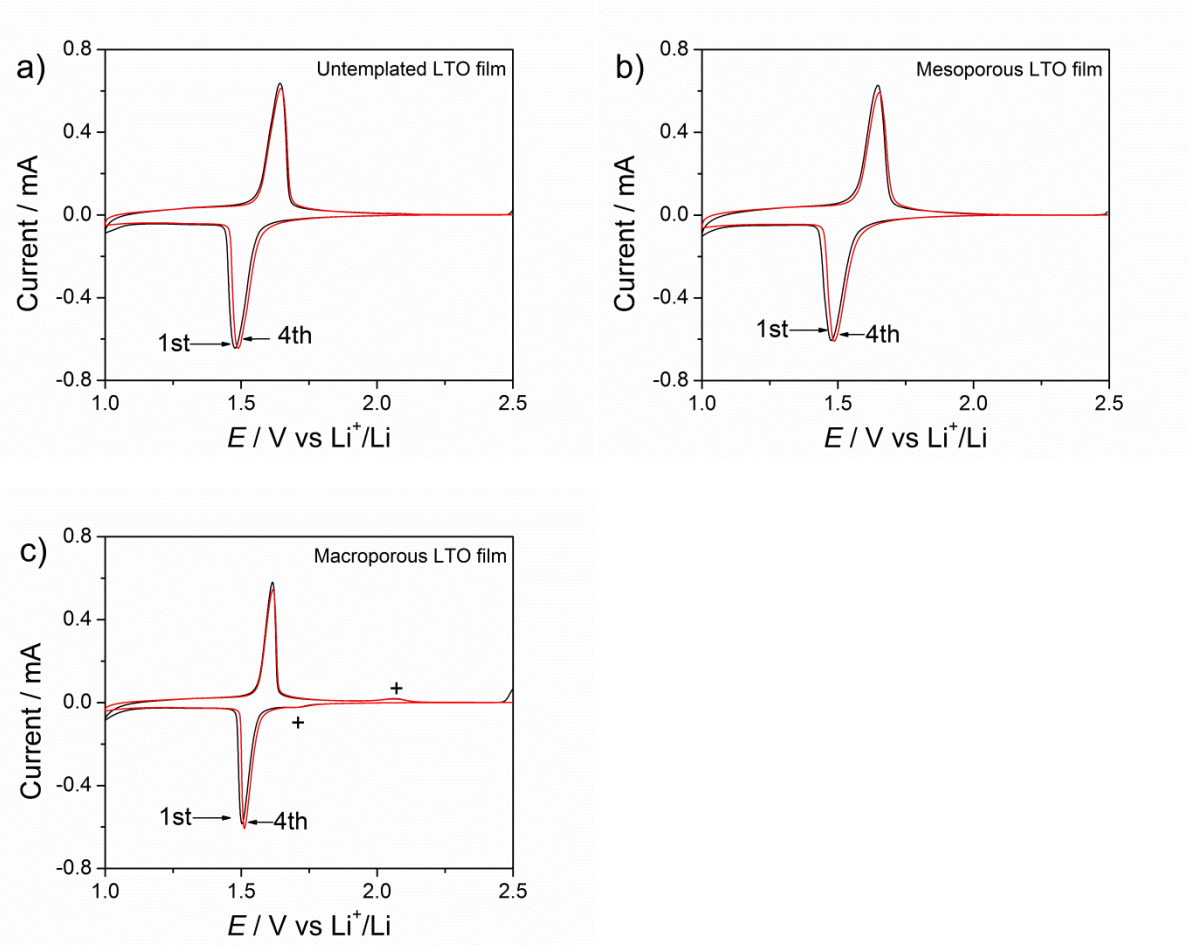

Figure 10 CV of untemplated, mesoporous and macroporous films. The scanning rate is 1 mV/s. The active material mass was estimated by the cathode peak area (the theoretical capacity of LTO is 175 mAh/g) and indicated the active mass of 0.1, 0.1 and 0.065 mg for untemplated, mesoporous and macroporous films. The "+" mark the redox peaks of Li^+ ion intercalation of anatase.

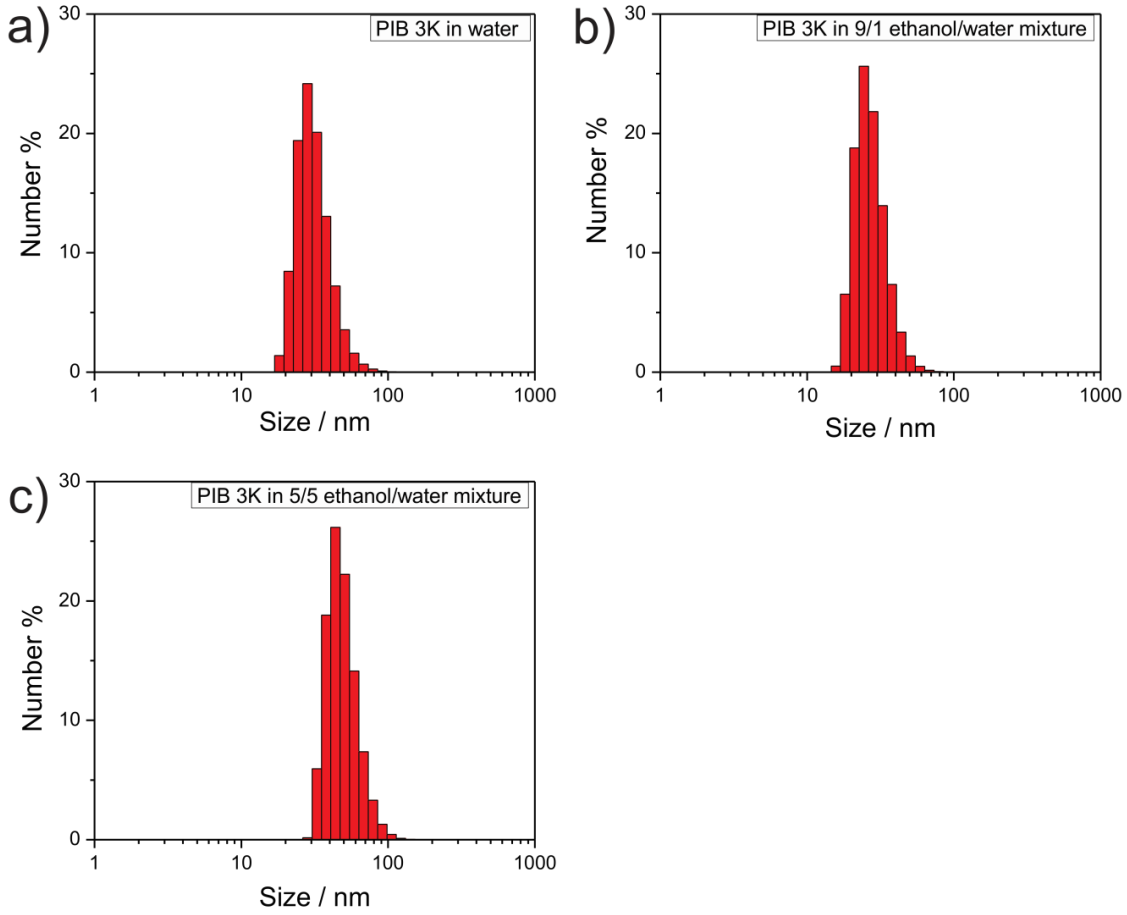

Figure 11 Micelle size distribution of PIB_{50}-*b*-PEO_{45} in different solvents. (a) Pure water. (b) Ethanol/water mixture with volume ratio of 9. (c) Ethanol/water mixture with volume ratio of 1. The results indicated the average micelle sizes of PIB_{50}-*b*-PEO_{45} in (a), (b) and (c) solvents are 30, 25 nm and 50nm, respectively.

LIST OF PUBLICATIONS

1, Opitz, M.; **Yue, J**.; Wallauer, J.; Smarsly, B.; Roling, B., Mechanisms of Charge Storage in Nanoparticulate TiO_2 and $Li_4Ti_5O_{12}$ Anodes: New Insights from Scan rate-dependent Cyclic Voltammetry. *Electrochimica Acta* **2015,** 168, 125-132.

2, **Yue, J**.; Suchomski, C.; Brezesinski, T.; Smarsly, B. M., Polymer-Templated Mesoporous $Li_4Ti_5O_{12}$ as a High-Rate and Long-Life Anode Material for Rechargeable Li-Ion Batteries. *ChemNanoMat* **2015,** 1, 415-421.

3, **Yue, J**.; Suchomski, C.; Smarsly, B. M., Mesoporous Nb-doped TiO_2 Films: The effect of Conductivity on Pseudocapacitive Contributions to Charge Storage. To Journal of Physical Chemistry C

4, **Yue, J**.; Zahn, S.; Zhang, W.; Dietrich C.; Janek, J.; Mollenhauer, D.; Smarsly, B. M., Investigations of crystallite size and doping effects on structure and electrochemical performance of $Li_4Ti_5O_{12}$ nanocrystals. Under preparation

5, **Yue, J**.; Suchomski, C.; Roling B.; Smarsly, B. M., Porous Structures from Pure Crystalline $Li_4Ti_5O_{12}$ Dispersion for ultrafast charge and discharge Lithium Ion Batteries. Under preparation

ACKNOWLEDGEMENTS

After four years spending in Giessen, finally I will complete my doctorate soon. I cannot make it without the support, help and encouragements from my supervisor, friends and family. I would like to express my gratitude to all those who made the creation of this thesis possible.

First of all, I would like to give my sincere thanks to my supervisor, Prof. Dr. Bernd Smarsly for offering me an opportunity to study and work in his group. For me, Bernd is not only a mentor who teaches professional knowledge and gives suggestions on the subject, but also a friend who cares about my career and life.

Secondly, I would appreciate the people whom I have collaborated with in the past: Prof. Dr. Bernhard Roling, who is an expert in electrochemistry and helps me a lot on characterization of electrochemical properties; Dr. Torsten Brezesinski, who helps me finish the electrochemical properties of mesoporous LTO powders; Dr. Stefan Zahn, who helps me calculate the electronic structure of doped LTO nanoparticles.

Frau Gwyneth Schulz and Frau Antonella D'Ambrosio are acknowledged for her nice and patient support on administrative and social work. Dr. Christian Suchomski is specially acknowledged for his help and support whatever in academic side or outside work.

I am very grateful to the past and present members in AG Smarsly and PCI: Dr. Roland Marschall, Dr. Jan Haetge, Dr. Takeshi Hara, Dr. Laemthong Chuenchom, Dr. Daniela Stöckel, Dr. Kristin Faber, Michael Schröder, Claas Wessel, Matthias Böhm, Christoph Weidmann, Rüdiger Ellinghaus, Maren Möller, Zewei Bai, Pascal Vöpel, Christoph Seitz, Martin von der Lehr, Julia Migenda, Rafael Meinusch, Giuliana Beck, Marc O. Loeh, Tobias Weller, Wenbo Zhang, Torben Pfaff, Natalia Kulischow, Chenwei Li and the others whose names are not mentioned here for their scientific support.

Many thanks to the work shop staff for manufacturing battery models for me, Dr. Thomas Leichtweiß for XPS measurement, Rüdiger Ellinghaus for physisorption measurements, Tobias Weller for TEM measurements, Hubert Wörner for TGA-MS, Dr. Erwin Röcker for GC-MS, Pascal Vöpel for the translation of the abstract and declaration.

Special thanks to Chinese friends in Giessen. Without their kind friendship, I cannot live colorfully in Germany.

Last but not the least I would like to thank my parents, my brother, my sister and my nephew for their support and love. It was not an easy decision for me to come here and even harder for me to exchange university in Germany, but their encouragement and understanding made me keep moving on bravely.

For financial support, I would like to thank China Scholarship Council who provides living expenses for three years and I very appreciate that I can be involved in the great project of STORE-E.